Galaxy Formation at Cosmic Noon Probed with Lyman-Alpha Emission

by

Satoshi KIKUTA

Dissertation

Submitted to the Department of Astronomical Science
in Partial Fulfillment of the Requirements for the Degree of

Doctor of Philosophy

The Graduate University for Advanced Studies, SOKENDAI

January 2020

Contents

List of Figures

List of Tables

Acknowledgments

First of all, I would like to express my deepest gratitude to my supervisors, Assistant Professor Masa Imanishi, Assistant Professor Yuichi Matsuda, and Assistant Professor Yutaka Komiyama and former supervisors, Associate Professor Yoshiki Matsuoka and Professor Taddy Kodama, for giving me helpful instructions and having kept me motivated. When I was an undergraduate student at the University of Tokyo, I attended "Subaru Taiken Kikaku," an observation training program for undergraduate students organized by the National Astronomical Observatory of Japan (NAOJ) and I visited the Subaru Telescope atop Maunakea for the first time in my life. Masa and Taddy were organizers of that program and this was how I met them and got interested in physics of galaxies and supermassive black holes. That program was filled with wonderful encounters with great astronomers, including Yusei Koyama, Ichi Tanaka, and Saeko Hayashi, and staffs who kindly supported our observations. I would like to thank Associate Professor Kazuhiro Shimasaku for letting me know about the program and giving me inspiring lectures on galactic astronomy at the University of Tokyo in my undergraduate days which also fostered my interest on galaxies.

Until I visited Maunakea, I was not even aware that such a large number of staffs were involved with one observing program to support us behind the scene. I would like to say big MAHALO to all who supported our observations during this several years with the Subaru Telescope, including the staffs of NAOJ, Maunakea Observatories, and the local Hawaiian people who have been making great efforts to preserve and share the beautiful dark sky of Maunakea with us. It is no exaggeration to say that this work would not have existed at all without them. Actually, my first night at the Subaru Telescope on November 20 of 2013 was totally cloudy. It was a shame at that time, but this energized me to revisit the summit someday by myself as an astronomer, as a principal investigator of scientific proposals [1]. As Taddy said after the night, “that’s life and that’s astronomy” — this may be one of the greatest lessons I have learned in the program. I am very happy that most of students who share the bitter feeling with me at the night — Yuma Sugahara, Tadafumi Matsuno, Tomohiro Inada, Akiko Tei, and Yuko Matsushita — finally decided to pursue careers as astronomers. They are always not only good friends but also good rivals who have motivated me for years. Best wishes for clear skies for their future observations!

I owe a great debt to Assistant Professor Yuichi Matsuda. High-quality imaging data taken with Hyper Suprime-Cam on the Subaru Telescope, which is the most important ingredient of this thesis, was kindly provided by him. I learned a lot of things from him – not only about science but also about creativity. He is always friendly to others and never hesitates to collaborate with people from different backgrounds such as physicists, mathematicians, and even biologists. Such an open attitude must be a key to be always creative. He also brought about precious opportunities to meet world’s greatest astronomers. Thanks to his introduction, I was so fortunate to visit laboratories of Professor Chuck Steidel at California Institute of Technology (Caltech), Professor Scott Chapman at NRC Herzberg, and Professor Renyue Cen at Princeton University for a few months as a research internship. They all are very productive and fully enjoying science without damaging their daily family lives, for which I truly respect. Needless to say, this thesis was significantly improved through insightful discussion with those people. I also deeply thank five thesis committee members, Associate Professor Tadafumi Takata, Assistant Professor Yusei Koyama, Assistant Professor Kazuhiro Hada, Associate Professor Kazuhiro Shimasaku, and Associate Professor Hidenobu Yajima for their careful reading and many constructive comments which also greatly improved the quality of the thesis.

Research internship at Caltech, Princeton, and NRC Herzberg was one of the greatest experience I have ever had. I was so impressed by blessed research environments of the most reputable universities in the US and motivated graduate students there. Internship was mostly fun and exciting, but sometimes I feel low due to many kinds of hardship. Especially, as a non-native, non-fluent English speaker, being a “foreigner”

---

[1] Actually, the revisit is yet to be achieved, despite I was awarded Subaru observing time for three times — those programs are (will be) either conducted in the HSC queue mode, or as a service program, or with the Keck Telescope!

alone was interesting but also a bit tough experience. During my visit at Caltech, Hien T. Nguyen at NASA/JPL helped me a lot in many ways — he was so kind that he even allowed me to stay at his house for a week. He told me a lot of interesting stories (e.g., about his stay at Antarctica). Among them, what I remember the most was what he said about his dream (which is to be a scientist and already came true). It was something like the following: “it is far more important to be crazy about something than to be just good at something”.

Music is always (when I am depressed, healthy, being abroad alone, reading or writing papers, etc.) my source of energy. Above all, I cannot thank enough to a Japanese rock band “the pillows.” The day before the deadline for a doctoral thesis for preliminary defense, I saw their 30th-anniversary live show at Yokohama Arena, putting aside the unfinished draft of my thesis. I always think astronomers (or maybe researchers in general) are so much alike musicians — both are forced to be constantly in fierce competition to survive, but both truly love what they do. The songs and lyrics written by Sawao Yamanaka of the pillows are, in that sense, so powerful and impressive that it seemed as if he would have been singing just for me. Sometimes metaphorically and sometimes directly, they sing a lot about chasing dreams and fighting against all odds, powerfully encouraging all the audience. Actually, I was at that time still anxious and unsure about my career after completion of a Ph.D. course. However, leaving Yokohama Arena after the show, I was then reassured and no longer worried about the future, since I realized (or just remembered) during their show that I am indeed crazy enough about astronomy. I must say that I am so grateful to my friend since undergrad, Tomoki Emmei, who got tickets of the show and invited me to come. He was actually the person who cheered me up in Pasadena. When I was staying at Caltech, he was also there totally by chance for internship at NASA/JPL. My life might have been different without his action. As the pillows sang on that night, the gravity of rock’n’roll was actually almighty.

I would like to thank wonderful roommates and colleagues around Subaru building at NAOJ: Tadafumi Matsuno, Mayuko Mori, Takuma Izumi, Mariko Kubo, Hiroyuki Ishikawa, Jun Hashimoto, Taiki Kawamuro, Shunsuke Baba, Takuji Yamashita, Kei Ito, and Shigeru Namiki. Casual chat and discussion with these people are not only fun and inspiring but also have played an evidently important role for keeping me sane during five year long daily life at NAOJ. Lunch at the NAOJ cafeteria with those people worked very well to keep my body clock regular — without it I easily disturb life rhythm and end up waking up afternoon. I hope that our friendship will last gigayear-long.

And finally, none was more supportive as my parents, Ichiro and Keiko Kikuta. Words cannot express my gratitude to both of them. I like the most the freedom they offered me and let me just say thank you for taking care of me for such a long time and accepting and respecting my decision to be an astronomer.

Data analysis was carried out on the Multi-wavelength Data Analysis System operated by the Astronomy Data Center (ADC), National Astronomical Observatory of Japan, for which I am thankful. I would like to thank Yukie Oishi and the HSC pipeline team for their many helpful comments on HSC data analyses. I acknowledges supports from the JSPS KAKENHI grant No. 18J11477 and the Course-by-Course Education Program of SOKENDAI.

Abstract

In the current framework of galaxy formation, cold gas accretion from the cosmic web which forms the backbone of the Universe with dark matter, fuels star formation and active galactic nucleus (AGN) activity in galaxies. After star formation proceeds, accreted gas from the intergalactic medium (IGM) interacts with gas ejected from galaxies via various feedback mechanisms in the circumgalactic medium (CGM, roughly referring to gas within a few times the virial radii of galaxies), regulating the galactic gas supply. Thus, the IGM and CGM are crucial components to reveal galaxy formation and evolution, and extensively studied for decades. Despite many efforts, however, there remains so much mystery about them, e.g., if the cosmic web filaments really exist at high redshift in the first place, how much the gas distribution is affected by their large-scale environments, and so forth.

In this thesis, we tackle these issues mainly using the Lyα emission line. Our goal is to detect the IGM in Lyα emission, which will lead to further investigation with spectrographs to constrain detailed physical properties of the IGM. At the same time, we aim to characterize the CGM around LAEs at $z \sim 3$, through stacking analyses. We especially focus on "protoclusters", which are ancestors of today's galaxy clusters, since they are the site of the most active, massive galaxy formation within which various important processes are at work. We present our results of successful wide-field observations with the Hyper Suprime-Cam (HSC) on the Subaru Telescope targeted at a massive protocluster at $z = 2.85$, at the center of which a "hyperluminous" QSO (HLQSO) resides. Using a narrow-band filter, we can detect redshifted Lyα emission from that redshift, and probe the IGM and CGM around the protocluster and other normal density fields at the same time, thanks to the wide field of view of the HSC.

In Chapter 2, we focus on the large- and small-scale Lyα structure around the QSO.

As we took wide-field images centered at the protocluster and the QSO, we can probe diverse environments from a protocluster to void regions simultaneously. Lyα emitters (LAEs, young star-forming galaxies) are used to trace the large-scale structure at $z = 2.85$ and the distribution of Lyα blobs (LABs, galaxies with extended Lyα emission) is studied. We revealed the large-scale filamentary structure extending from the protocluster. LABs are basically distributed along the structure, with larger ones particularly clustering around the HLQSO, confirming a previously noted tendency of LABs to prefer denser environments. We then describe diffuse Lyα emission detected around the QSO revealed with our deep imaging observations. One diffuse nebula has no luminous UV/sub-mm counterpart within it and has a filamentary shape pointing toward the HLQSO. We propose a few explanations for this nebula; one interesting possibility is that the nebula may represent a cold filament which is predicted in simulations but remains observationally elusive until very recently.

With the same datasets, we can probe the CGM of LAEs through stacking analysis. Chapter 3 will focus on diffuse Lyα emission around LAEs, or Lyα halos (LAHs). The depth and wide field coverage of our data enable us to argue the dependence of LAHs on various galaxy properties, especially on Mpc-scale environments with unprecedented depth and sample size at $z \sim 3$. With 3490 LAEs within the field, we probe LAHs of various subsamples through stacking of their Lyα images. Subsamples are constructed with 5 quantity: UV magnitude, Lyα luminosity, Lyα equivalent width, local environment, and distance from the HLQSO. We succeeded to detect more extended Lyα emission compared to UV continuum emission in all subsample. UV-bright/Lyα-bright/low-Lyα equivalent width LAEs have more extended LAHs, while the distance from the QSO seems not to make a large difference in LAHs. Finally, combining our results and those in literature, we conclude that the dependence of LAH shapes of LAEs on large-scale environments is only evident in the densest parts of the Universe, i.e., in protoclusters. These results suggest that the CGM distribution around star-forming galaxies at $z \sim 3$ in normal environments is mainly determined by their own properties such as halo masses instead of their external conditions.

Our goal of detecting the IGM in Lyα emission is partially achieved in this thesis — we discovered a promising candidate and further characterization is still ongoing. At last in Chapter 4, we highlight key results and present our future directions to further approach the ultimate goal of understanding the galaxy formation at high redshift.

1

Introduction

Galaxy is a fundamental component of our Universe. Revealing how did they form and evolve is one of the major goals of today's astronomy. This thesis intends to take a small step toward this goal with an observational exploration of galaxies in the distant past, especially using the Lyα emission line. In this Chapter, current understanding and unresolved questions about galaxy formation and evolution are briefly discussed.

1.1 Galaxy Formation at Cosmic Dawn

Before reviewing galaxy formation, we need to know our Universe, in which everything happens. Observations revealed that the Universe is almost flat and its energy density is 95% dominated by dark energy in the form of the cosmological constant Λ and "cold" dark matter, which is collisionless, dissipationless, and having negligible random motion (Planck Collaboration et al., 2015). Soon after the Big Bang, almost uniformly distributed matter — both dark and visible (baryons), starts to form self-bound dense clumps under gravity, known as halos (see the initial seminal work by Press & Schechter, 1974). Subsequent behavior of dark matter is relatively easily followed by numerical calculations within a framework of the so-called ΛCDM paradigm. Statistical properties of the large-scale matter distribution derived from observations and simulations agree very well (e.g., Springel et al., 2005b), although some problems remain on small scales (e.g., the so-called missing satellite problem; Moore et al., 1999).

Figure 1.1 shows dark matter and gas (baryons) distributions at various redshifts in a numerical simulation (Vogelsberger et al., 2014). Following gravity, dark matter makes up a bubble-like structure out of initial density fluctuations as imprinted in the cosmic microwave background. Basically, ordinary matter is also distributed along this network structure, often referred to as "**the cosmic web**". Galaxies are formed at the center of halos of dark matter and evolve by acquiring pristine gas from the cosmic web and by merging with other galaxies. However, subsequent evolution of galaxies is not as simple to predict as that of dark matter halos, because of the complexity of baryon-related processes. In the following sections, details of those processes are reviewed.

1.2 Cold Mode Accretion as a Main Driver of Galaxy Evolution

In the classical scenario of galaxy formation, galaxies acquire gas by spherical infall of gas heated to the halo virial temperature (e.g., Rees & Ostriker, 1977; White & Rees, 1978). However, as seen in Figure 1.1, gas accretion should occur in a filamentary network rather than in a spherical halo (Katz & White, 1993). In the early 2000s, an alternative picture, which is now widely accepted as "**the cold mode accretion**" paradigm, emerged (Fardal et al., 2001; Birnboim & Dekel, 2003; Kereš et al., 2005; Dekel & Birnboim, 2006); in this scenario, a substantial fraction of accreted gas is predicted to remain dense and cold (below halo virial temperature) during accretion, in the form of thin filaments, never shock-heated by virial shock.

Whether cold mode accretion occurs or not is determined by the stability of shock. It is evaluated by comparing the cooling time t_{cool} and compression time t_{comp} of post-shock gas. If $t_{\mathrm{cool}} < t_{\mathrm{comp}}$ (due to e.g. high gas density/metallicity), it radiatively cools and rapidly reduce pressure, failing to support the shock. Through analytic arguments and one-dimensional numerical simulations, Birnboim & Dekel (2003) showed that in halos with masses lower than the shock halo mass $M_{\rm shock}$ ~a few $\times 10^{11}\ M_\odot$ this condition is always met almost independent of redshift. Since at $z > 2$ the typical halo mass of each epoch (the Press-Schechter mass) is below this value, most galaxies are fed by cold mode accretion. On the other hand, halos with $M_{\rm h} > M_{\rm shock}$ at $z \gtrsim 2$ tend to be found in the nodes of the cosmic web. Since the mass accretion rate is roughly proportional to the halo mass while the filament width does not have a strong dependence on the halo mass, gas density of filaments penetrating the high mass halos becomes much higher than simple calculations (Dekel & Birnboim, 2006; Dekel et al., 2009, see Figure 1.2). As a result, filaments can penetrate through such high-redshift massive halos even after the development of the hot media. More realistic simulations reproduce similar results qualitatively, with no strong dependence on the numerical methods (Ocvirk et al., 2008; Kereš et al., 2009; Agertz et al., 2009; van de Voort et al., 2011; Nelson et al., 2013). The hot-mode accretion, once thought of as the dominant mode, becomes gradually important in massive halos but only at $z \lesssim 2$. Thus, the cold mode accretion can be said to be the main driver of galaxy evolution, especially at high redshift Universe.

This cold/hot mode accretion paradigm could be a key to reproduce one of major observed features of galaxies, **the galaxy bimodality** in color, shape, and star formation rate (Kauffmann et al., 2003; Baldry et al., 2004, see Figure 1.3), since the observed transition mass from blue/spiral/star-forming galaxies (collectively referred to as "blue cloud galaxies") to red/spheroidal/quiescent galaxies (collectively referred to as "red sequence galaxies") at $z = 0$ is similar to $M_{\rm shock}$. However, there are also some drawbacks. First, early studies which probe the importance of cold streams treated feedback only crudely (if any). For example, metal enrichment can drastically alter the cooling function and the interaction with galactic winds would generate turbulence (Fielding et al., 2017; Stern et al., 2019). Secondly, **observational evidence for the cold mode accretion is still very limited in the literature**. We will return to this problem in Section 1.5.

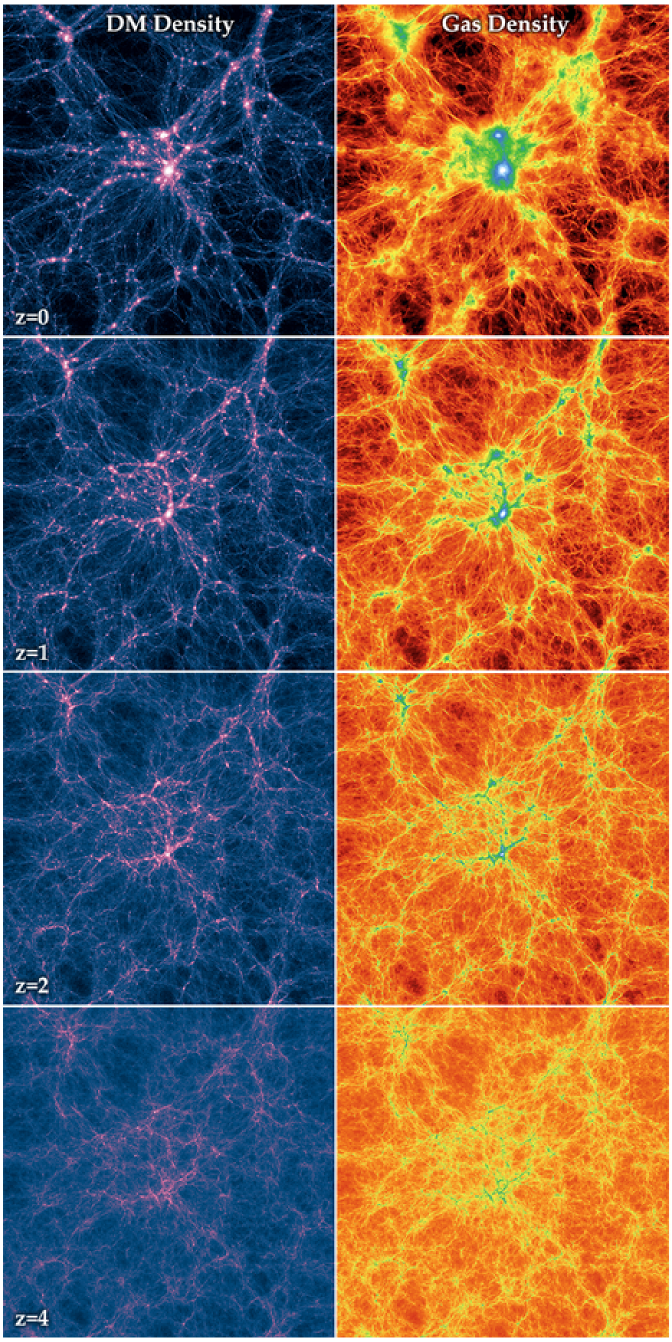

Figure 1.1: Redshift evolution of the dark matter (left) and gas (right) distribution for $z = 0,\ 1,\ 2,$ and 4 in a projected slice with a thickness of 21.3 comoving Mpc and a width of 106.5 Mpc in the Illustris simulation (Vogelsberger et al., 2014). At the center is the most massive cluster at $z = 0$ in the simulation.

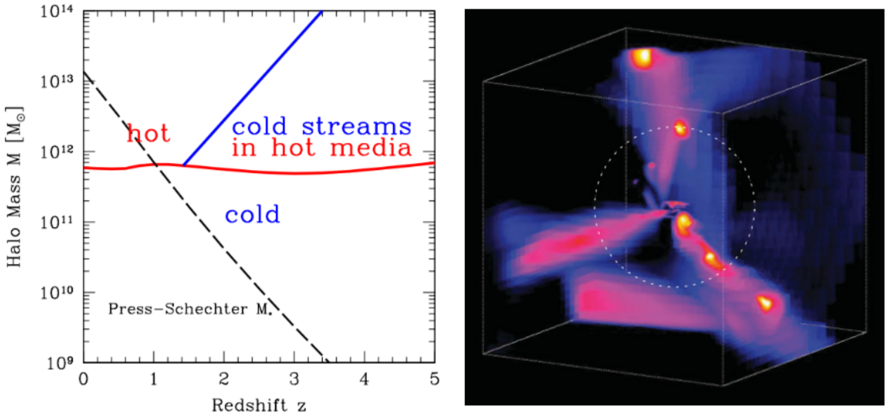

Figure 1.2: (Left) Diagram to predict a dominant mode of accretion from Dekel et al. (2009). The nearly horizontal red curve shows M_{shock}, above which a shock-heated medium is present. At $z \gtrsim 2$, even $M_{\mathrm{h}} > M_{\mathrm{shock}}$ halos have cold streams due to enhanced stream density. Dashed curve indicates the Press-Schechter mass which corresponds to typical dark matter halo mass for a given epoch. (Right) Streams in the simulation of (Dekel et al., 2009). The dotted circle indicates the halo virial radius. Three main streams are visible, two of which containing low-mass clumps.

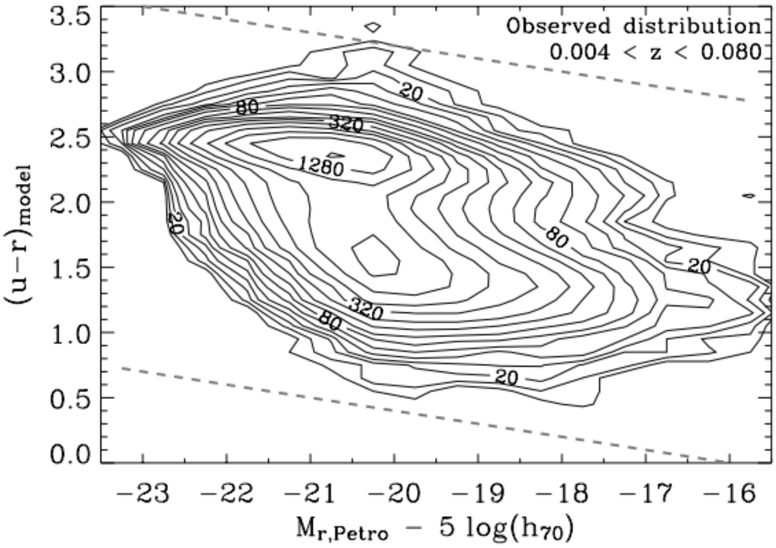

Figure 1.3: Observed distribution of nearby ($0.004 < z < 0.080$) SDSS galaxies in rest-frame u − r color VS. absolute SDSS r-band magnitude. There are two prominent peaks at the redder/brighte side and the bluer/fainter side. This trend is referred to as the galaxy bimodality.

1.3 Feedback from Stars and Active Galactic Nuclei

Galaxy evolution as a whole can be traced by the galaxy stellar mass function. Here, the mass function (of all kinds) is defined as the number density of something per logarithmic mass interval as a function of mass. Naively, more massive dark matter halos should contain more baryons and therefore more stars in proportion to their dark matter mass. In reality, the distribution of baryons does not completely follow that of dark matter. Figure 1.4 and 1.5 respectively show the dark matter halo mass function in a numerical simulation (Ishiyama et al., 2015) and observed galaxy stellar mass function (Baldry et al., 2008) at $z = 0$. In Figure 1.5, the dark matter halo mass function multiplied by $\Omega_\mathrm{b}/\Omega_\mathrm{m}$ (baryon fraction) is overplotted. Apparently, their shapes are similar; massive halos are rare and less massive halos are abundant. However, we have much fewer massive and low-mass galaxies than naively expected. This means that there are some mechanisms that alter the efficiency of star formation depending on halo masses. Revealing what physical mechanisms are regulating this efficiency is of particular importance to understanding galaxy evolution.

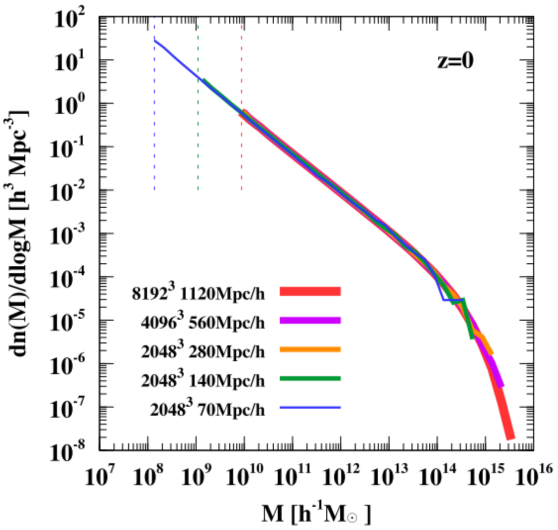

Figure 1.4: The dark matter halo mass function at $z = 0$ derived in a recent cosmological N-body simulation (Ishiyama et al., 2015). Different colors show different resolution/box size of the simulation. Vertical dashed lines denote the minimum halo mass of each simulation.

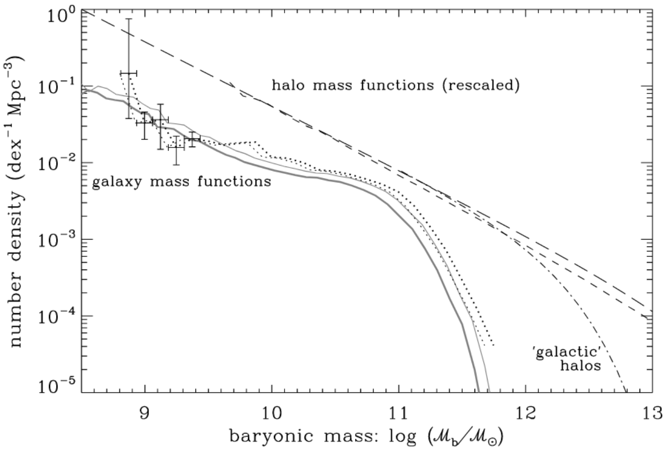

Figure 1.5: The galaxy stellar mass function at $z = 0$ (Solid and dotted curves; Baldry et al., 2008). Dashed and dot-dashed curves are the dark matter halo mass functions multiplied by Ω_b/Ω_m. Dot-dashed curve are the dark matter halo mass function derived by excluding the contribution from groups and clusters of galaxies.

The energy released by massive young stars and subsequent (type-II) supernova (SN) explosions is huge (emits $\sim 10^{57}$ erg per one SN). Gas in galaxies is heated and/or ejected from the galaxies by the energy injected by young stars, thereby stopping further star formation. This is why the process is called "feedback". The classical example of "superwinds" caused by stellar and SN feedback can be seen in M82.

In the most massive galaxies, stellar feedback alone cannot stop excessive star formation and other mechanisms to stop over-cooling are required. The leading candidates for sources for additional negative feedback are supermassive black holes (SMBHs) at the center of galaxies. The ubiquity of SMBHs in massive galaxies and the correlation between the masses of SMBHs and spheroidal components of galaxies (Magorrian et al., 1998) strongly suggest that SMBHs have played a crucial role in galaxy evolution. Indeed, actively growing SMBHs can emit an enormous amount of energy and are observed as active galactic nuclei (AGNs). **Quasars** (or quasi-stellar objects, or **QSOs**) are a subclass of AGNs that are very bright in the optical waveband[1]. In some AGN-hosting galaxies, massive outflows are observed (Feruglio et al., 2010; Cano-Díaz et al., 2012; Cicone et al., 2015). In addition, radio-loud (and not necessarily bright in UV/optical) AGNs can reduce star formation rate in host galaxies differently. Their

---

[1] However, there is no strict definition for these nomenclature.

powerful radio jets heats the surrounding media and prevent it from further cooling (McNamara et al., 2009). Theoretical models which include AGNs and associated feedbacks are known to reproduce many observables fairly well (e.g., Kauffmann & Haehnelt, 2000; Hopkins et al., 2006), although related sub-grid physics is still very uncertain and need to be constrained.

1.4 Environmental effects on Galaxy Evolution

At $z = 0$, fundamental properties of galaxies such as their colors, morphologies, star formation rate, and so forth are known to strongly depend on **environments** they reside. Galaxies in clusters tend to have redder color and elliptical morphology, while field galaxies more likely to have bluer color and spiral shapes (Dressler, 1980; Cappellari et al., 2011, see Figure 1.6). Thus galaxy environments must be another key to understand the origin of the galaxy bimodality and how to quench galaxy growth along with the accretion mode (Section 1.2).

By tracing back to the epoch of cluster formation in the early Universe, clues to reveal the origin of this "environmental effect" have been collected. Butcher & Oemler (1984) showed that high-redshift galaxy clusters tend to have a higher "blue galaxy fraction", defined by the ratio of the number of blue galaxies to that of all member galaxies. Since then, numerous research groups have conducted intensive searches for "protoclusters" (see Overzier 2016 for a review), which is loosely defined as ancestors of present-day's galaxy clusters. Observations of protocluster revealed that at redshift two to three, or "**cosmic noon**", a reversal of the SFR-density relation and accelerated galaxy formation at protoclusters occurred (e.g., Koyama et al., 2013). The red sequence also began to develop afterward (Kodama et al., 2007). Moreover, it is not only the peak epoch of the cosmic star formation rate density (Hopkins & Beacom, 2006), but also the maximum of the cold mode accretion rate onto massive halos through the cosmic web (Kereš et al., 2009). This is the very epoch of active cluster formation and thus important epoch to constrain to reveal the role of environments in galaxy formation.

In addition to an enhanced inflow rate of cold gas, frequent mergers/interactions with other galaxies due to a high galaxy number density in protoclusters may accelerate galaxy evolution within them. Mergers have long been thought to trigger starburst and AGN activity since it allows gas of colliding galaxies to lose its angular momentum and

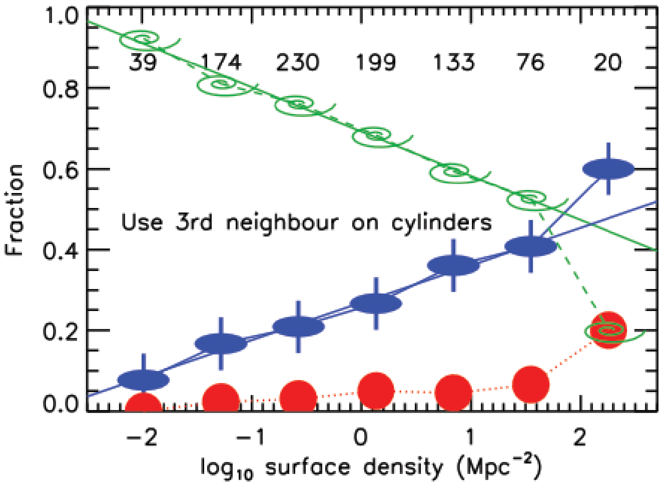

Figure 1.6: The morphology-density relation of galaxies at $z = 0$ (Cappellari et al., 2011). Vertical axis shows the fraction of galaxies with some morphological types (spiral galaxies: green spiral; fast rotators: blue ellipse with vertical line; slow rotators: red filled circle. Fast/slow rotators are early-type galaxies with and without a prominent rotation signal. Roughly speaking, the former corresponds to the classical lenticular galaxy and the latter corresponds to more massive elliptical galaxies) as a function of local environments (horizontal axis). The rightmost part of this figure corresponds to the density at the center of clusters of galaxies. This figure clearly shows that the fraction of spiral galaxies decreases with increasing galaxy surface density, suggesting some environmental effects at work.

channels a large amount of gas into the central part of galaxies, transforming the resultant galaxy's morphology into spheroidal (Toomre & Toomre, 1972; Hernquist & Mihos, 1995; Springel et al., 2005a; Teyssier et al., 2010). Observations of ultraluminous infrared galaxies (ULIRGs, galaxies with $L_{\rm IR} > 10^{12}L_{\odot}$) and submillimeter galaxies (SMGs) revealed a high fraction of mergers/interactions and AGN activity within them (Alexander et al., 2005; Takata et al., 2006), supporting an evolutionary link between mergers and starbursts/AGNs (Sanders et al., 1988; Scoville et al., 2000). Such active populations are often said to be ancestors of the most massive elliptical galaxies at $z = 0$ considering that their star formation history suggests that a bulk of their stellar population should be formed at $z > 2$–3.

Before closing this Section, we explain here how protoclusters are found. They do not have some features that galaxy clusters at $z = 0$ have such as extended X-ray emission and the Sunyaev-Zel'dovich effect, both originated from high-energy particles in very massive halos, and the well-defined red sequence in the color-magnitude diagram. We cannot rely on such features and have to invent other techniques. A blind survey is the most simple and unbiased way. To do this, the Lyman break technique is most often used to locate high-redshift (mostly star-forming) galaxies. Ionizing continuum emission from distant galaxies has to travel great distance toward us. In the course of the journey, UV light suffers from the absorption by neutral hydrogen (Lyman series absorption) in the intergalactic medium. The Lyman-break technique utilizes this nature to select high-redshift galaxies. In particular, the breaks made by Lyman-limit (921Å) and Lyα (1216Å) absorption can be identified by a difference in magnitudes in some broad-band filters (see Figure 1.7a and Figure 1.7c). Since these features made high-redshift galaxies distinct from other objects in an appropriate color-color plot, these galaxies — the **Lyman-break galaxies** (**LBGs**) — can be selected via multi-band imaging observations with redshift uncertainty $\Delta z \sim 1$ and turned out to be very successful to probe high-redshift Universe (e.g., Steidel et al., 1996; Ouchi et al., 2004; Shimasaku et al., 2005; Bouwens et al., 2015; Ono et al., 2017).

Another efficient technique is used to select galaxies called "**Lyα emitters**" (**LAEs**). They are identified by their intense Lyα emission. When the Lyα line of a galaxy redshifts into the range where **narrow-band filters** are sensitive, it shows the excess of narrow-band magnitude with respect to broad-band magnitude which contains both the continuum emission and the Lyα emission (see Figure 1.7b and Figure 1.7d). This technique has also been used to detect a significant number of high-redshift star-forming galaxies at $z > 2$ with redshift uncertainty $\Delta z \lesssim 0.1$ (Cowie & Hu, 1998; Rhoads et al., 2000; Ouchi et al., 2003, 2008, 2010, 2017; Kashikawa et al., 2006). Most protoclusters are found with either of these techniques (Steidel et al., 1998, 2005; Shimasaku et al., 2003; Ouchi et al., 2005; Toshikawa et al., 2012, 2018; Higuchi et al., 2018).

Besides blind search with Lyman break and narrow-band techniques, many authors attempted to use extreme objects as signposts of overdense regions of the high-redshift Universe. AGNs are thought to be triggered by major merger and thus we naively expect that they should reside more frequently in overdensity where a merger rate should be higher than that in normal fields. While radio-loud AGNs are often found in overdense environments (Zheng et al., 2006; Venemans et al., 2007; Matsuda et al.,

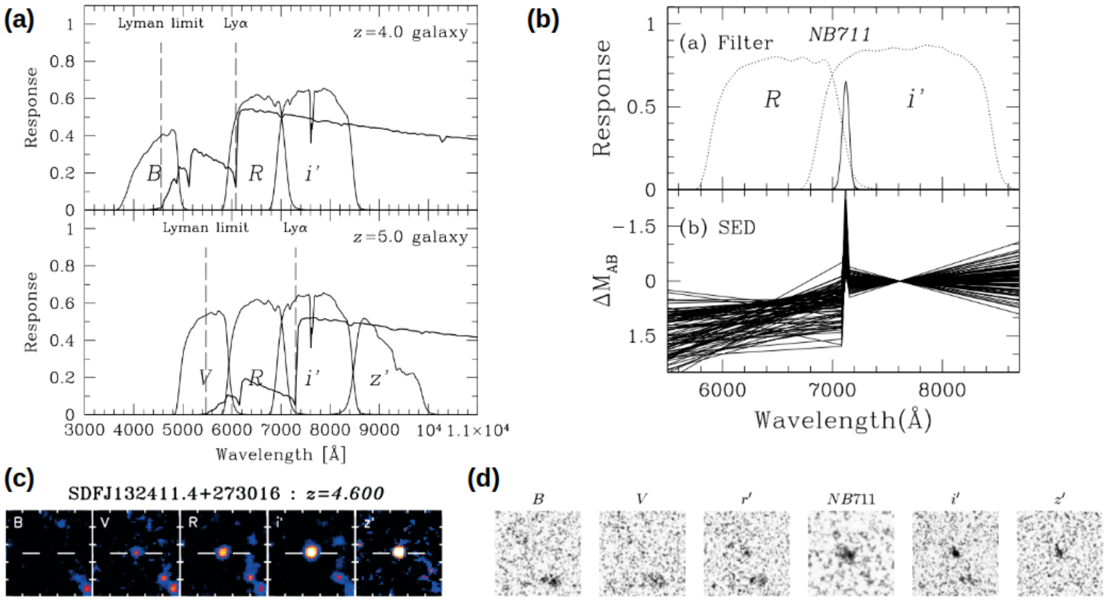

Figure 1.7: (a): Transmission curves of *B*-, *V*-, *R*-, *i'*-, and *z'*-band filters installed on the Suprime-Cam on the Subaru telescope and modeled generic spectra of star-forming galaxies at redshift 4 (Top) and 5 (Bottom) (Yoshida et al., 2006). Position of breaks made by Lyman limit and Lyα is also marked by vertical dashed line. (b): Transmission curves of *R*-, *NB711*-, and *i'*-band filters of Suprime-Cam (Top) and observed SED of galaxies selected by a narrow-band technique (Ouchi et al., 2003). Lyα emitters are only detected when their redshifts are precisely matched with the transmission of narrow-band filters. (c): Example snapshot of a galaxy selected by the Lyman-break technique (= Lyman-break galaxy) (Ouchi et al., 2004). Dropout in *B*-band is clearly seen. (d): Example snapshot of a galaxy selected by a narrow-band technique (= Lyα emitter) (Shioya et al., 2009). Dropout in *B*-, *V*-, and *R*-band and detection in *NB711*-band is seen.

2009; Wylezalek et al., 2013), whether this is also the case for radio-quiet ones is still a controversial topic (YES: Capak et al. 2011; Falder et al. 2011; Swinbank et al. 2012; Husband et al. 2013; Morselli et al. 2014, NO: Kashikawa et al. 2007; Kim et al. 2009; Bañados et al. 2013; Simpson et al. 2014; Adams et al. 2015; Mazzucchelli et al. 2017; Kikuta et al. 2017; Uchiyama et al. 2018).

1.5 Intergalactic Medium (IGM) and Circumgalactic Medium (CGM)

As discussed in Section 1.2 and 1.3, galaxies are not closed systems at all. They acquire gas from the cosmic web, lose some by various feedback processes, and some is pulled back again by gravity (recycled) to form stars and feed SMBHs. The diffuse gas floating between galaxies and making up the cosmic web are called **the intergalactic medium (IGM)**, whereas gas associated with galaxies is called **the circumgalactic medium (CGM)**. Although there is no clear boundary between the IGM and CGM, the latter roughly refers to gas within a few times the halo virial radii of galaxies. Figure 1.8 illustrates the CGM around a galaxy a recent review paper by Tumlinson et al. (2017).

The IGM and CGM of high-redshift galaxies are frontier of galactic astronomy, both for observers and theorists. Accretion of the IGM is the central prediction of the cold accretion paradigm. Determining how and how much gas is actually accreted onto galaxies and comparing it with simulations are thus urgent tasks. Nevertheless, **direct evidence of the IGM in the cosmic web has not been found until very recently** (Umehata et al., 2019). Conventionally, observational constraints on the IGM have mainly been extracted from absorption lines on background quasars (e.g., Sargent et al., 1980; Miralda-Escude et al., 1996). However, its one-dimensional nature, the small surveyed volume, and the sparseness of the background quasars (especially at $z > 3$) prevent us from further constraining important properties of the IGM in terms of galaxy evolution, such as two- or three-dimensional distribution and morphology around individual galaxies. Direct detections of the IGM in emission is desirable for further investigations, although the IGM are predicted to be undetectably faint ($\sim 10^{-20}$ erg s^{-1} cm^{-2} arcsec^{-2} Gould & Weinberg, 1996; Cantalupo et al., 2005; Kollmeier et al., 2010; Witstok et al., 2019) — if just consider illumination by cosmic

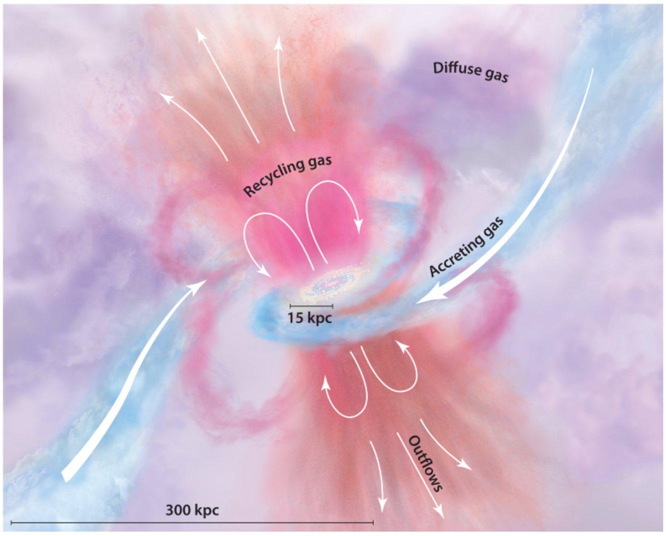

Figure 1.8: Schematic picture of the CGM around a galaxy (Tumlinson et al., 2017). Blue accreting gas from the IGM is connected with the cosmic web on larger scales. Such gas fuels star formation in the disk and feeds a central SMBH, which in turn create outflow illustrated by red fountains above and below the disk. Some of the blown-out gas is re-accreted and recycled. Here redder color is used to show more enriched gas and bluer color means it is nearly pristine.

ultraviolet background radiation.

The CGM has rich information about galaxy evolution since it is the very place where accreted cold gas and blown-out gas by feedback are mixed and interact. Although observations of the CGM is easier than those of the IGM, most studies are based on absorption lines of neighboring background quasars/galaxies (Adelberger et al., 2005; Steidel et al., 2010; Tumlinson et al., 2011; Rudie et al., 2012; Rakic et al., 2012; Turner et al., 2017; Prochaska et al., 2017). UV spectra of high-redshift galaxies themselves are also informative, since stellar light of host galaxies comes through the CGM and thus acts as a background light source. Inflow/outflow signals and the mass loading factor (the ratio of the outflow rate to the star formation rate) are extensively studied with this method (Heckman et al., 2015; Trainor et al., 2015; Sugahara et al., 2017). One should note that there are a number of uncertain assumptions such as the geometry of outflows when deriving the outflow rate. These should be constrained by more direct observation with emission lines.

Reproducing observed properties of the CGM in numerical simulations is much more difficult, partly because of its multiphase nature. The results vary significantly depending on how feedback is implemented and also spatial resolution of the simulations. Recent studies clearly showed the importance of a high spatial resolution of the order < 1 kpc (Peeples et al., 2018; Corlies et al., 2018; Hummels et al., 2018; van de Voort et al., 2019; Suresh et al., 2019). Small scale features reproduced in enhanced resolution simulations can dramatically change emission properties, since the emissivity is proportional to density squared if collisional processes (recombination, collisional excitation) dominates. The emissivity due to collisional excitation depends also on gas temperature exponentially around $T \sim 10^4$ K, making accurate predictions even more difficult (Faucher-Giguère et al., 2010).

Techniques to study the IGM and CGM with emission lines have been gradually developed. The Lyα line is the brightest emission line among all and thus has been a natural choice for observers. In early 2000s, objects known as "**Lyα blobs**" (**LABs**; Keel et al., 1999; Steidel et al., 2000; Francis et al., 2001, see Left panel of Figure 1.9) at $z > 2$ are precious targets in this light. They are bright ($L_{\mathrm{Ly}\alpha} > 10^{43}$ erg s^{-1}) and extended Lyα nebulae without obvious power sources such as AGNs. More than ten years later, giant Lyα nebulae around radio-quiet QSOs [2] started to be found (Cantalupo et al., 2014; Martin et al., 2014; Hennawi et al., 2015, see Middle panel of Figure 1.9). Their extents sometimes exceed 200 physical kpc (almost the halo virial diameter of halos with $M_{\mathrm{h}} \gtrsim 10^{12} M_\odot$ at $z \sim 3$) and therefore a number of authors supposed that they represent the densest part of the cosmic web. Proving this is however difficult, since strong shocks induced by outflow launched by hidden starburst and/or AGN activity may also explain observed Lyα luminosity and extent of LABs (Taniguchi & Shioya, 2000; Mori & Umemura, 2006) as the case for radio-loud AGNs. Other powering mechanisms include: gravitational cooling during accretion (Dijkstra & Loeb, 2009; Goerdt et al., 2010; Faucher-Giguère et al., 2010; Rosdahl & Blaizot, 2012; Yajima et al., 2013), scattered Lyα photon from star formation or AGNs (Dijkstra & Kramer, 2012; Cen & Zheng, 2013; Cantalupo et al., 2014), or recombination due to ionizing radiation from nearby source (most likely, QSOs; Haiman & Rees 2001; Kollmeier et al. 2010; Gronke & Bird 2017). One of the most interesting observational traits of LABs is they

---

[2] Lyα nebulae around radio-loud AGNs and radio galaxies are discovered earlier than those around radio-quiet AGNs. They have a spatial correlation with radio jets and violent kinematics, suggesting that they are originated from shocked outflowing gas (Heckman et al., 1991; van Ojik et al., 1996).

tend to reside in dense environments, i.e., fields around protoclusters (Matsuda et al., 2004; Prescott et al., 2008; Bădescu et al., 2017; Zhang et al., 2019).

Thanks to the accumulated large dataset and the advent of sensitive integral field units (IFUs) such as the Multi-Unit Spectroscopic Explorer (MUSE; Bacon et al., 2014) on the Very Large Telescope, the Keck Cosmic Web Imager (KCWI; Morrissey et al., 2018) on the Keck Telescope, and the newly implemented IFU mode of the Faint Object Camera and Spectrograph on the Subaru Telescope (FOCAS IFU; Ozaki et al., 2014; Kashikawa et al., 2002), observing Lyα nebulae around normal star-forming galaxies at high redshift has become feasible. Through stacking analysis of narrow-band images which contain the redshifted Lyα emission line of star-forming galaxies, Hayashino et al. (2004) first clearly showed that Lyman break galaxies in the SSA22 protocluster at $z = 3.1$ have more extended Lyα emission than continuum emission. Steidel et al. (2011) also detected large Lyα halos around continuum-selected galaxies residing in three protoclusters at $z = 2.30$, 2.85, and 3.09 through stacking of 92 spectroscopically confirmed protocluster members (see Right panel of Figure 1.9) and argued that basically all star-forming galaxies at high redshift can be potentially classified as Lyα blobs if we have sufficient sensitivity. Numerous studies utilized stacking analysis are published after these seminal works (Matsuda et al., 2012; Feldmeier et al., 2013; Jiang et al., 2013; Momose et al., 2014), while Rauch et al. (2008) conducted an experiment to find low surface brightness Lyα emission with a 92-hour long-slit spectroscopy with VLT/FORS2, resulting in 27 faint Lyα emission at $2.6 < z < 3.8$. By stacking a large number of images of Lyα emitters (for example, $N_{\rm LAE} \sim 700$ in Momose et al. 2016 and $N_{\rm LAE} \sim 1400$ in Xue et al. 2017), the limiting sensitivity goes to as low as $\lesssim 10^{-19}$ erg s^{-1} cm^{-2} arcsec^{-2}, roughly equaling that of Rauch et al. (2008). The advent of the MUSE on the VLT change the situation; it succeeded in routinely detecting Lyα halos around individual high-redshift galaxies (Wisotzki et al., 2016; Leclercq et al., 2017). With these techniques, various correlations between Lyα halos and galaxy properties e.g. UV magnitude, Lyα luminosity and equivalent width, and environments they reside have been studied.

The past a few years have also seen remarkable success in detecting Lyα halos around radio-quiet QSOs with MUSE and KCWI (Borisova et al., 2016; Arrigoni Battaia et al., 2019; Cai et al., 2019). Borisova et al. (2016) showed that the brightest radio-quiet QSOs at $z > 3$ ubiquitously have giant (> 100 pkpc) Lyα nebulae when seen with IFU,

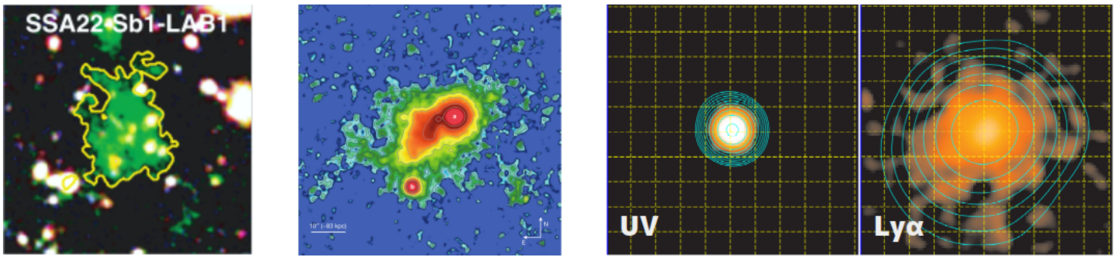

Figure 1.9: Cutout images of various class of Lyα nebulae. (Left) Pseudo-color image of Lyα blob (LAB) at $z = 3.1$ (V band for red, a narrowband filter NB497 for green, and B band for blue; Matsuda et al., 2011). The size of the image is 40×40 arcsec^2 ($\sim 300 \times 300$ pkpc^2 at $z = 3.1$). (Middle) Lyα image of a luminous QSO at $z = 2.3$, UM 287 (Cantalupo et al., 2014). This nebula has been called "the Slug Nebula". The scale bar at the bottom left of the figure corresponds to an angular scale of 10 arcsec. The maximum projected physical size of the nebula above 2σ isophotal contour is as large as 460 pkpc. (Right) Stacked UV and Lyα images of 92 protocluster LBGs (Steidel et al., 2011). The size of the image is 20×20 arcsec^2 ($\sim 160 \times 160$ pkpc^2 at $z = 2.65$) with logarithmically spaced contours. Lyα emission is clearly more extended than UV (stellar continuum) light.

which do not suffer from slit loss or difference between narrow-band coverage and QSO's true systemic redshift. These findings suggest that bright QSOs have a large amount of cold gas within their halos and it is powered by strong ionizing radiation of QSOs. Moreover, by using QSOs as a flashlight, even the IGM gas disconnected from QSO halos must be become visible above the detection limit, clear evidence of which had not yet been obtained until quite recently (Umehata et al., 2019). That probably is enabled by elevated ionizing photon flux in the core of the protocluster SSA22 at $z = 3.1$ where the number density of AGNs and SMGs (along with other ordinary populations) are much higher than usual.

Finally, we here comment on confusing jargon used in the literature, which is by no means well defined. The term "**Lyα nebulae**" is the most general one, covering all the populations which have extended Lyα emission. The term "Lyα halo (**LAH**)" can be used almost interchangeably. Practically, however, since the term "Lyα blob (**LAB**)" is specially used for Lyα nebulae with large size (usually, larger than a few tens of pkpc) and high luminosity (larger than $\sim 10^{43}$ erg s^{-1}), "LAH" is used for more diffuse emission than that around LABs in most cases. "Lyα emitter (LAE)" and "Lyman break galaxy (LBG)" are two of the most frequently used acronyms in high-redshift galactic astronomy and are just names of galaxy populations as we explained in Section 1.4. These are used irrespective of Lyα nebulae around them.

1.6 This Thesis

The IGM and CGM are frontiers of galactic astronomy, as we described in Section 1.5. There remains a lot of things to be done, including more definite detection of Lyα emission from the cosmic web of the IGM. And beyond just a detection, further characterizations of the cosmic web gas is definitely needed to directly test the favored scenario of galaxy formation today. Moreover, despite many efforts, properties of Lyα halos (LAHs) are still not well understood. Especially, studies in the literature provide controversial results about the dependence of LAHs of LAEs on local environments; Steidel et al. (2011) found very large LAHs around LAEs in protoclusters and Matsuda et al. (2012) found that the extent of LAHs are proportional to local galaxy number density squared, while Xue et al. (2017) found no evidence for such dependence.

We tackle these issues with newly taken deep images which cover a field around a protocluster at $z = 2.845$. This protocluster is found through a spectroscopic follow-up of LBG overdensity around a "hyperluminous" QSO at the same redshift (Steidel et al., 2011; Mostardi et al., 2013). Such a bright QSO acts as a flashlight to light up the otherwise too faint cosmic web. By targeting at the known protocluster which has bright QSOs, we expect a higher probability of detecting the Lyα emission from the cosmic web. At the same time, we can obtain LAEs reside in the densest environments, which is rarely possible with survey data targeting blank fields. Through this project, we first aim **(1)** to detect the IGM in emission to test the validity of the cold-mode accretion scenario. We also aim to establish the relation between the IGM and large-scale environment. Next, we try **(2)** to determine if LAHs depend on the environment they reside in. Wide-field narrow-band imaging with the HSC can investigate both topics very efficiently, connecting kpc-scales to Mpc-scales.

In Chapter 2, we focus on the large- and small-scale properties of Lyα emission from the field. LAEs are used to probe the large-sale structure of the Universe at $z = 2.85$. Then, the distribution of LABs in relation to the large-scale structure is studied. On smaller scales, Mpc-scale diffuse Lyα emitting structure was revealed around the HLQSO. We argue the origin of the emission and claim that one of the diffuse nebulae near the HLQSO represents the dense part of the cosmic web. In Chapter 3, we describe our analysis of LAHs of LAEs detected in the same field. The depth and wide field coverage of our data enable us to argue the dependence of LAHs on environments with unprecedented depth and sample size at $z \sim 3$. Combining our results and those in literature, we conclude that the dependence of LAH shapes of LAEs on large-scale environments is minor. At last, in Chapter 4, we highlight the main result presented in the above Chapters and briefly discuss how the results of Chapter 2 and Chapter 3 are interpreted altogether. Also, we present future direction to further study the IGM and CGM, and galaxy formation at the densest environments.

Throughout this thesis, we use the AB magnitude system and assume a cosmology with $\Omega_{\rm m} = 0.3$, $\Omega_\Lambda = 0.7$, and $H_0 = 70$ km s^{-1} Mpc^{-1}, unless otherwise noted.

2

Lyα view around a Hyperluminous Quasar at a Node of the Cosmic Web

—Based on Kikuta et al. (2019)

2.1 Introduction

In the current framework of galaxy formation, accretion of cold gas from the intergalactic medium (IGM) through thin filaments (cold streams) is a crucial component which governs subsequent galaxy evolution (see Section 1.2; Kereš et al., 2005; Dekel & Birnboim, 2006; Dekel et al., 2009; Cen, 2014). Accreted gas from the IGM interacts with outflowing gas from galaxies in the circumgalactic medium (CGM, roughly referring to gas within a few times the virial radii of galaxies), regulating the galactic gas supply. Extended Lyα emission, or Lyα blobs (LABs; Steidel et al., 2000), are effective probes for studying the physical properties of the IGM/CGM, particularly for the overdense environment in which they tend to be found (Matsuda et al., 2004; Cen & Zheng, 2013;

Bădescu et al., 2017). While most LABs have obvious sources for their Lyα emission such as AGNs and starbursts (e.g., Overzier et al., 2013; Prescott et al., 2015), some with filamentary morphology might also be related to cold streams (Goerdt et al., 2010; Faucher-Giguère et al., 2010).

Matsuda et al. (2011) suggested a possible relation between LAB morphology and Mpc-scale environments. Erb et al. (2011) reported that six LABs in the HS1700+643 protocluster at $z = 2.3$ (Steidel et al., 2005) are distributed along two linear structures with position angles of each oriented along the same lines. Although these results suggest a link between LABs and the large-scale structure (LSS), whether or not this is a general trend is still not known due to a lack of very deep and wide observations.

In this Chapter, we present a new example of such a field suggesting a correlation between the LSS and Lyα emission, around a hyperluminous QSO (HLQSO) HS1549+1919 at $z = 2.84$. Previous galaxy redshift surveys have revealed a massive protocluster around the HLQSO (Steidel et al., 2011; Trainor & Steidel, 2012; Mostardi et al., 2013). With new wide-field imaging data obtained with the Hyper Suprime-Cam (HSC; $\phi = 1.5°$, Miyazaki et al., 2012) on the 8.2m Subaru Telescope, we were able to trace structures on > 100 comoving Mpc (cMpc) scales around the HLQSO. Additionally, the HSC images led us to discover Mpc-scale Lyα emission surrounding the HLQSO, which may be enhanced due to the unusual QSO activity within a small region.

2.2 Observations and Data Reduction

We observed the field centered on HS1549+1919 ($15^{\mathrm{h}}51^{\mathrm{m}}52.^{\mathrm{s}}47$, $+19°11'04.''0$ (J2000.0), $z = 2.843$, $L_{1450} = 1.5 \times 10^{14} L_{\odot}$, Trainor & Steidel 2012), with Subaru/HSC on 2016 June 2–3 (UT; Program ID: S16A-110, PI: Y. Matsuda). We used a g-band ($\lambda_{\mathrm{c}} = 4712$Å, $\Delta\lambda = 1479$Å) and a narrow-band filter NB468 ($\lambda_{\mathrm{c}} = 4683$Å, $\Delta\lambda = 88$Å). As shown in Figure 2.1, the NB468 filter can capture the Lyα emission from $z = 2.815$-2.887 while the g-band can additionally detect continuum emission from those emitters. We took images with short exposure time (20 sec for g and 200 sec for NB468 [1]) to avoid saturation of the HLQSO and with 5-point dithering (RDITH= 600”) and 12 different position angles to reliably extract diffuse emission minimizing the sky contamination.

---

[1] We confirmed that the noise level of individual images are sky limited rather than dominated by readout noise.

We stacked, respectively, 389 and 113 individual exposures (total of 2.2 hrs and 6.3 hrs, respectively) to produce final g-band and NB468 images.

The raw data were reduced with HSC pipeline[2] version 4.0.5 (Bosch et al., 2018), using additional packages for ghost and satellite masking[3] and global sky subtraction[4], which estimates and subtracts the sky on scales larger than that of individual CCDs in the mosaic with a grid size of 6000 pixel (17′). Additionally, we manually masked obvious artificial signals that are not masked through automated procedure described above, such as CCD defects. Astrometry and photometric zero points were calibrated using Pan-STARRS1 catalogs (Schlafly et al., 2012). The FWHMs of stellar sources in the stacked images are 0.″77 and 0.″65 in g-band and NB468, respectively. The NB468 image was smoothed to match the FWHM of stellar sources in the g-band image. After correction for Galactic extinction of $A_{\mathrm{g}} = A_{\mathrm{NB468}} = 0.17$ mag (Schlegel et al., 1998) and subtraction of a residual local sky, a 5σ limiting magnitude measured with 1.″5 diameter aperture is 27.4 (26.6) mag for g-band (NB468) image. As the S/N ratio near the edge of the images becomes lower, we only use a 72′ diameter circular region centered at the HLQSO for the analysis below.

We used photometric criteria below to select LAE at $z = 2.815$–2.887:

$$\mathrm{g} - \mathrm{NB468} > \max(0.5, 0.1 + 4\sigma(\mathrm{g} - \mathrm{NB468})) \tag{2.1}$$

$$\mathrm{NB468} < 26.6 \tag{2.2}$$

where $\sigma(\mathrm{g} - \mathrm{NB468})$ denotes the expected 1σ deviation of the quantity $\mathrm{g} - \mathrm{NB468}$ for a flat continuum (f_ν =const.) source. The criterion $\mathrm{g} - \mathrm{NB468} > 0.5$ corresponds to $\mathrm{EW_{obs}} > 59$Å. For objects fainter than 2σ in the g-band, we replace their g-band magnitude by their 2σ limiting magnitude as a lower limit. SExtracor (Bertin & Arnouts, 1996) was used to perform 1.″5 aperture photometry with double-image mode, with the NB468 image used as the detection band. We set a background mesh size of 64 pixels (= 11”) to estimate local sky values. Spurious detections such as diffraction spikes around bright stars and cosmic rays are excluded. As a result, we detected 3490 LAEs within $r < 36'$ from the QSO position. Figure 2.2 shows the distribution of

---

[2] https://hsc.mtk.nao.ac.jp/pipedoc_e/

[3] https://hsc.mtk.nao.ac.jp/pipedoc_e/e_tips/ghost.html

[4] https://hsc.mtk.nao.ac.jp/pipedoc_e/e_tips/skysub.html#global-sky

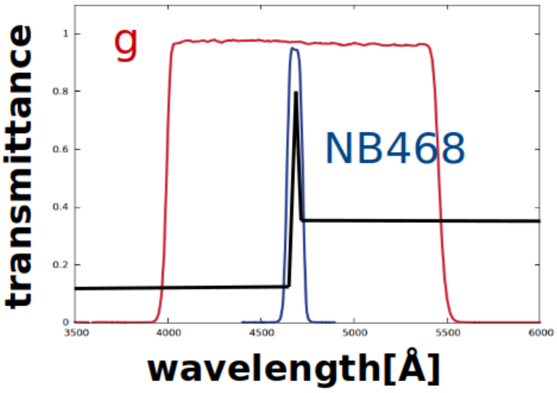

Figure 2.1: Transmission curves of NB468 and g-band filters. Black curve indicates typical spectrum of LAE at $z = 2.84$.

selected LAEs on the color-magnitude diagram along with all the detected objects. A contamination rate of this selection should be quite low ($\lesssim 3\%$), according to extensive spectroscopic follow-up by Trainor et al. (2015) and Steidel et al. in prep. Like us, they utilized a selection method in which only one broad-band magnitude (G-band of Keck/LRIS) was used along with a NB filter (NB4670 of Keck/LRIS) to estimate the continuum luminosity. All the confirmed contaminants in their entire survey (including various fields at $2.57 < z < 2.85$) were low-redshift AGNs with the strong CIV λ1549 line at $z \sim 1.9$ and HeII λ1640 line at $z \sim 1.7$, the number density of which are much lower than LAEs at $z \sim 2.8$. Indeed, within the $\sim 7' \times 6'$ field centered at the HLQSO, all of our sample which have been spectroscopically followed up by them (82 sources) are LAEs at $z = 2.82$–2.88[5].

We also selected extended LAEs or Lyα blobs (LABs) using an additional criterion on their isophotal areas on the Lyα image. A pure Lyα image was created by subtracting the g-band image from the NB468 image after scaling by their relative zero points. The g-band overlaps with the NB468 and this has the slight effect ($\sim 6\%$ at the NB center) of an oversubtraction. We smoothed the Lyα image to reduce noise with gaussian kernel $\sigma = 3$ pixel or 0.″5 (FWHM 1.″2). LABs were selected as objects which satisfy Equation (2.1) and (2.2), and in addition have 2σ (28.36 mag arcsec^{-2}) isophotal areas larger than

---

[5] Of course, the contamination rate derived around the HLQSO would be underestimated due to the existence of the protocluster. Still, the fact that all of our source are confirmed to be around $z \sim 2.85$ is reassuring.

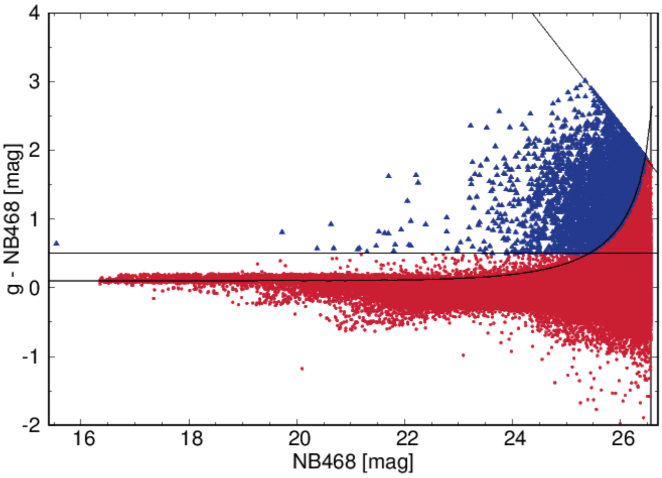

Figure 2.2: Distribution of sources in a color-magnitude diagram in the field. Blue triangles denote sources selected as LAEs at $2.815 < z < 2.887$, while red points denote all the detected sources. Curves outline the selection criteria as shown in Equation 2.1 and 2.2. Sources on the diagonal line at upper-right have $g > g_{2\sigma}$. The triangle with NB468 $\sim$ 15.5 is the hyperluminous QSO. Sources with g − NB468 ~ -1 and NB468 $\sim$ 20 and 23 are respectively a cosmic ray in the g-band image which is not excluded in our inspection process and a low-z interloper. Although other fainter sources with negative g − NB468 should include galaxies at $z \sim 2.85$ with strong Lyα absorption line, we defer a detailed analysis on these sources since we used the NB468 image as a detection band here.

16 arcsec^2 in the Lyα image. For those extended sources, we used the isophotal area to calculate the color, and a background mesh size of 176 pixels (30”) was used for local sky estimation. These criteria were chosen to be consistent with those used by Matsuda et al. (2004). To put this criteria into context, we showed the distribution of isophotal areas of LAEs in the Lyα image in Figure 2.3. After rejecting obviously spurious detections, we detected 76 LABs in the field. We showed Lyα images of these LABs in Figure 2.4, Figure 2.5, and Figure 2.6.

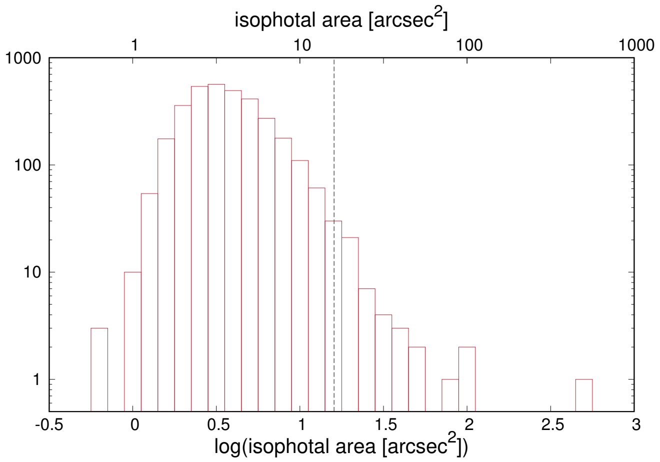

Figure 2.3: Histogram of isophotal area of LAEs in the Lyα image. Vertical dashed line indicates 16 arcsec^2.

2.3 Results

2.3.1 Distribution of LAEs and LABs

Figure 2.7 shows the spatial distribution of LAEs/LABs around the HLQSO, overlaid on the number density map of LAEs measured with the "fixed aperture method": we measured a local density of LAEs by counting their number n within a fixed aperture. Then we calculated the average $\bar{n}$ and overdensity δ as $\delta \equiv (n - \bar{n})/\bar{n}$. The value of δ depends strongly on the (arbitrarily chosen) aperture radius. Here we used an aperture radius of $1\farcm8$ (or 0.83 pMpc) to be consistent with the measurement of Matsuda et al. (2012) and Yamada et al. (2012).

The HLQSO is located at the origin in Figure 2.7. Two arm-like structures extend toward the north-east and north-west, revealing that the HLQSO lies near their intersection. LABs are distributed along the structure, avoiding the huge void to the south of the protocluster. The distribution of δ for LAEs and LABs is presented in Figure 2.8. As previously noted, a clear trend of LABs favoring denser environments is seen in both Figure 2.7 and in the cumulative distribution function in Figure 2.8. We performed a two-sample Kolmogorov-Smirnov test and obtained a p-value of 0.0017. Even if we only consider LAEs and LABs with $\delta < 2.5$ (those out of the protocluster) a p-value remains low ($p = 0.011$). This trend becomes even clearer for larger LABs; of

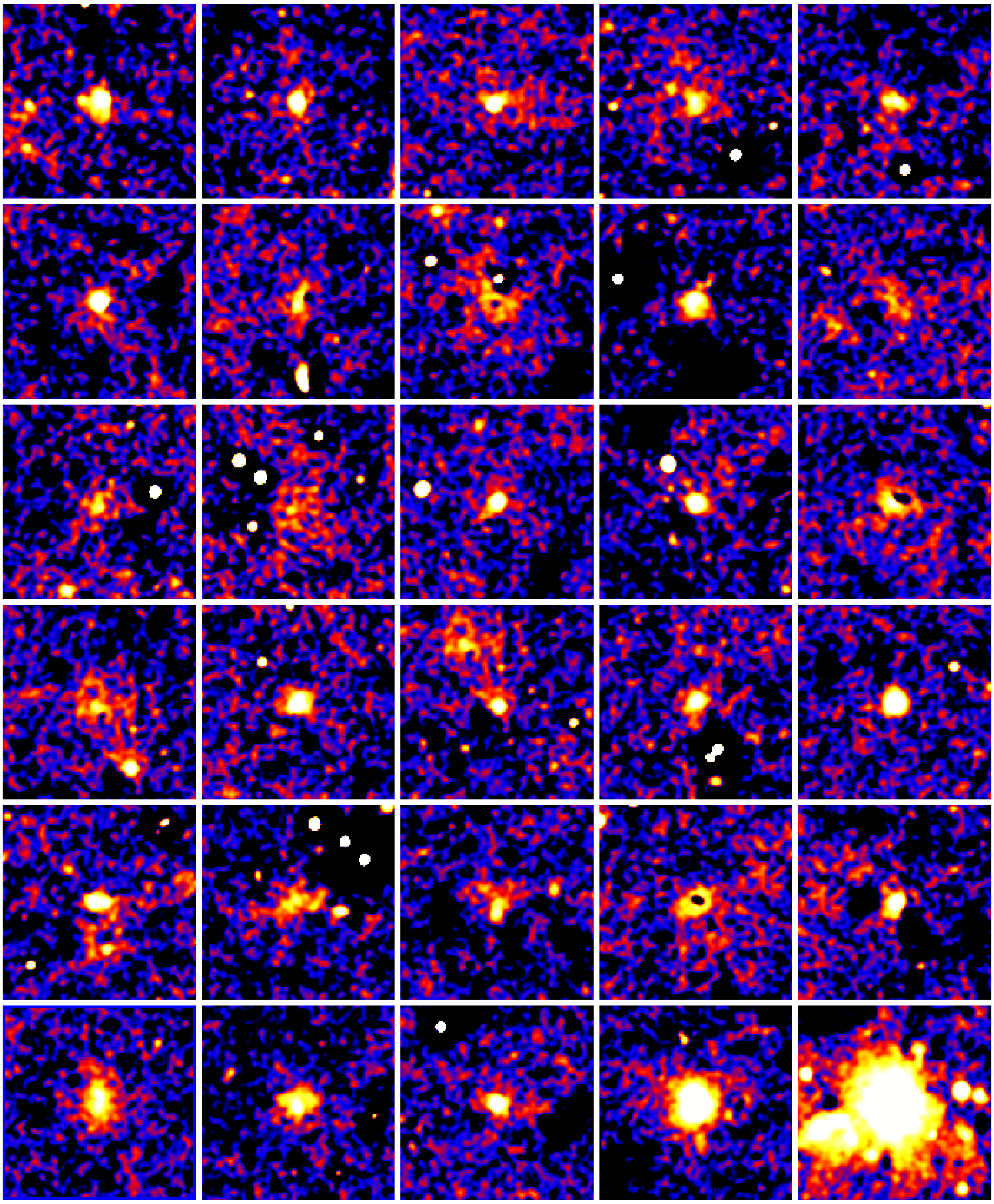

Figure 2.4: Lyα image of detected LABs. The images are smoothed with gaussian kernel $\sigma = 3$ pixel. The size of each panel is 300 pkpc × 300 pkpc.

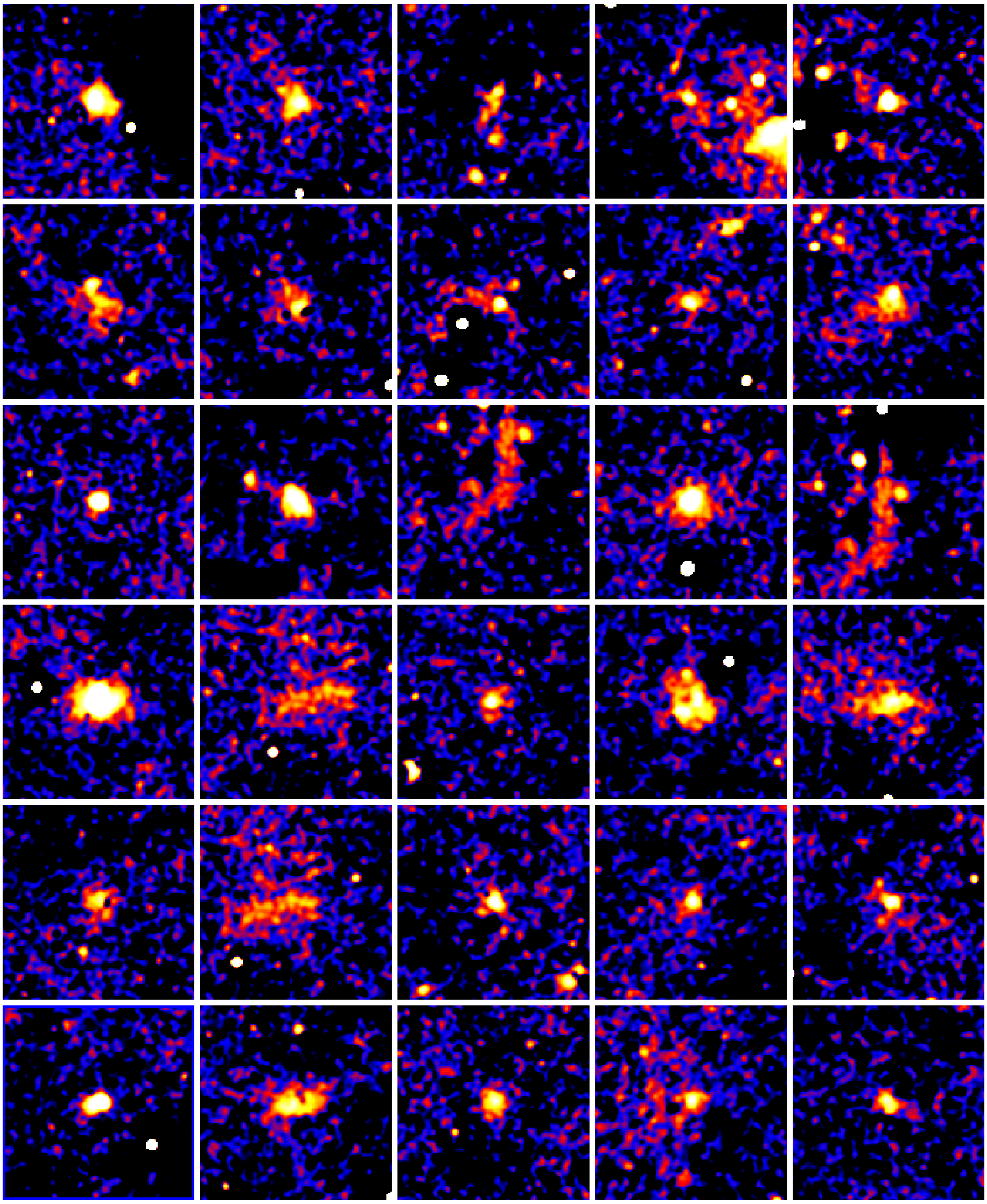

Figure 2.5: Lyα image of detected LABs. See the caption of Figure 2.4 for details.

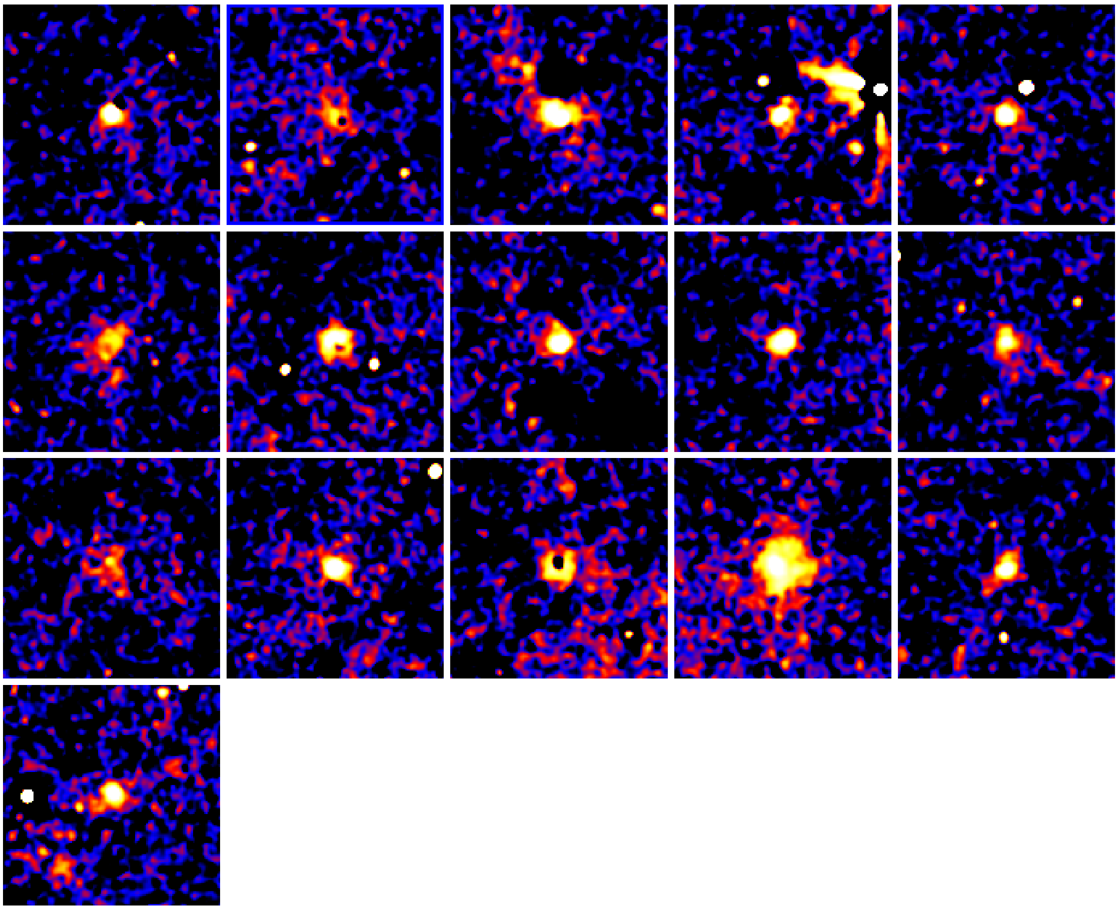

Figure 2.6: Lyα image of detected LABs. See the caption of Figure 2.4 for details.

eight LABs with isophotal area > 50 arcsec^2, four are located within 1.5 pMpc (see Figure 2.9) of the HLQSO, and one lies only 2.7 pMpc away. The number density of LABs averaged over the entire field is 7.8×10^{-5} cMpc^{-3} using the survey volume (dictated by the field of view and width of the NB468, $\Delta z = 0.075$ or equivalently $d_C = 73$ cMpc) of $\sim 10^6$ cMpc^3 without any correction. This is an order of magnitude higher than that observed in random fields at $z = 2.3$ (Yang et al., 2010), largely because of the difference in sensitivity. A survey by Matsuda et al. (2004) targeting the SSA22 protocluster at $z = 3.1$ found 35 LABs within a $31' \times 23'$ field (1.3×10^5 cMpc^3) with similar sensitivity and criteria to ours, resulting in $\sim 2.7 \times 10^{-4}$ cMpc^{-3}. If we use the same $31' \times 23'$ window centered at the QSO location, we obtain $\sim 1.4 \times 10^{-4}$ cMpc^{-3} for the HS1549 field. Note, however, these values are sensitive to the window size and the extent of the protoclusters. Within a 4 pMpc diameter aperture (a typical size for protoclusters at $z \sim 3$, Chiang et al., 2013), the number density is a factor of 5 higher.

2.3.2 Lyα Emission around the HLQSO

A close-up smoothed Lyα image around the HLQSO is shown in Figure 2.9, using a background subtraction mesh size of 30” (235 pkpc). We confirmed nebulae discussed below persist with larger mesh sizes of $1'$ and $2'$. This is also checked with two images made by splitting 113 NB468 exposures into two and separately stacking them. Also, we checked no dubious negative pattern exists at their location in the g-band image which could produce spurious nebulae in the Lyα image.

The HLQSO is the brightest source near the center. An enormous Lyα nebula around the QSO reported in Martin et al. (2014) is clearly seen. Although not connected to this main nebula, there is a chain of diffuse Lyα emission toward the south (marked as “tail”), comprising a Mpc-scale Lyα structure. No source is detected as an LAE within the tail except for the one at the tip. We caution that, however, some parts of the tail are only significant at 1-2σ levels.

In this $5' \times 3.'5$ image, 10 sources are detected as LABs (green squares), most of which have a size of > 100 pkpc. The distribution and shapes of LABs appear to broadly follow the LSS toward north-east and north-west in Figure 2.7, although the alignment is not as obvious as that described by Erb et al. (2011). Similar to the tail,

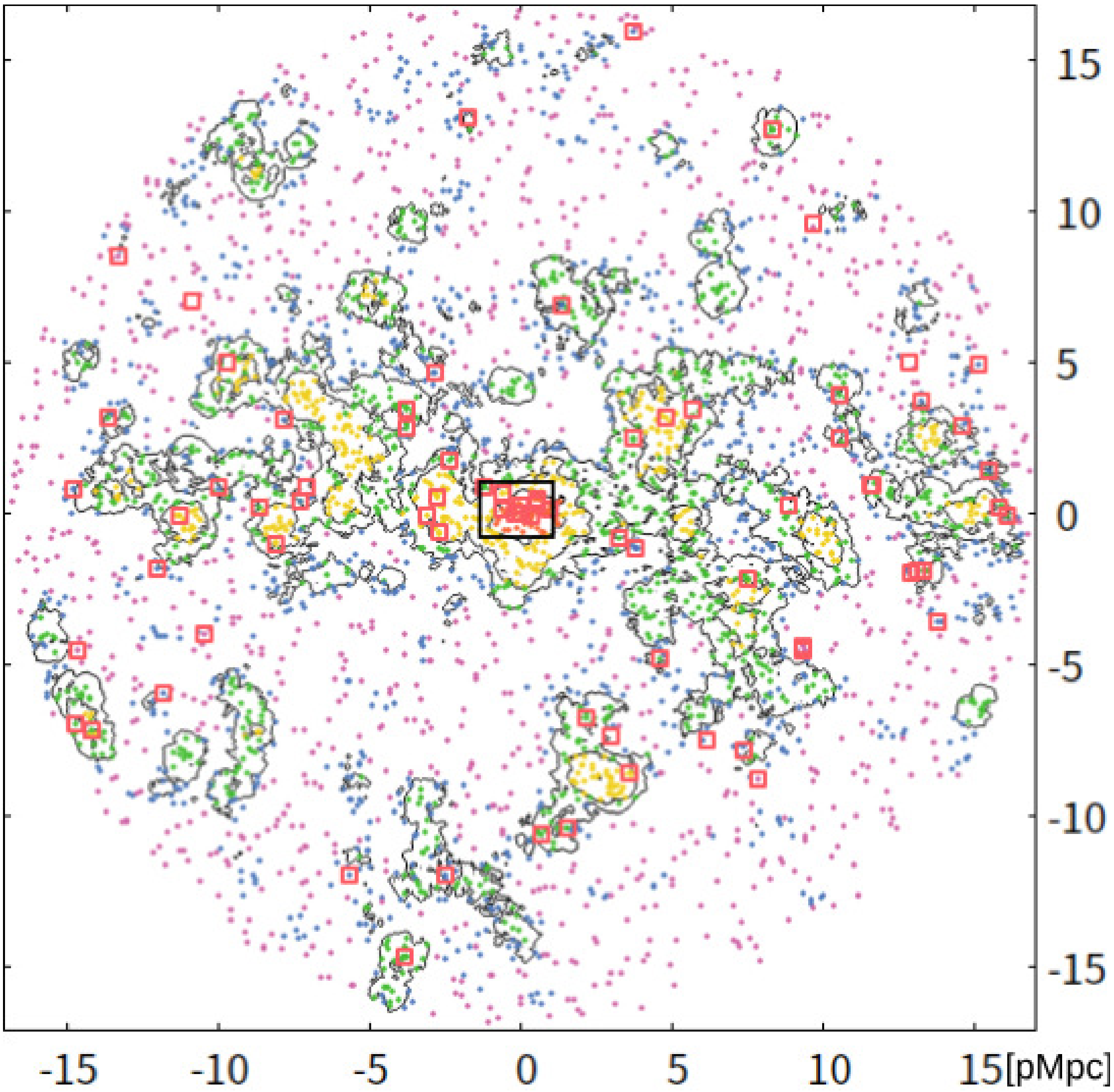

Figure 2.7: Spatial distribution of LAEs at $z = 2.84$ with north up and east left. The origin (0,0) is set to the QSO location. Colored points denote selected LAEs, with their colors reflect local environments they reside (see Figure 2.8). Red squares denote LABs. Black contours are LAE overdensity $\delta = 0.3, 1, 2.5$. Black rectangle shows the area highlighted in Figure 2.9. 5pMpc corresponds to an angular scale of 10′.7.

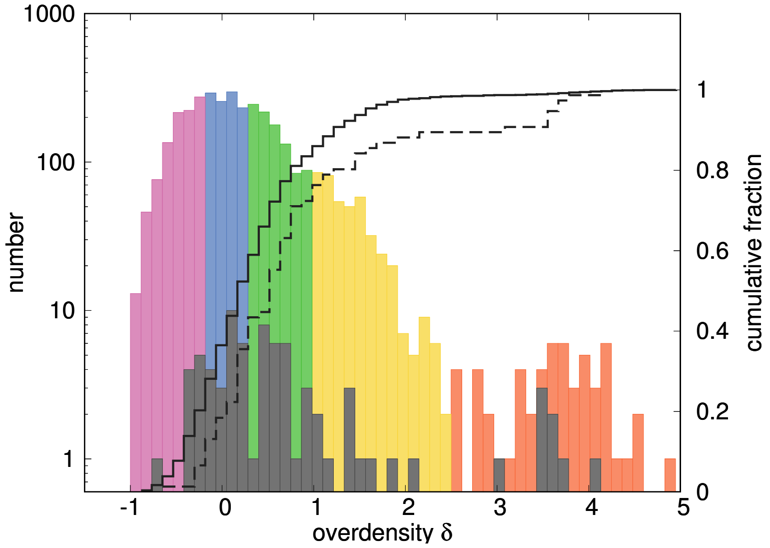

Figure 2.8: Distribution of δ. Color (gray) boxes indicate the distribution for LAEs (LABs). Solid line shows a cumulative distribution function of δ for LAEs while dashed line shows that for LABs, which is clearly skewed toward the right-hand (thus denser) side.

diffuse emission to the north-west of the HLQSO (marked as "filament")[6] has no LAE counterpart except for the one at the north end, despite its total Lyα luminosity of $\sim 10^{43.3}$ erg s^{-1}. If powered by star formation, SFR = 12 $M_\odot$ yr^{-1} is required, using calibration of Murphy et al. (2011) and Lyα/Hα = 8.7. There are two UV sources with g = 25.6 and 25.8 mag with g − NB468 $\sim$ 0 just outside of the 2σ SB contour. Even if they are both at the same redshift as the filament, their combined SFR amounts to only $\sim 7\ M_\odot$ yr^{-1}.

To check the robustness of our detection of these nebulae, we split 113 individual NB468 exposures into two groups (56 and 57 images each) and separately stack them, and then subtract new g-band images which are generated in the same manner. Although some details are lost, most features persist, assuring that the emissions have astrophysical origins rather than artificial ones. The filament is also barely visible in the Lyα image created from an NB4670 image and a V-band image taken with Keck/LRIS (Mostardi et al. 2013; Steidel et al. in prep.).

---

[6] These are originally selected as two separated LABs. We regard it as one hereafter.

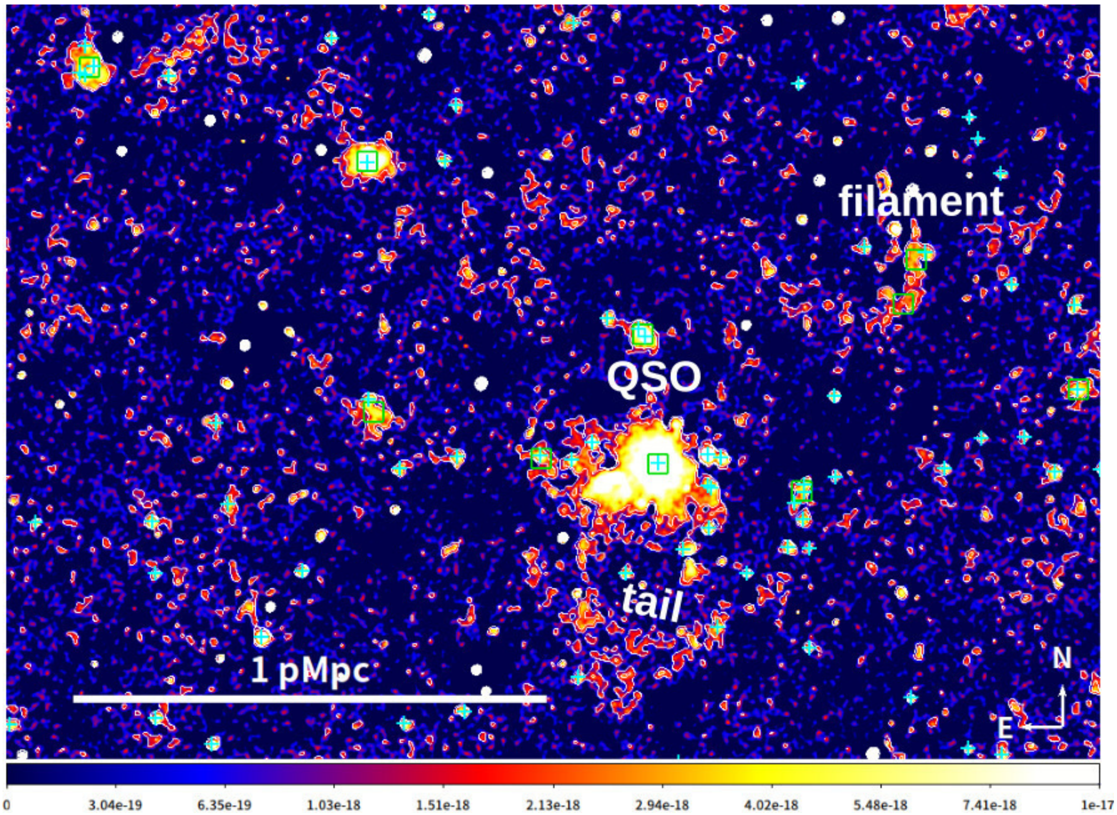

Figure 2.9: Cutout Lyα image showing the $5' \times 3'.5$ area around the HLQSO with north up and east left. Cyan crosses (green squares) denote objects selected as LAEs (LABs). Color bar indicates Lyα brightness in erg s^{-1} cm^{-2} arcsec^{-2} using an asinh stretch. White contours correspond to 1×10^{-18} and 2×10^{-18} erg s^{-1} cm^{-2} arcsec^{-2} (respectively correspond to $\sim 1\sigma$ and 2σ).

2.4 Discussion

2.4.1 Significance of Overdensity

To estimate descendant halo mass of this protocluster, we compare our results with those of Chiang et al. (2013), who provided the relation between overdensity δ of galaxies at $z = 3$ and descendant cluster total mass (see their Figure 13). We used a circular aperture radius of 8.46 cMpc and LAEs with $L_{\rm Ly\alpha} > 10^{42}$ erg s^{-1} to match the area of square aperture they provided (15×15 cMpc^2) and their SFR threshold of $> 1\ M_\odot$ yr^{-1}. In our case, we measured peak value of $\delta_{8.46\rm cMpc} = 2.0$ with the redshift uncertainty of LAEs of $\Delta z = 0.075$, making the HS1549 field a highly reliable progenitor of Coma-type ($M_{\rm halo} > 10^{15} M_\odot$) cluster. A similar conclusion is reached by examining the overdensity of continuum-selected galaxies in the KBSS spectroscopic sample (C. Steidel, et al., in prep.). At $z \sim 3$, the most massive halos could have $M_{\rm halo} \sim 10^{13} M_\odot$. These redshift and halo mass are respectively lower and upper limit where cold streams can penetrate through growing hot media (Dekel & Birnboim, 2006), possibly enabling extreme starburst and SMBH activity around the QSO.

2.4.2 Possible Origin of Diffuse Nebulae

It is interesting to consider the origin of the two mysterious nebulae, namely the "tail" and "filament" in Figure 2.9. Interestingly, they both have few LAEs within them. The overall shape of the tail is reminiscent of tidal features in nearby galaxies, albeit an order of magnitude size difference. They could be remnant features of mergers and interactions with the main halo which are distributed prior to the onset of the HLQSO. Another possibility is that they trace cold streams/filaments. This scenario seems incompatible for the tail with its large curvature and the fact that there is no large-scale structure of LAEs to the south. By contrast, the thin shape, orientation pinpointing the HLQSO, and alignment with the LSS of the "filament" is consistent with expectations for cold streams or filaments along the LSS, though whether it is "streaming" toward the halo center or not is unclear at this stage. It is located at ~ 650 pkpc (projected, $\sim 3 \times R_{\rm vir}$) away from the QSO while the virial shock must develop much closer to the halo center and thus it is hard to say that it is related to cold-mode accretion onto the host halo of the QSO. One mystery then arises is the absence of emission between the QSO and the filament. This absence may be explained by a variability, anisotropy of QSO illumination and/or a local lower density region, which then simultaneously provides the required illumination of the filament by the QSO discussed in the following paragraph. The observed mild curvature of the filament is not unexpected as is also seen in some numerical simulations (Rosdahl & Blaizot, 2012). To confirm if it is flowing toward a halo center, we clearly need more information such as the velocity field, temperature and density. A part of them can be obtained with our planed IFS observations with Keck/KCWI (see Section 4.3.1).

The configuration and position angles of other LABs are also roughly aligned with the LSS. Specifically, 5 LABs to the north and east of the QSO showed $\cos\theta > 0.8$, where θ is the angle between their major axis and the line to the QSO, while if their orientations are randomly distributed there is 1% chance for this to happen. This suggests enhanced cold gas accretion and interactions along the structure efficiently distribute gas around galaxies and activate AGNs/starbursts which light up the gas, making it visible as LABs. Indeed, three brightest LABs in Figure 2.9 (the HLQSO itself and the two to the north-east) are associated with either SMG (the eastmost one, Lacaille et al., 2018) or QSOs, with three more AGNs within just 150 pkpc from the HLQSO, suggesting enhanced interactions (C. Steidel et al. 2019, in prep.).

Because no counterpart is identified within the filament at present, the origin of the Lyα emission is ambiguous — possibilities include obscured galaxies, gravitational cooling, scattering of Lyα photon from the HLQSO, or photoionization by ionizing photons from the HLQSO ("QSO fluorescence", e.g., Kollmeier et al., 2010). Lacaille et al. (2018) conducted JCMT/SCUBA2 observations with 0.6 mJy beam^{-1} sensitivity at 850 μm (corresponding to SFR $\sim 45\ M_\odot\ \mathrm{yr}^{-1}$) for this field. They found a source with a few mJy at 850 μm near the filament, but it is at ~ 10" away and at present has no redshift information, leaving it unconvincing as a power source. If the sub-mm source is confirmed to be a member of the protocluster, then the filament can be used to determine whether gas is cold or hot just before entering into high-redshift halos. Fainter SMGs can still explain observed $L_{\mathrm{Ly}\alpha}$ and need to be constrained in the future (see Section 4.3.2). The contribution of gravitational cooling to the Lyα emission, though still difficult to predict due to its exponential dependence on temperature, can in principle be large enough to be detected (e.g., Goerdt et al., 2010; Rosdahl & Blaizot, 2012) but only within $\sim R_{\mathrm{vir}}$ from the massive ($M_{\mathrm{halo}} > 10^{12}$) halo center in most cases, hence this mechanism is unlikely at the location in question if the sub-mm source is not a protocluster member. Considering the luminosity of the HLQSO and assuming the gas sees the QSO radiation, hydrogen in the filament should be almost ionized except for dense parts. Thus, the most promising power source at this stage is QSO fluorescence.

We crudely estimate the plausibility of this scenario. The ionizing photon production rate from the HLQSO is estimated as $\dot{N} = 10^{58}$ s^{-1} using the observed UV luminosity of $\nu L_{\nu,1450} = 1.5 \times 10^{14} L_{\odot}$ and assuming UV continuum slope of ν^{-1}. Modeling the filament as a column with a height of 200 kpc and a diameter of 50 kpc, the amount of ionizing photon available to the filament at the distance of 650 kpc is $\Omega/(4\pi) \cdot \dot{N} = 2 \times 10^{56}$ s^{-1} or equivalently $L_{\mathrm{Ly}\alpha} = 2 \times 10^{45}$ erg s^{-1}, which can power the observed luminosity of the filament, $L_{\mathrm{Ly}\alpha} = 2 \times 10^{43}$ erg s^{-1}. The predicted HI fraction can be written as $Cn_{\mathrm{e}}\alpha/\Gamma = 4 \times 10^{-4} Cn_{\mathrm{e}}$, where C is the clumping factor, n_{e} is the electron density [cm^{-3}], and $\alpha = 2.6 \times 10^{-13}$ cm^3 s^{-1} denotes the case-B recombination rate at temperature of 10^4 K, and Γ denotes the photoionization rate [s^{-1}]. Under these assumptions, the luminosity of the filament will be roughly $L_{\mathrm{Ly}\alpha} = 0.68 h\nu_{\mathrm{Ly}\alpha} \times Cn_{\mathrm{e}}^2 \alpha V = 3 \times 10^{46} Cn_{\mathrm{e}}^2$ erg s^{-1}, where $h\nu_{\mathrm{Ly}\alpha}$ is the energy of Lyα photon and V is the assumed total volume of the structure. As an example, $C \sim 10^3$ with a density $n_{\mathrm{e}} \sim 10^{-3}$ cm^{-3}, corresponding to about 100 times the mean baryon density at $z = 2.84$, could explain the luminosity of the filament.

How is this high clumping factor achieved? We advocate a mechanism where the high clumpiness of gas in the filament is due to the CGM of a significant number of faint halos of mass in the range of $\leq 10^{9-10} M_{\odot}$. Regions just around self-shielded spheres where density is sufficiently high are ionized by the QSO and emit Lyα photons which are then scattered by residual HI gas in the filament. We will detail this model in a separate paper (Cen et al. in prep.; see also Figure 4.1 below for a schematic picture). Additionally, the sub-kpc scale structure in the CGM/IGM suggested in some observations (e.g., Rauch et al., 1999; Schaye et al., 2007; Hennawi et al., 2015; Cantalupo et al., 2019) may drastically change its emission properties (e.g., Corlies et al., 2018; Peeples et al., 2018; Suresh et al., 2019; van de Voort et al., 2019). Current cosmological simulations lack sufficient resolution to resolve such scales. These small-scale clumps, if proven to exist in substantial abundance even in the IGM, may change the above scenario.

2.5 Summary

In this Chapter, we have reported the results of our wide-field Lyα imaging around the HLQSO HS1549+1919 at $z = 2.84$ with Subaru/Hyper Suprime-Cam. We were able to map the large-scale structure traced by Lyα emission on > 100 cMpc scales and probe diverse environments from voids to protoclusters within a single pointing of HSC, clearly displaying its power (Figure 2.7). Furthermore, we identified a variety of Lyα nebulae near the central part of the protocluster centered on the HLQSO. What especially stand out in this field are the significant overdensity of LABs, their apparent alignment with that of the large-scale structure, and the existence of the "filament", that may be ambient gas illuminated by the HLQSO (Figure 2.9). These results suggest enhanced interactions which redistribute gas around galaxies and abundant cold gas in the densest environments at cosmic noon. With a help of QSO fluorescence, more LABs similar to the filament will be found. A detailed comparison with integral field spectroscopy datacubes of such LABs and numerical simulations will clarify their true nature and shed light on crucial gaseous phenomena which drive galaxy evolution.

3

Lyα Halos across Environments

In the previous Chapter, we mainly focused on Lyα blobs (LABs) and diffuse Lyα nebulae which are detected in the Lyα image individually and the relation between them and the large-scale structure. With the same datasets, we can probe the CGM of LAEs through stacking analysis. This Chapter will focus on LAEs in our field and investigate diffuse Lyα halos around them.

3.1 Introduction

Gas inflow from the cosmic web fuels star formation and AGN activity in galaxies. After these activity, galaxies expel a huge amount of gas as an outflow, thereby reducing further star formation and SMBH growth. The circumgalactic medium (CGM) have information of both of these components and thus very important to reveal how galaxies evolve. Recently, the CGM are routinely detected as extended Lyα nebulae or Lyα halos (LAHs) around star-forming galaxies at high redshift both individually (Wisotzki et al., 2016) and through image stacking technique (Steidel et al., 2011;

Momose et al., 2014). Numerous authors tried reproducing observed Lyα halos by taking account of various physics including gravitational cooling, scattering of Lyα photons, fluorescence (i.e., recombination due to external ionizing sources), and so on (Zheng et al., 2011; Dijkstra & Kramer, 2012; Lake et al., 2015). Properties of LAHs should be mainly determined by a combination of distribution of gas, sources of Lyα and ionizing photons, and the relative importance of various physical mechanisms described above.

LAHs are naturally expected to have significant dependence on environments in which galaxies reside (Zheng et al., 2011; Mas-Ribas & Dijkstra, 2016). However, the observational relation between LAHs and environments is not well established and even contradictory. There are studies which found that LAEs in denser environments have larger halos and suggested that their extents (measured by r_s in the fitting function of the form $\propto \exp(-r/r_s)$) are proportional to galaxy overdensity squared δ^2 (Steidel et al., 2011; Matsuda et al., 2012). Conversely, Xue et al. (2017) found no such dependence with LAEs in two overdense regions at $z = 2.66$ and $z = 3.78$. Because the possible relation between environments and LAH properties might be linked to well-established local relations such as density-morphology relation (Cappellari et al., 2011, see also Section 1.4), pursuing this relation in detail is of great interest of galactic astronomy.

One major problem is small sample size of previous works. While only a few studies investigated fairly large sample of LAEs with deep images ($N_{\mathrm{LAE}} > 2000$; Matsuda et al. 2012; Momose et al. 2014), others used insufficient number of LAEs, the images of which were taken with 4m telescopes ($N_{\mathrm{LAE}} \sim$ a few×100-1000; Feldmeier et al. 2013; Xue et al. 2017). Because Lyα nebulae are extremely faint ($< 10^{-18}$ erg s^{-1} cm^{-2} arcsec^{-2}), interpretation of relations derived with such poor dataset would be difficult. To alter this situation and to provide a firm observational basis for theorists, well-controlled statistical sample of LAEs is needed. We compiled information about previous observational studies in Table 3.1.

As already presented in Chapter 2, we recently obtained new deep narrow-band (NB468) data with Hyper Suprime-Cam toward HS1549 protocluster at $z = 2.843$. Just one pointing of HSC allowed us to detect 3490 LAEs and thus their LAHs can be better investigated. As shown in the bottom row of Table 3.1, the sample size of our study is the largest to date. This Chapter is structured as follows. In Section 3.2, we describe our LAE sample and how we divide them for the stacking analyses described in Section 3.3. The results of the analyses are shown in Section 3.4. Based on these, we present discussion in Section 3.5.

Field / Sample	Redshift	Environment	N_{gal}	Notes	Reference
O2	2.07	blank field	187	4m, 36hr, 50Å	Feldmeier et al. (2013)
C-O3	3.10		241	4m, 24hr, 50Å	
K-O3	3.12		179	4m, 16hr, 57Å	
LAB	2.66	$3.5 < \delta_{\mathrm{LAE}}$	29	4m, 8.3hr, 42Å	Xue et al. (2017)
		$1.4 < \delta_{\mathrm{LAE}} < 3.5$	139		
		$\delta_{\mathrm{LAE}} < 1.4$	86		
PCF	3.78	$2.0 < \delta_{\mathrm{LAE}}$	44	8m, 3hr, 201Å	
		$0.5 < \delta_{\mathrm{LAE}} < 2.0$	76		
		$\delta_{\mathrm{LAE}} < 0.5$	43		
SSA22, HS1549, HS1700	3.09, 2.85, 2.30	protocluster	92	10m, 17/5/22hr, 80/88/90Å	Steidel et al. (2011)
SSA22, GOODS-N, SXDS-C/N/S	3.1	$2.5 < \delta_{\mathrm{LAE}}$	130	8m, 5-10hr, 77Å	Matsuda et al. (2012)
		$1.5 < \delta_{\mathrm{LAE}} < 2.5$	273		
		$0.5 < \delta_{\mathrm{LAE}} < 1.5$	861		
		$-1\delta_{\mathrm{LAE}} < 0.5$	864		
COSMOS, GOODS-N/S, SSA22, SXDS	2.2	$0.5 < \delta_{\mathrm{LAE}} < 1.5$	1047	8m, 2-3hr, 94Å	Momose et al. (2016)
		$-1 < \delta_{\mathrm{LAE}} < 0.5$	348		
HS1549	2.85	$2.5 < \delta_{\mathrm{LAE}}$	55	8m, 6hr, 88Å	This thesis
		$1.0 < \delta_{\mathrm{LAE}} < 2.5$	433		
		$0.3 < \delta_{\mathrm{LAE}} < 1.0$	944		
		$-0.15 < \delta_{\mathrm{LAE}} < 0.3$	1076		
		$-1 < \delta_{\mathrm{LAE}} < -0.15$	982		

Table 3.1: Sample description of previous works who studied LAHs around star-forming galaxies at cosmic noon. Fourth column denotes the number of galaxies (either LAEs or LBGs) used for stacking analysis. Fifth column contains information about telescope apertures, exposure time with narrowband filters, and FWHMs of narrowband filters which cover the Lyα emission from the redshifts probed in each study.

3.2 Sample Description

We used the LAE sample constructed in Section 2.2. To study dependence of LAHs on various photometric galaxy properties, we divide LAEs into several groups according to the following five quantities. Summary can be found in Table 3.2.

1. UV magnitude.
2. Lyα luminosity.
3. Lyα equivalent width.

   These three quantities are not independent with each other. UV continuum luminosity is a good proxy for star formation rate. At the same time, Lyα luminosity is also a tracer of star formation rate, but its resonant nature makes interpretation difficult. More importantly, UV slope or hardness of UV emission is a strong function of age and metallicity, thus Lyα equivalent width changes accordingly (Schaerer, 2003; Hashimoto et al., 2017). In addition, there is a known relation between the EW distribution and UV limiting magnitude, known as “the Ando effect” (Ando et al., 2006). Moreover, Lyα emission can be powered by other mechanisms than star formation in the galaxies, such as gravitational cooling, shock caused by outflow, and recombination induced by nearby ionizing sources. As a tracer for star formation rate, UV magnitude is more robust to use here.

   Division in UV magnitude, Lyα luminosity, and Lyα equivalent width is done so that the number of LAEs in each subsample becomes almost the same ($N_{\mathrm{LAE}} \sim 700$).

4. Environment.

   Grouping based on environments is done rather physically motivated. This division is already illustrated in Figure 2.7 and 2.8. The boundary of $\delta = 2.5$ is set to only include protocluster members in the densest subgroup (see red points in Figure 2.7). The next boundary $\delta = 1$ is set by a trade-off between tracing sufficiently dense regions and including enough number for higher S/N when stacked (see yellow points in Figure 2.7). The rest is set to equalize the number of LAEs.

5. Distance from the HLQSO.
   This grouping is used to see if QSO radiation affects LAHs of surrounding LAEs. The HLQSO is so luminous that the entire field covered by the HSC could have higher ionizing radiation field than the cosmic average at $z \sim 3$ (Haardt & Madau, 2012) if radiation is reached, and additional ionization induced by the QSO will increase Lyα luminosity of LAEs in the field. Here, we use a projected distance from the QSO. This is equivalent to assume that all LAEs are at the same redshift as the QSO. Note, however, that the NB468 filter has an FWHM of $\Delta\lambda = 88$Å or $\Delta z = 0.075$, corresponding to 19 pMpc width when centered at $z = 2.84$. This brings uncertainty in a line-of-sight distance and also in a real (3D) distance.

We checked if there is any difference in the sample as a function of environments and distance from the HLQSO. Specifically, we checked the distributions of UV magnitude, Lyα luminosity, and Lyα equivalent width for each subsample. Figure 3.1 and Figure 3.2 are the summary of cumulative distribution functions. Note that a weird behavior of the purple curve in the lower-right panel of Figure 3.1 is likely to be artificial; as seen in Figure 2.2, EWs of LAEs not detected in g band are just lower limits. Faint low-EW LAEs are also incomplete due to criterion about g − NB468 (Equation 2.1), thus distorting the distribution. In the top-left and lower-left panels in Figure 3.2, the protocluster subsample (LAEs with $\delta > 2.5$) evidently stands out among others, while distance from the HLQSO seems not to make significant difference. These difference should be kept in mind when interpreting the result in Section 3.4.

3.3 Analyses

3.3.1 Image Stacking

Details of our observations and data reduction is presented in Section 2.2. This time, as we interested in diffuse and extended components, we changed a background mesh size from 64 pixels to 176 pixels (= 30 arcsec). Then the Lyα image is created in the same manner to eliminate non-emitters such as foreground stars and galaxies.

Continuum image is created at the same time, and a segmentation image of this continuum image is used for masking. A segmentation image is an output of SExtractor

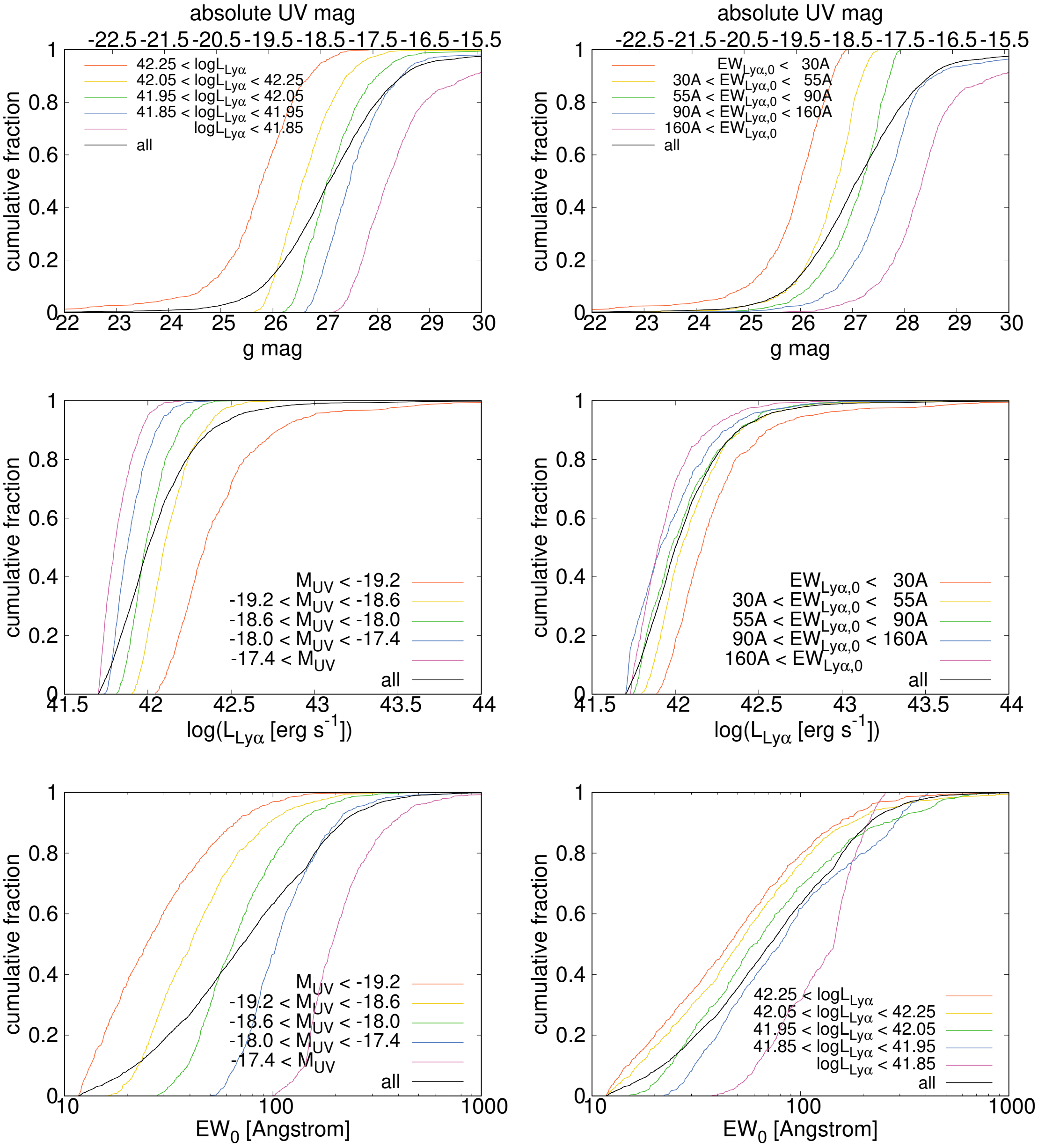

Figure 3.1: Cumulative distributions of UV magnitude, Lyα luminosity, and Lyα EW from top to bottom. Left, Middle, and Right columns respectively highlight differences between subsamples based on UV mag, $L_{\mathrm{Ly}\alpha}$, and $\mathrm{EW}_{0,\mathrm{Ly}\alpha}$.

and it specifies which pixel is detected as a source (if detected, that pixel has a non-zero integer value which corresponds to ID number in the output catalog). Then we created

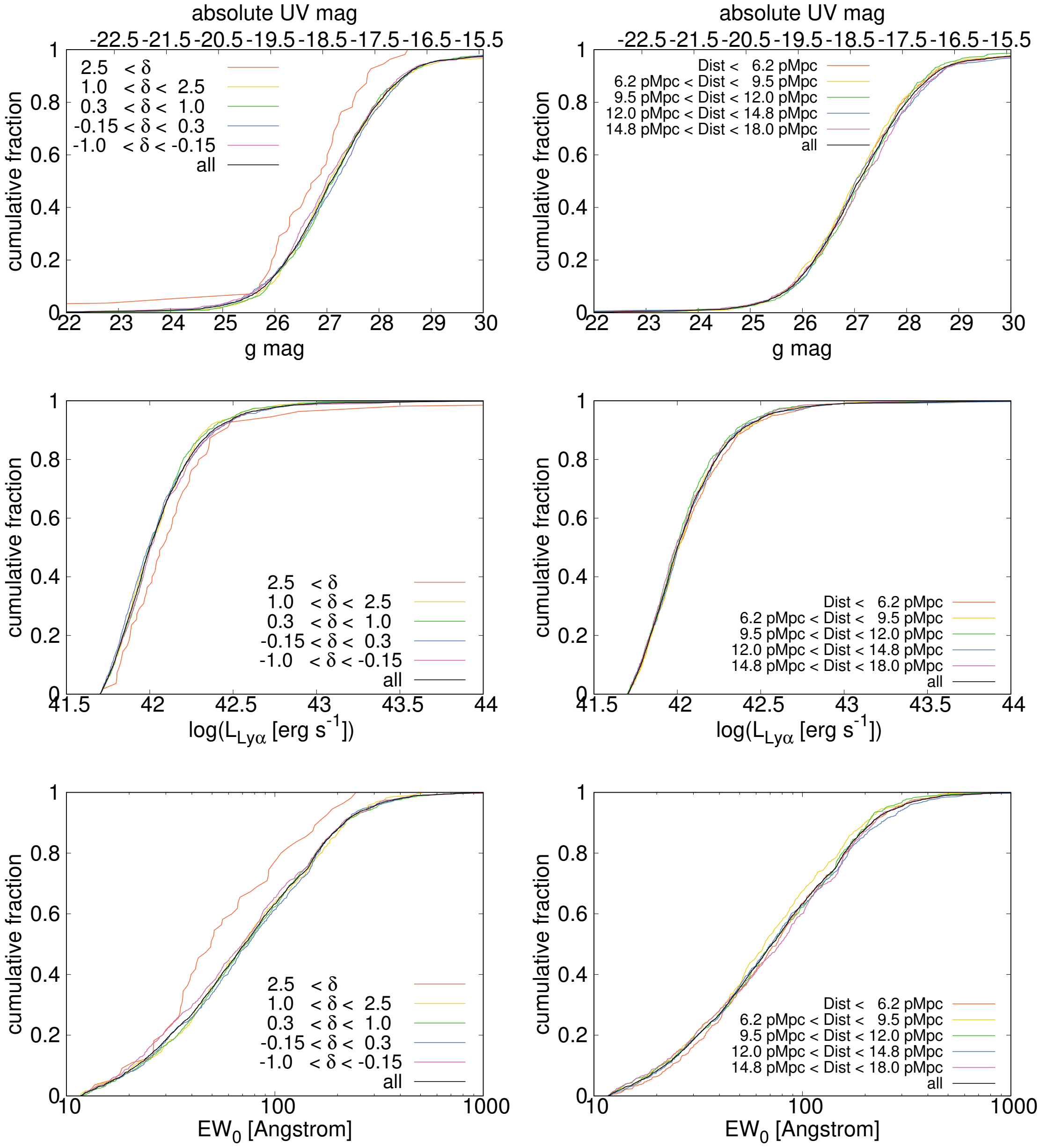

Figure 3.2: Cumulative distributions of UV magnitude, Lyα luminosity, and Lyα EW from top to bottom. Left (right) column highlights dependence on environment (distance from the HLQSO).

cutout Lyα images centered on each LAEs. The mask is applied to each cutout image. If the LAE at the center of cutout image is detected in the continuum image, masking

quantity	criteria	N
UV magnitude	$M_{\rm UV} < -19.2$	690
	$-19.2 < M_{\rm UV} < -18.6$	696
	$-18.6 < M_{\rm UV} < -18.0$	773
	$-18.0 < M_{\rm UV} < -17.4$	648
	$-17.4 < M_{\rm UV}$	683
Lyα luminosity	$42.25 < \log L_{\rm Ly\alpha}$	647
	$42.05 < \log L_{\rm Ly\alpha} < 42.25$	833
	$41.95 < \log L_{\rm Ly\alpha} < 42.05$	610
	$41.85 < \log L_{\rm Ly\alpha} < 41.95$	645
	$\log L_{\rm Ly\alpha} < 41.85$	755
Lyα equivalent width	$\rm EW_{0,Ly\alpha} < 30$Å	686
	30Å$< \rm EW_{0,Ly\alpha} < 55$Å	727
	55Å$< \rm EW_{0,Ly\alpha} < 90$Å	698
	90Å$< \rm EW_{0,Ly\alpha} < 160$Å	735
	160Å$< \rm EW_{0,Ly\alpha}$	644
Environment	$2.5 < \delta$	55
	$1.0 < \delta < 2.5$	433
	$0.3 < \delta < 1.0$	944
	$-0.15 < \delta < 0.3$	1076
	$-1.0 < \delta < -0.15$	982
Distance from the HLQSO	$d_{\rm Q} < 6.2$ pMpc	679
	6.2 pMpc $< d_{\rm Q} < 9.5$ pMpc	739
	9.5 pMpc $< d_{\rm Q} < 12.0$ pMpc	633
	12 pMpc $< d_{\rm Q} < 14.8$ pMpc	778
	14.8 pMpc $< d_{\rm Q} < 18.0$ pMpc	661

Table 3.2: Subsample used in our stacking analysis. N is the number of LAEs which satisfy the criteria described in the middle column.

for the object is turned off so as not to underestimate Lyα emission near the center. We show an example of the masked cutout Lyα image and continuum image in Figure 3.3. Stacking is executed using the IRAF task "imcombine" with median to further eliminate unrelated signals.

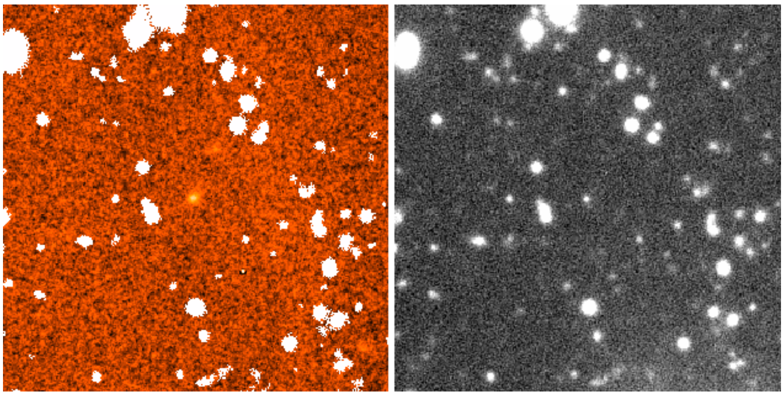

Figure 3.3: Example of cutout Lyα (Left) and continuum (Right) image. Objects detected in the continuum image is masked in the Lyα image (white pixels show masked region when stacking). This LAE is also detected in the continuum image, but mask for the LAE itself is switched off.

3.3.2 Uncertainties and Limitations

To estimate the noise level of stacked image, we created cutout image of the Lyα image centered on randomly selected points in the field. After applying the continuum mask, these "sky cutouts" are stacked in the same manner as LAEs. Number of sky cutouts used for stacking should be the same as the number of LAEs of each subsample. The noise level of an image created by stacking of N images is estimated by repeating this 1000 times and averaging each result. As shown in Figure 3.4, we confirmed that the noise level decreases almost as $\propto N^{-1/2}$. Thus, we decided to extrapolate this relation to estimate the noise level of stacked image with any N rather than to iterate 1000 times for every possible N in the right column of Table 3.2. The same method is used to estimate the noise level of the continuum image, which behaves almost $\propto N^{-1/2}$ as well. This contains the effect of large-scale flat-fielding errors discussed in Feldmeier et al. (2013).

At the same time, average values of the sum of the counts in each annulus are measured. Due to systematic errors, the average sky counts is not exactly equal to zero. To correct for this effect, we subtract average sky value when we derive the radial profile. Typical sky value of the Lyα image is $\sim -5 \times 10^{-21}$ erg s^{-1} cm^{-2} arcsec^{-2}.

Since the Lyα image is created by subtracting the g-band image from the NB image, any difference between PSFs of the images could make spurious patterns around

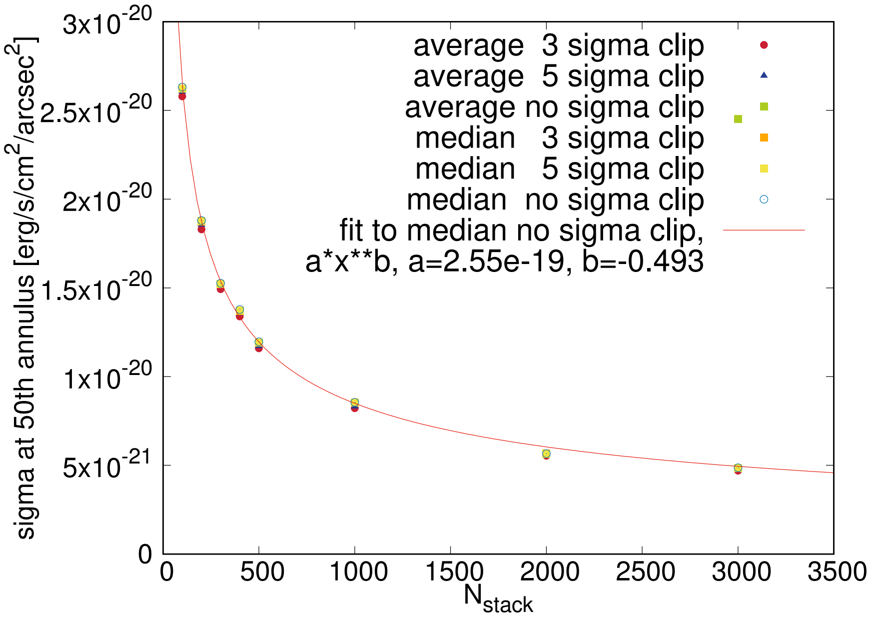

Figure 3.4: Estimating the sky noise level of the Lyα image. X-axis shows how many sky cutouts are stacked and y-axis shows estimated noise level evaluated in a specific annulus containing 1270 pixels. Different points indicate different stacking method (average VS. median, no sigma clipping VS. with 3(5)σ clipping), which are all well converged except for the case with average without sigma clipping. Red curve is a fitting function with a form $a \times N^b$ to the blue circles, which is consistent with inverse square root proportionality.

sources in the Lyα image. Even if PSF matching done in Section 2.2 can match the FWHM of stellar sources, it cannot completely match the exact shape of PSFs of two images. Moreover, the shape of PSF at large radius may introduce additional errors. To examine the detailed shapes of the PSF in the two images, we first select bright unsaturated sources from a source catalog using one of the SExtractor output CLASS_STAR, which is a parameter showing stellarity of sources. CLASS_STAR is 1 if an object is a point source and drops 0 if extended. Here we use following criteria: CLASS_STAR> 0.95 and $18 < g < 22$. In total, 3980 sources are stacked to determine the central part of the PSFs in the images[1]. To determine the much fainter outer part of

---

[1] Initially we divide this sample into two; one is sources distributed in the inner part of the field and the other is in the outer part. The profiles of the stacked image of the two subsamples are almost identical. Thus we conclude that variation of the PSF within the field is minor and ignore the effect in

the PSFs, we extracted stars with magnitude $13 < g_{\mathrm{SDSS}} < 15$ from the SDSS DR14 catalog (Abolfathi et al., 2018). After excluding stars with bright nearby companion and/or obviously extended sources when seen with our deep images, images of 113 bright stars are stacked. Point sources start to saturate in this magnitude range. Thus, the PSF of the brighter sources are connected at $r = 20$ pixels or 3.4 arcsec with that of fainter sources, following a method described in Infante-Sainz et al. (2019). Derived PSFs from 0.17 arcsec to 40 arcsec are shown in Figure 3.5. The PSF of the NB image is slightly smaller than that of the g band at $r =$ a few arcsec.

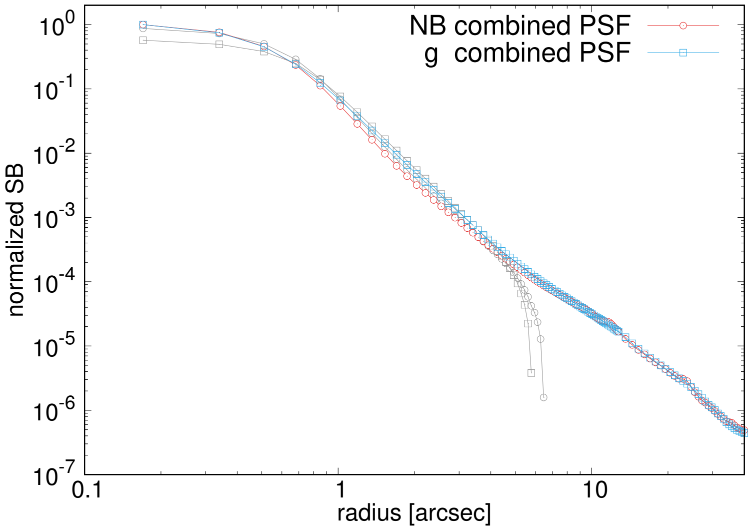

Figure 3.5: Normalized PSFs of the NB (red circles) and g (blue squares) band images. The inner and outer PSFs are connected at $r = 3.4$ arcsec (20 pixels). Gray curves are the extrapolated inner and outer PSFs beyond the junction radius.

To check if the slight difference of PSFs affects our LAH measurement, we created a stacked "non-LAE" image, following a method described in Momose et al. (2014). "Non-LAE" sources are defined as objects not selected as LAEs which have almost the same distribution in the object size VS NB468 magnitude plane as the real LAEs (Figure 3.6). Since the majority of LAEs are distributed in the range 0.75 arcsec < FWHM < 3.25 arcsec and 24 < NB468 < 26.5, we select non-LAE sources in this range. Any signal detected in the stacked Lyα image of non-LAEs can be used as an estimate not only for

---

the following analyses.

the PSF difference but also other unknown systematic effects such as errors associated with flat-fielding and sky subtraction.

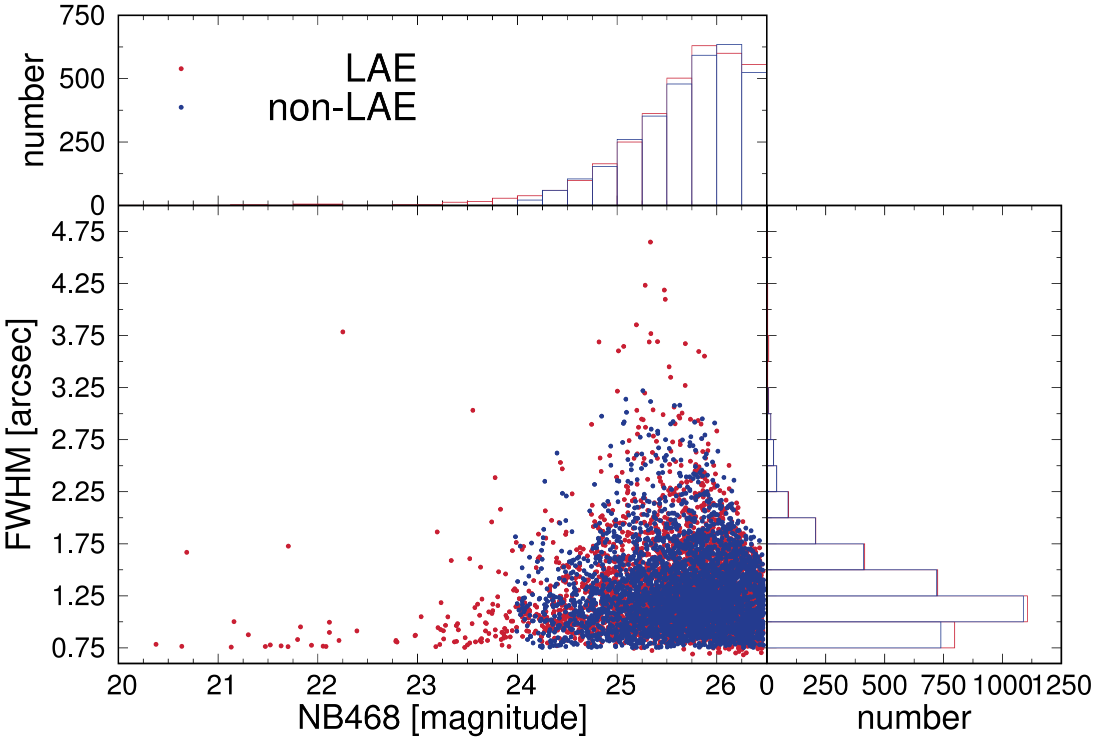

Figure 3.6: FWHM VS NB468 plot of LAE (red) and non-LAE (blue). Top and right panels show histgrams of NB468 and FWHM, respectively. Their distribution is almost identical.

3.4 Results

Figure 3.7 shows the stacked Lyα and continuum images of all LAEs and non-LAEs. The profiles of them are shown in Figure 3.8. The non-LAE has a negative ring-like structure around the center. This probably arises from the slight difference in PSFs of g band and NB images. Still, the absolute value of the non-LAE profile is about an order of magnitude smaller than that of LAEs in Figure 3.8. Beyond 2 arcsec, the profile of the non-LAE stack is almost consistent with the sky value and thus the effect of PSF

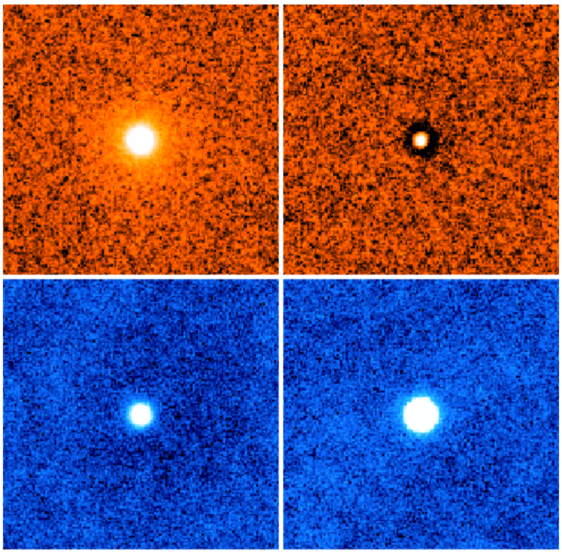

Figure 3.7: Stacked Lyα (top) and continuum (bottom) image of all LAEs (left) and non-LAEs (right).

difference is negligible. The large-scale PSF, which is shown with the gray curve in Figure 3.8, drops much more rapidly than the Lyα profile of LAEs. From the above arguments, we conclude that LAHs around LAEs at $z = 2.85$ are robustly detected and the effects of systematic errors cannot have a significant impact on the derived Lyα SB profiles.

To check if the mesh size for sky estimation matters or not, we derived a stacked Lyα profile of all LAEs with different sky mesh sizes than 30 arcsec. A larger mesh size enables us to probe possible large-scale emission around LAEs, at the same time increasing errors due to residual non-astrophysical signals (which stem from e.g. halos around bright stars). A smaller mesh size may lead to oversubtraction of real signal while reducing errors described above. To find a better compromise, we tested sky mesh sizes of 1 arcmin, 2 arcmin, and 11 arcsec (64 pixels, the default mesh size used in Chapter 2). 1σ errors and residual sky emissions to be subtracted are derived in the same way as described in Section 3.3.2. In Figure 3.9, we showed results of this test. The derived Lyα SB profiles are all consistent with the case for a mesh size of 30 arcsec within uncertainty. Also, no systematic trend is noticed with increasing mesh size in the slight offset seen in the outer part. This suggests the effect of oversubtraction of

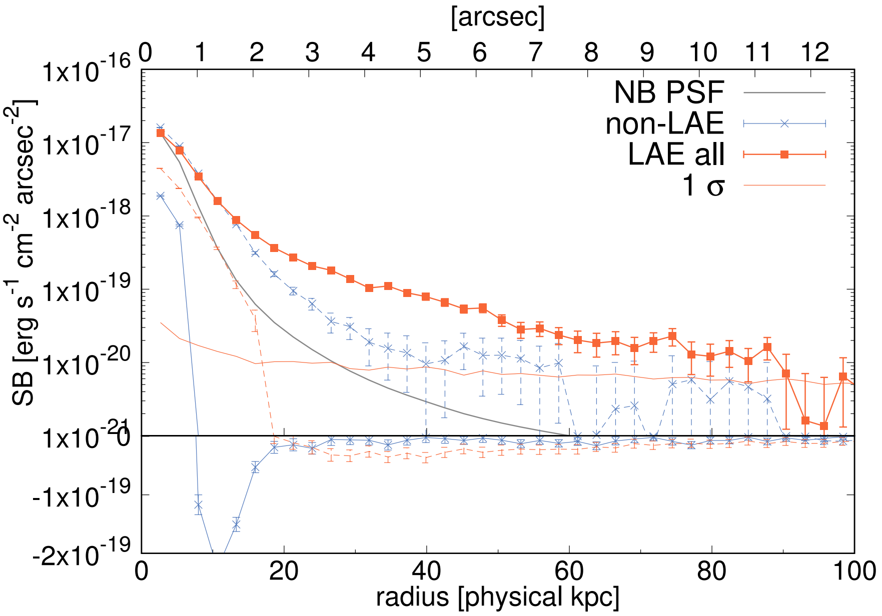

Figure 3.8: Radial SB profile of LAEs (red) and non-LAEs (blue) in the Lyα (solid curve) and continuum (dashed curve) images are shown. Red thin solid curve shows 1σ noise level. On the bottom side, SB profiles below 1×10^{-21} erg s^{-1} cm^{-2} arcsec^{-2} level are shown in linear scale. The normalized PSF of the NB image is shown with the gray curve.

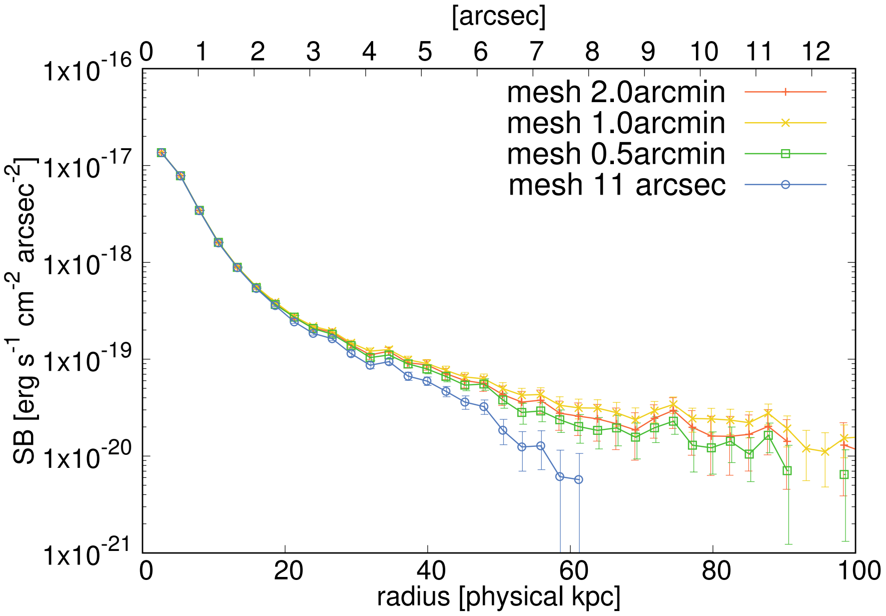

Figure 3.9: Radial Lyα SB profiles of all LAEs with different sky mesh size. Red, yellow, green, and blue curves respectively indicate profiles derived with sky mesh sizes of 2 arcmin, 1 arcmin, 0.5 arcmin, and 11 arcsec.

large-scale diffuse Lyα emission is minor. However, as the larger sky mesh sizes are utilized, residual artificial emission around bright stars in the Lyα images becomes clearer as well. On the other hand, a mesh size of 64 pixels = 11 arcsec = 85 pkpc clearly oversubtract sky emission. Considering that LAHs are detected out to several tens of pkpc, a mesh size of 85 pkpc, which is comparable to the extent of LAHs, should not be used. Thus, the use of 0.5 arcmin = 30 arcsec sky mesh is justified.

Next, we show the stacked Lyα and continuum images of all subsamples in Figure 3.10 and Figure 3.11. Derived profiles of stacked Lyα and continuum images are shown in Figure 3.12 and Figure 3.13. We detected LAHs, or Lyα emission more extended than UV (stellar) emission in all subsample. As expected, clear and systematic differences can be seen in bins of UV, $L_{\mathrm{Ly}\alpha}$, and $\mathrm{EW}_{0,\mathrm{Ly}\alpha}$ in a way that UV/Lyα-bright LAEs or low $\mathrm{EW}_{0,\mathrm{Ly}\alpha}$ LAEs have larger LAHs. On the other hand, the difference of profiles in Figure 3.13 is not obvious except for the protocluster subsample (those with $\delta > 2.5$). In the lower-left panel of Figure 3.13, curves seem to deviate with each other beyond 2 arcsec. To check if this is significant, we performed a test; we stacked Lyα images of 700 randomly selected LAEs from the whole ($N = 3490$) LAE sample and derived their Lyα SB profiles. We repeated this test 500 times and derived the 5th and 95th percentile of the SB distribution in each annulus. These are shown as a gray shaded region in Figure 3.13. The curves are almost within the shaded regions, suggesting that the difference is insignificant. There is no difference in UV SB profiles in both cases, again except for the protocluster subsample, which contains more UV bright galaxies as seen in Figure 3.2.

3.5 Discussion

First of all, we clearly detect LAHs for every subset of LAEs. Notably, even LAEs near voids have extended LAHs compared to continuum emission. Therefore non-detections reported in some previous works are probably due to the shallowness of their images (Feldmeier et al., 2013).

3.5.1 Dependence of the LAH Shapes on Galaxy Properties

To quantify the LAH shapes, previous works used a “halo scalelength” r_{h} (e.g., Steidel et al., 2011; Matsuda et al., 2012). This is derived by fitting a function with a form $S = C\exp(-r/r_{\mathrm{h}})$ to observed data. However, r_{h} varies a lot depending on how fitting is performed (e.g., the range of radius used in fitting, binning size, etc.). Indeed, most of the observed Lyα SB profiles are downwardly convex and thus r_{h} becomes larger when the outer boundary of the fitting range is larger. In some cases, profiles start to fluctuate beyond just ~ 30 pkpc which affects the measurement of r_{h}. Most of the previous studies fit from ~ 10 pkcp to ~ 40 pkpc, despite poorer sensitivity than our measurements, making direct comparison difficult.

Keeping the above argument in mind, we performed fitting to the observed data. Figure 3.14 compiles r_{h} for all subsamples. As expected, basically a wider fitting range results in larger r_{h}. The Lyα SB profile derived for the stack of all LAEs have relatively good S/N ratio and r_{h} can be reliably determined for the profile among others. Fitting to this profile yields $r_{\mathrm{h}} = 13.0$ pkpc (fit to 15 pkpc $< r <$ 40 pkcp) or $r_{\mathrm{h}} = 10.1$ pkpc (fit to 15 pkpc $< r <$ 30 pkpc), slightly larger than typical values derived in normal environments (r_{h} = 5-10 pkpc, e.g., Momose et al., 2014, who employed fitting range of 2 arcsec - 40 pkpc). The reason why we found systematically higher r_{h} may be the

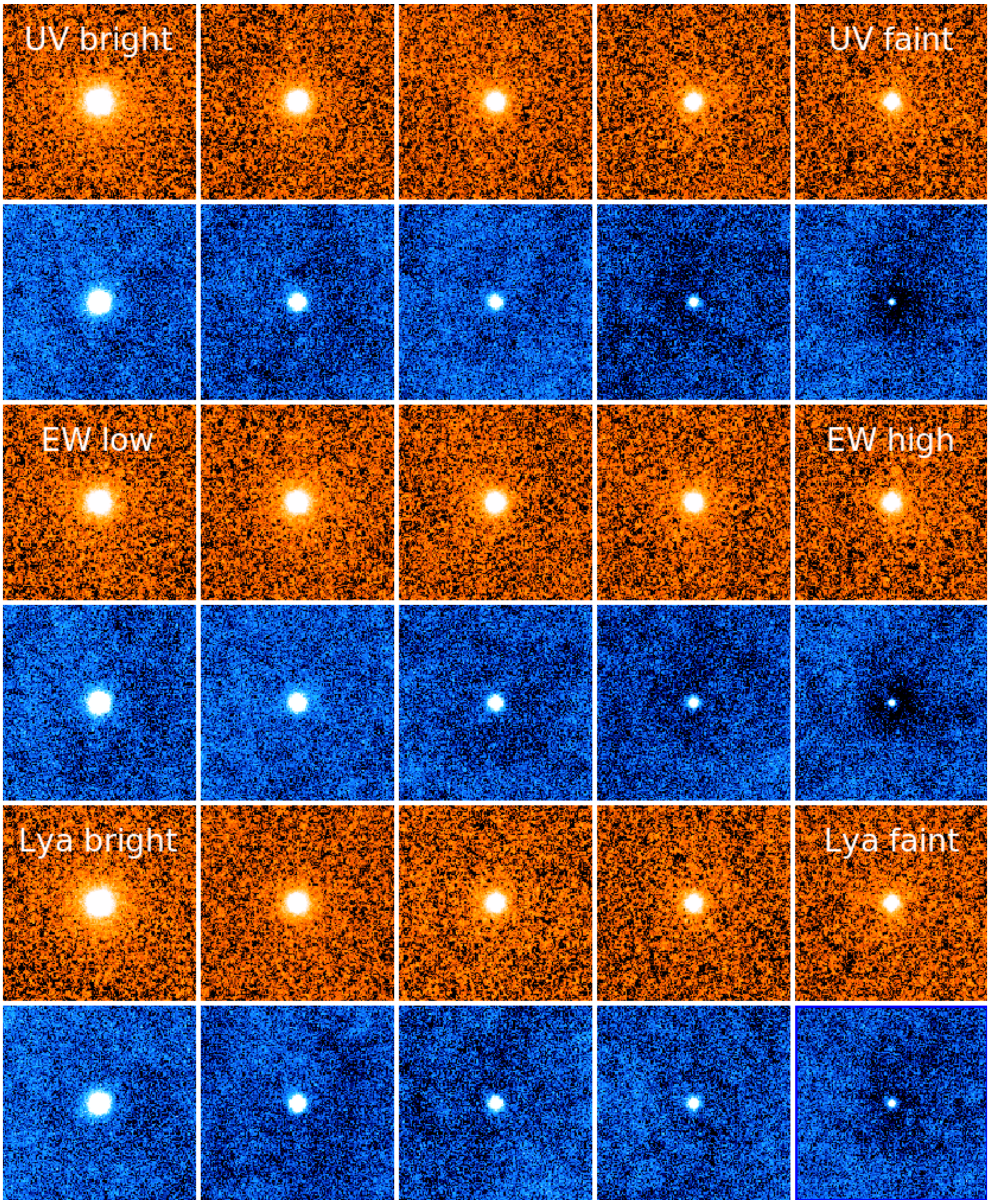

Figure 3.10: Stacked Lyα (odd row, orange) and continuum (even row, blue) images of different subsamples. From top to bottom, we show stacked images of UV magnitude, $L_{\rm Ly\alpha}$, $\rm EW_{0,Ly\alpha}$ subsamples. From left to right, median [UV, $L_{\rm Ly\alpha}$, $\rm EW_{0,Ly\alpha}$] of each subsample respectively become [fainter, fainter, larger]. The size of each image is 200 × 200 pkpc.

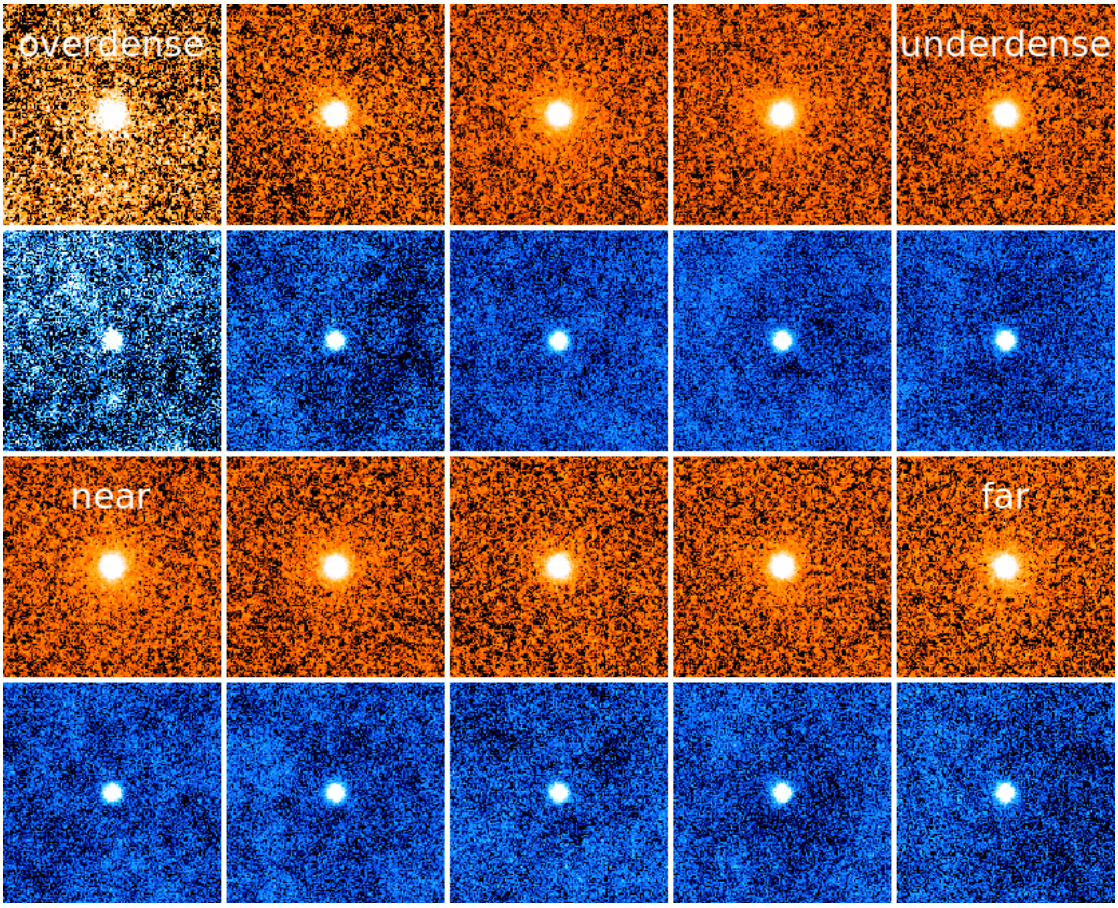

Figure 3.11: Same as Figure 3.10, but here we show stacked images of environment (top) and distance (bottom) subsamples. From left to right, median δ and distance from the HLQSO of each subsample become smaller and larger, respectively. The size of each image is 200 × 200 pkpc.

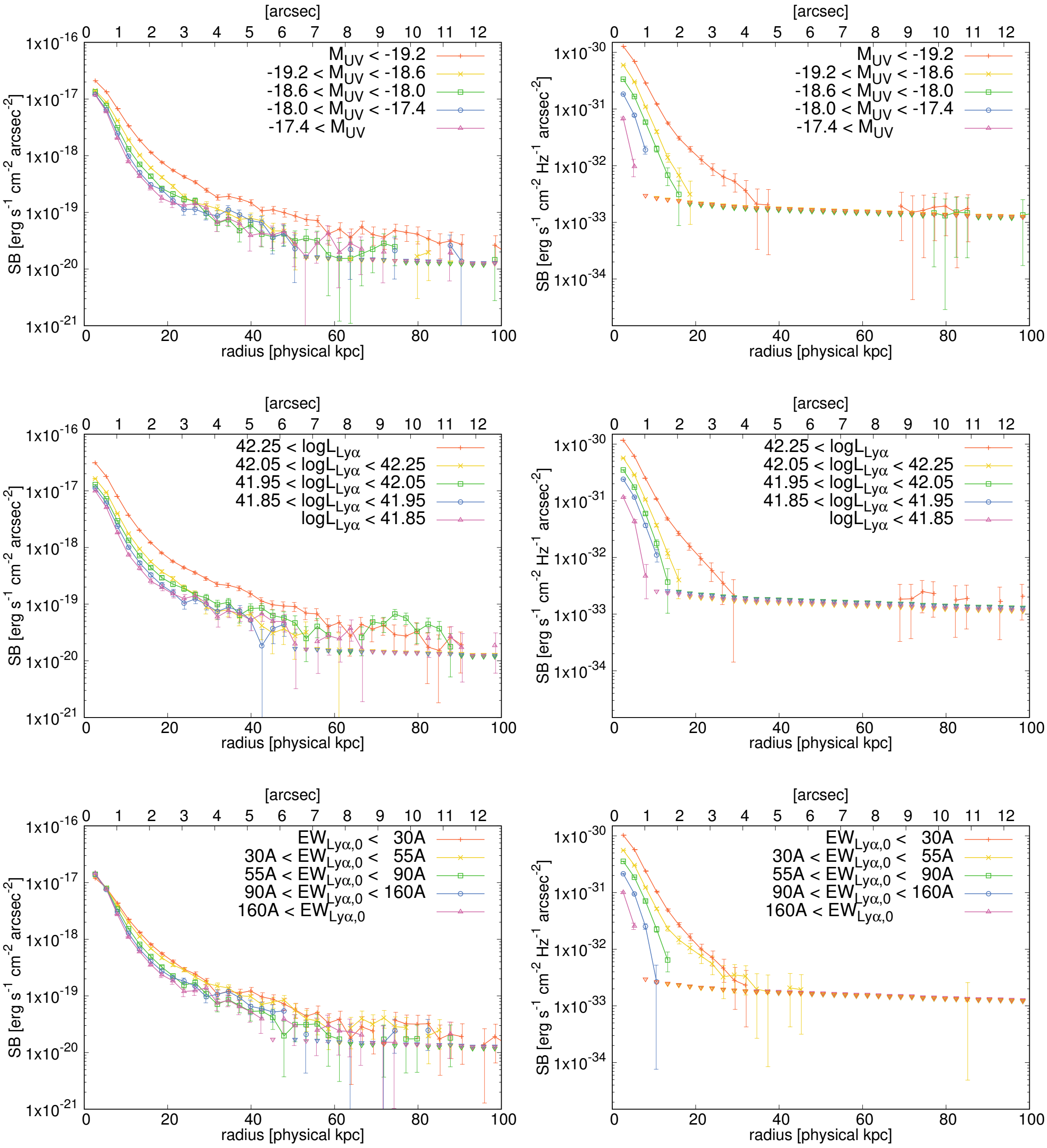

Figure 3.12: Lyα SB profiles (Left) and UV continuum SB profiles (Right) derived by stacking analysis. From top to bottom, the LAE sample is grouped by their UV magnitude, Lyα luminosity, and Lyα equivalent width in the way we specified in Table 3.2. The error bars are slightly shifted horizontally for display purpose. Downward triangles show 1σ error levels after residual sky subtraction.

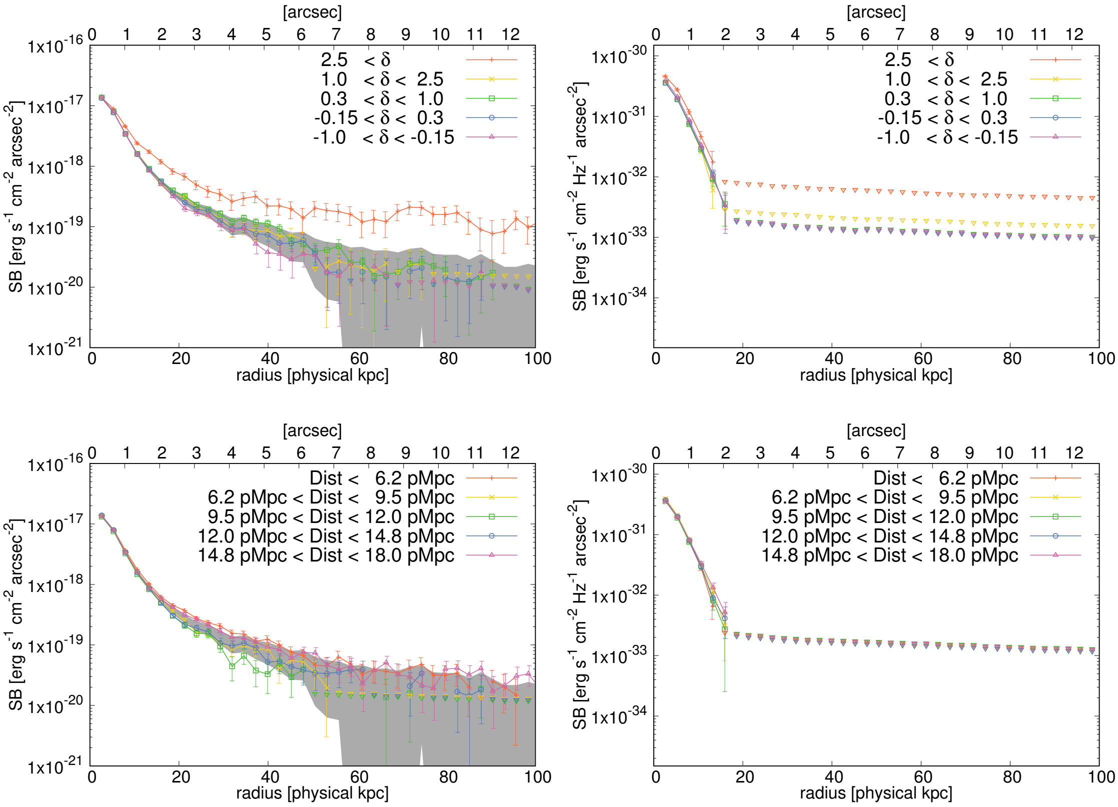

Figure 3.13: Same as Figure 3.12, but here the LAEs are grouped by their environments and distances from the HLQSO in the way we specified in Table 3.2. Gray shaded regions show 5th and 95th percentile of the Lyα SB distribution of stacked images created with randomly selected 700 LAEs.

better sensitivity of our data. The Lyα SB profiles start to flatten beyond 20 pkpc in Figure 3.12 and Figure 3.13. This trend cannot be captured with shallow data, thus leading to underestimation of r_h. We defer further discussion based on r_h for the reason discussed above. Instead, in Figure 3.15 we show Lyα SB profiles of LAEs normalized at the innermost radius, to facilitate comparison of their shapes. Even with our deep datasets, it is hard to investigate the behavior of LAHs beyond 30 pkpc because of statistical fluctuations and the sky noise. On the other hand, systematic trends within 30 pkpc can be clearly seen in the three panels. Consistent with Momose et al. (2016), UV-bright and low-EW LAEs tend to have more extended LAHs. Momose et al. (2016) also claimed that high-$L_{\mathrm{Ly}\alpha}$ LAEs have smaller LAHs, as opposed to our

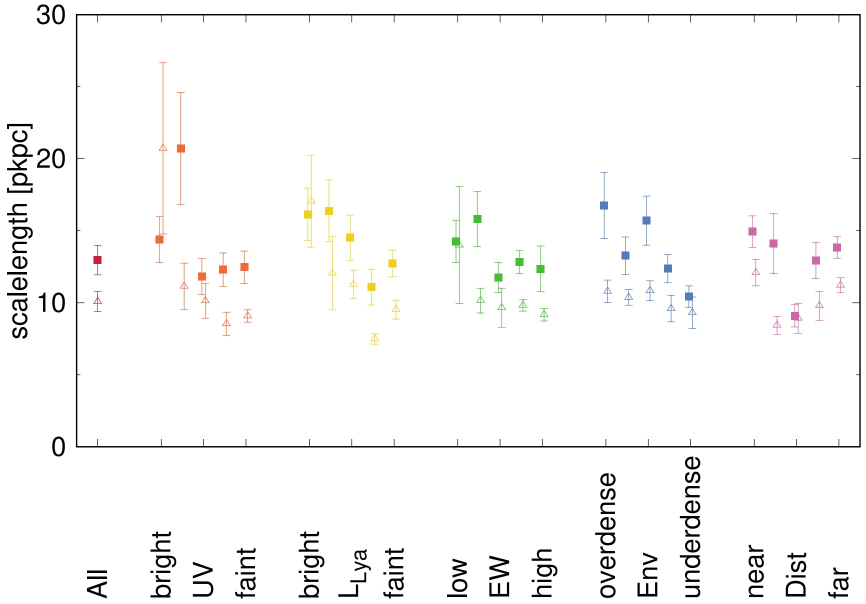

Figure 3.14: Halo scalelengths of various subsamples. Values shown with filled squares are obtained by fitting $15 < r < 40$ pkpc range, while those shown with open triangles are obtained by fitting $15 < r < 30$ pkpc range.

observations. However, considering that the difference observed in our data is minor and the curvature seen at $r < 20$ pkpc, their claim could be correct. This should be confirmed with much deeper datasets in the future.

High EW LAEs are very efficient in producing Lyα photons. Thus, if they have the same amount of scattering media around them compared to those of low-EW LAEs, their LAHs should become larger. Our observations suggest this is not the case and high-EW LAEs have smaller gas envelope. This is consistent with the trend of higher EW LAEs having fainter UV luminosity and thus having lower halo mass through the $M_{\rm UV} - M_{\rm halo}$ relation (Harikane et al., 2018). Or, if they ionize much of the gas around them with very young stellar population, the amount of scattering HI will decrease. This in turn makes Hα halos via fluorescence which are not developed in the case of scattering by HI. Observations of Hα emission from $z = 2.85$ is however very difficult with ground-based telescope due to heavy atmospheric absorption. Future space-based facilities can open up a new pathway to study LAHs and the CGM in this redshift and beyond.

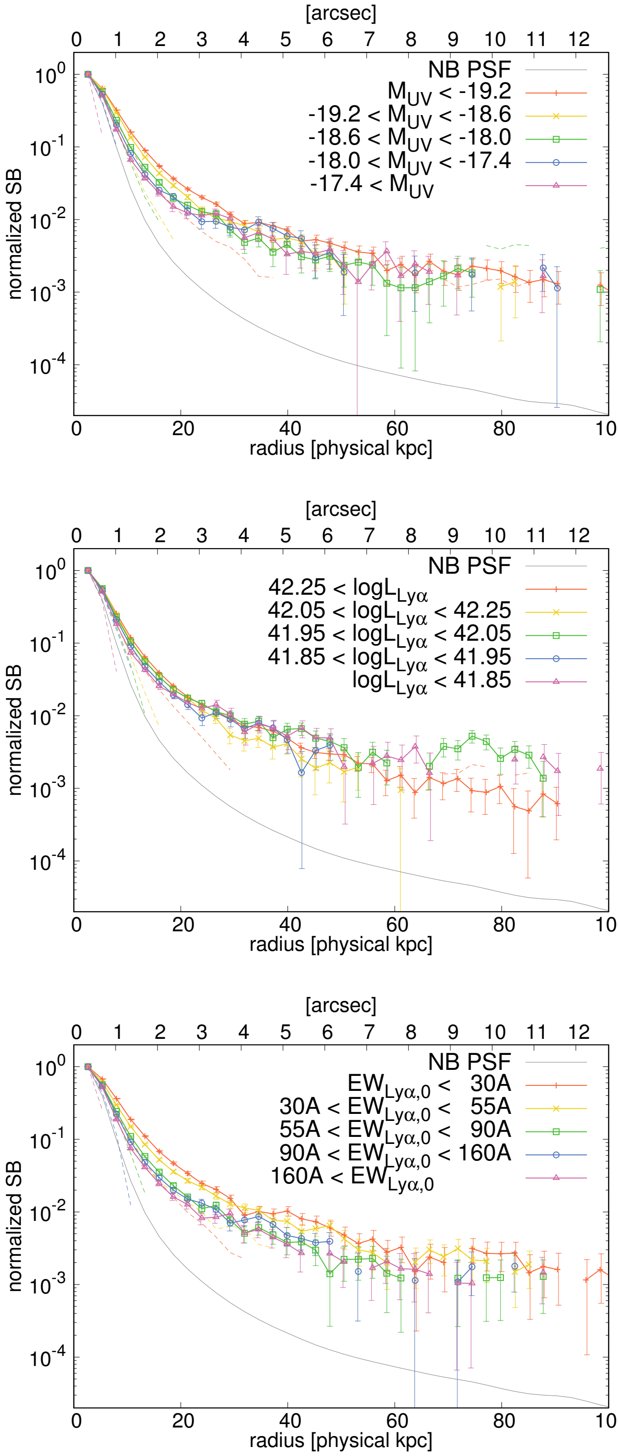

Figure 3.15: Normalized Lyα SB profiles. From top to bottom, the LAE sample is grouped by their UV magnitude, Lyα luminosity, and Lyα equivalent width in the way we specified in Table 3.2. Dashed curves are normalized UV continuum SB profiles for reference.

In Figure 3.13 we studied the dependence of LAHs on environment and distance from the HLQSO seems minor except for the protocluster LAEs. Indeed, $-0.15 < \delta < 0.3$, $0.3 < \delta < 1.0$, and $1.0 < \delta < 2.5$ subsamples are all within the gray region and overlap with each other within 1σ for almost all radius. If LAHs trace gas distribution of the CGM, this indicates that the large-scale environment does not have a large impact on the CGM shape and it is solely determined by individual halo mass or internal process such as outflow driven by feedback. At much higher redshift of $z > 6$, circumstantial evidence of outflow redistributing the CGM gas is indeed obtained; Fujimoto et al. (2019) found 10-pkpc scale diffuse [CII] halos as a result of a (visibility-based) stacking analysis of ALMA data of $z = 5$–7 star-forming galaxies. On the other hand, the $\delta < -0.15$ sample systematically deviate below the gray region at $r > 20$ pkpc. Although deeper observations are needed, this imply a possible deficit of gas in void galaxies.

As for the distance from the HLQSO (r_{Q}), $r_{\mathrm{Q}} < 6.2$ pMpc and 14.8 pMpc $< r_{\mathrm{Q}} < 18.0$ pMpc subsample deviate from the rest three (consistent within 1σ). Although $r_{\mathrm{Q}} < 6.2$ subsample contains all the protocluster sample which have large LAHs, it only amounts to 55 comparing the total number of 679 in the subsample and the effect should be minor. The only explanation we can think of is variable QSO activity in the past. If the HLQSO is active about ~ 50 Myr and ~ 20 Myr ago, the ionizing photons emitted then illuminate 15 pMpc and 6 pMpc away from the QSO. These photons ionize the envelopes of the LAEs and boost their Lyα luminosity, explaining the observed behavior. However, at 15 pMpc away, the ionizing radiation field strength due to the QSO will be just about 2 times the UVB at this redshift (e.g., Haardt & Madau, 2012) even assuming the very high luminosity observed today. This may not be enough to explain the observed level of boost (Umehata et al., 2019).

3.5.2 Origin of the Large LAH of Protocluster LAEs

We showed that dependence of LAHs on environments is not large where $\delta < 2.5$. On the other hand, at the protocluster ($\delta > 2.5$) the LAH shows elevated flux out to > 100 kpc. Enlarging the size of cutout images, we confirmed that flux higher than $> 1\sigma$ level continues out to ~ 500 pkpc. In this section, we investigate the cause of this emission in $\delta > 2.5$ subsample.

Recalling that the protocluster galaxies tend to have higher M_{UV}, $L_{\mathrm{Ly}\alpha}$ and low

EW in Figure 3.2 and that such galaxies have larger LAHs in Figure 3.12, the extent of LAHs of protocluster LAEs can be explained by just an overabundance of bright galaxies. We tested this scenario using the stacked Lyα images. We embedded stacked Lyα images in a blank image, mimicing the observed spatial distribution of LAEs and scaled by a certain factor to match observed UV magnitude, using IRAF task MKOBJECTS. We used the stacked Lyα image of appropriate M_{UV} subgroup when embedding LAE with a certain M_{UV}. For example, we embedded the stacked Lyα image of $-19.2 < M_{UV} < -18.6$ subgroup at the location of LAEs with $-19.2 < M_{UV} < -18.6$. At the core of the protocluster, LAEs are densely distributed and emission from nearby LAEs leads to overestimation of the SB profile. This test can simultaneously evaluate the effect of overlapping of halos. The result of the simulation is shown in Figure 3.16. Stacking the simulated LAEs in the same manner as the real LAEs with $\delta > 2.5$, we got an SB profile shown as the black line with open symbols in Figure 3.17. The observed large LAH is not at all reproduced. Two gray curves above and below the black curve are obtained by further dividing the simulated LAE sample into two. The one group is located within $\sim$ 400 pkpc from the HLQSO. This nearer group (see also Figure 3.18 for visualization of the distribution of the LAEs in the two samples) should be more severely affected by overlapping. However, this is still not enough to explain the observed profile of the $\delta > 2.5$ subsample. These arguments indicate that overlapping and overabundance of UV bright galaxies in the protocluster core cannot fully explain the observed large SB profile of the $\delta > 2.5$ subsample.

In Chapter 2, we see that there is an Mpc-scale diffuse Lyα emitting structure around the HLQSO. These ambient diffuse emission may cause such extended emission, especially at the compact central region of the protocluster. We further divide protocluster LAEs into a “near-core” group (red circled LAEs in Figure 3.18) and the rest (green circled LAEs), and then stacked them separately. In Figure 3.19, the near-core sample clearly shows excess emission which does not decrease toward the edge above the red curve, while the other stack shows just a mild bump around $\sim$ 15 kpc. The high level of Lyα SB continues out to $\sim$ 500 pkpc from the center. This suggests diffuse emission around $\sim$ 500 pkpc from the core of the protocluster and HLQSO indeed contributes to the extended emission. Although the “far” LAE sample shows a bump at $\sim$ 15 pkpc, there is no evidence about larger LAHs compared to other environment subsamples beyond 20 pkpc, despite they reside in an outskirt of the protocluster.

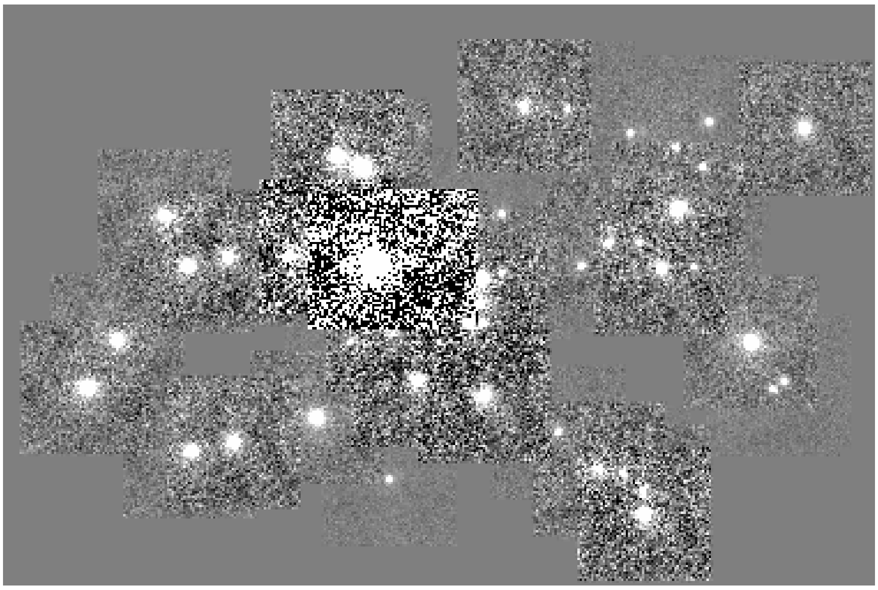

Figure 3.16: Simulated Lyα image of the protocluster core. See and compare with Figure 3.18.

3.5.3 Comparison with Previous Observational Studies

Xue et al. (2017) found no evidence for environmental dependence as a result of NB surveys for two protoclusters at $z = 3.78$ and $z = 2.66$. We caution that their survey are an order of magnitude shallower than our study. They used the Mayall 4m telescope for $z = 3.78$ data and the Subaru telescope for $z = 2.66$ data but used intermediate band filter (IA445 on Suprime-Cam, $\Delta\lambda = 201$Å) as shown in Table 3.1. In addition, the number of LAEs used to examine environmental dependence is at most 139 (for an intermediate density sample). Thus r_{h} derived through fitting to such data would not be appropriate to compare with our data. Moreover, their criteria to select LAEs only pick up high EW LAEs with $\mathrm{EW}_{0,\mathrm{Ly}\alpha} > 50$ in the $z = 2.66$ protocluster field. Our study suggest this could have a bias against large LAHs (Figure 3.12 and Figure 3.15). On the other hand, Steidel et al. (2011) reported that LBGs in three protoclusters, namely HS1700 protocluster at $z = 2.30$, HS1549 protocluster at $z = 2.85$ (which is also the target for this study), and the SSA22 protocluster at $z = 3.09$, have very large LAHs with a derived halo scalelength of $r_{\mathrm{h}} = 25.2$ pkpc. Matsuda et al. (2012) studied

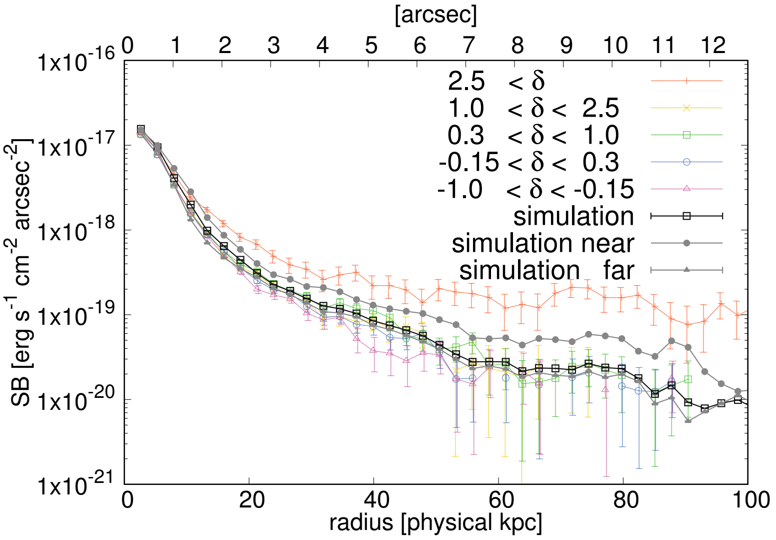

Figure 3.17: Stacked Lyα SB profile of the simulated protocluster LAEs (black curve with open symbol). Our simulation fails to reproduce the extent of observed profile. The gray curves above and below the black curve are obtained by further dividing simulated LAEs into two groups, a near-QSO LAEs and the rest. Simulated near-QSO LAEs have more nearby neighbors, but this effect cannot explain the observed SB profile of the $\delta > 2.5$ subsample.

environmental dependence of LAHs using NB images for the SSA22 protocluster and other blank field, finding that $r_{\rm h}$ becomes larger from normal density ($r_{\rm h} \sim 10$ pkpc) to the density peak of SSA22 ($r_{\rm h} = 29$ pkpc). Recently, Umehata et al. (2019) reported the central part of SSA22 is filled with diffuse Lyα emission. Combining this result with the fact that almost all the LAEs with $\delta > 2.5$ used in Matsuda et al. (2012) reside in the core of SSA22, the large LAHs reported in Matsuda et al. (2012) would be attributable to the diffuse emission, fully consistent with our finding in the core of HS1549. Moreover, the other field studied in Steidel et al. (2011), namely HS1700, also has a hint of such diffuse emission (Erb et al., 2011). Thus, possible dependence of LAHs on large-scale environments reported to date could be due to Lyα emission from the IGM rather than the CGM of member galaxies. Such a large value for $r_{\rm h}$ that exceeds 20 pkpc is rarely reported in blank fields and likely a phenomenon unique to protoclusters at cosmic noon, the peak epoch of cold gas accretion rate (Kereš et al., 2009).

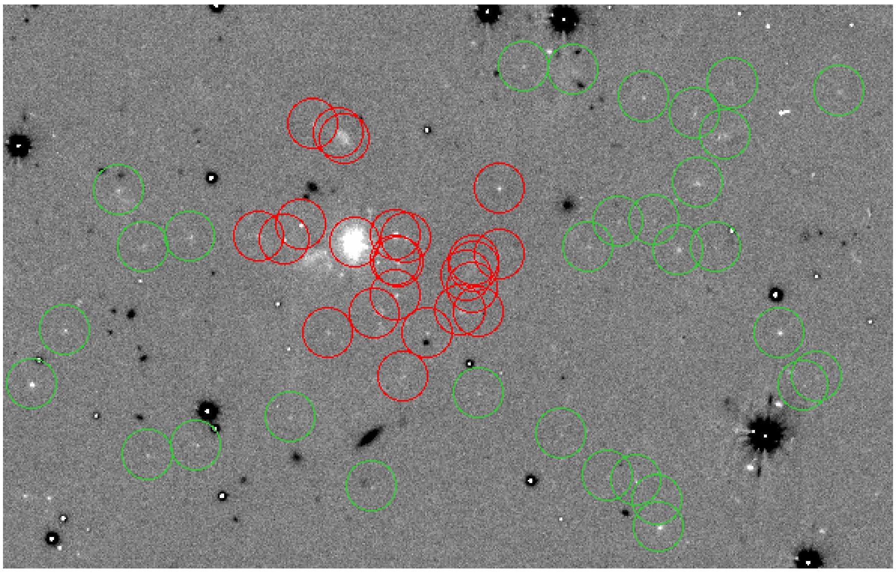

Figure 3.18: LAEs in the protocluster are further divided into two; one group contains LAEs near the HLQSO (red circles), the other contains the rest (green circles).

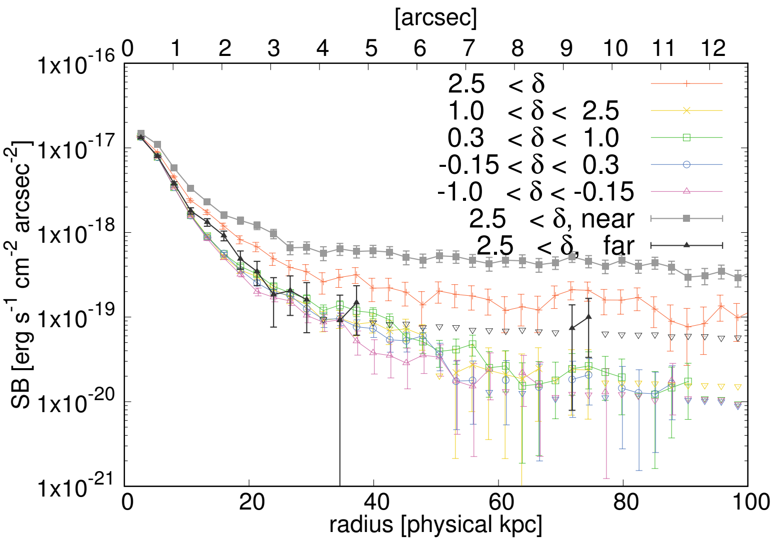

Figure 3.19: Stacked Lyα SB profiles of "near-core" sample and the other group of LAEs with $\delta > 2.5$, with SB profiles of LAEs in other environments. LAEs near the QSO clearly shows exceptionally large LAHs.

3.5.4 Comparison with LAHs in Numerical Simulations

To study the origin of LAHs, we compare out results with the numerical simulation by Lake et al. (2015). They performed radiative transfer modeling of 9 LAEs at $z = 3.1$ in a high resolution hydrodynamical cosmological simulation based on the adaptive mesh refinement Eulerian hydrodynamic code Enzo, as descried in Cen (2012). Their $21 \times 24 \times 20h^{-3}$ Mpc^3 simulation box contains galaxy cluster at $z = 0$ and chosen from a low-resolution simulation with a box size of $120h^{-1}$ Mpc. Importantly, their simulation includes the UV background and the self-shielding. The dark matter particle mass is $1.3 \times 10^7 h^{-1} M_\odot$ and the spatial resolution is better than $111h^{-1}$ physical pc. They chose 9 star-forming galaxies with halo masses $10^{11.5} M_\odot$ having mean stellar mass of $\sim 3 \times 10^{10} M_\odot$. Our $M_{\rm UV} < -19.2$ subsample should match the halo mass according to semi-analytic modeling of Garel et al. (2015); halo masses of $-18.3 > M_{\rm UV} > -20.8$ LBGs are estimated to be $\sim 10^{11.4} M_\odot$. In the simulation, Lyα photons are produced by star formation and gravitational cooling. Produced Lyα photons are then scattered until escaping toward the observer's direction. Dust extinction in the interstellar medium and the absorption in the IGM are also modeled.

In Figure 3.20, cutout Lyα and UV continuum images of 9 galaxies are shown (Figure 2 and 7 of Lake et al., 2015). We compare the resultant profiles with our observations in Figure 3.21. Their profiles are corrected for slight redshift difference by multiplying $(1 + z_{\rm L15})^4/(1 + z_{\rm HS1549})^4$. The thick black line is the average of 9 galaxies. Simulated galaxies tend to have larger LAHs and the profile is more extended than those of our $\delta > 2.5$ subsample and $M_{\rm UV} < -19.2$ subsample. It seems that the average profile is largely affected by three galaxies, namely, galaxy ID G85, G184, and G1327. Thus we also draw an average profile of 6 other galaxies with the thin black line (average'). This curve agrees well with our Lyα SB profile created with all the LAEs (median $M_{\rm UV} = -18.3$) in the field at $r < 40$ pkpc.

The reason why simulated galaxies G85 (top right), G184 (bottom left), and G1327 (bottom right) have such extended profiles are evident in the right panel of Figure 3.20. They all have bright companion galaxies within a few tens of pkpc. For example, G184 has a companion at ~ 30 pkpc in the UV continuum image, and we can see a corresponding bump around ~ 30 pkpc in its SB profile. Some show even upturn of SB

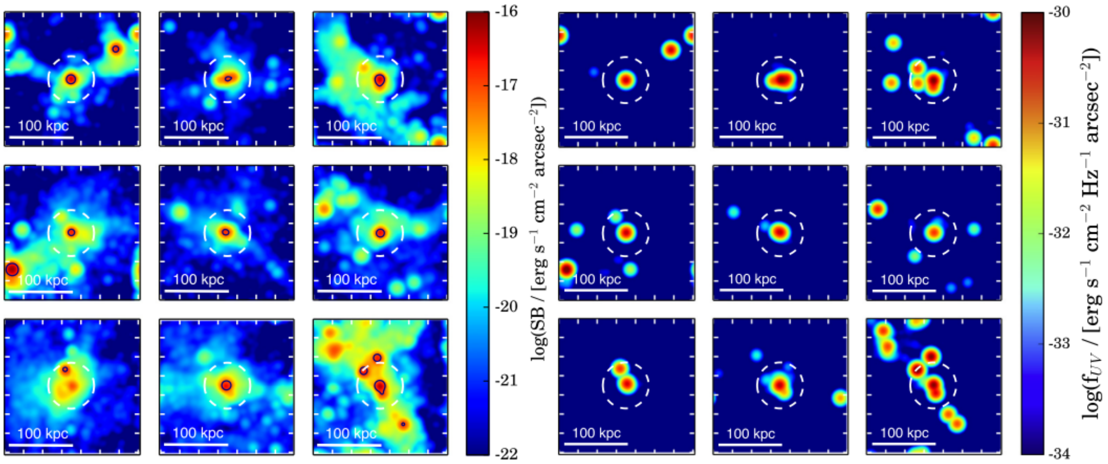

Figure 3.20: Lyα (left) and UV continuum (right) images of simulated galaxies, taken from Figure 2 and Figure 7 in Lake et al. (2015). White dashed circles denote 40 pkpc from the halo center. Black contour in the Lyα image shows an SB level of 10^{-17} erg s^{-1} cm^{-2} arcsec^{-2}, roughly equals to typical SB limit of individual LAE detection in surveys in the literature (e.g., Ouchi et al., 2008). Galaxy ID of each panel is, from top left to bottom right, G62, G76, G85, G87, G97, G131, G184, G346, and G1327.

beyond 60 pkpc (G62, G76, G87). This arises from the companion at > 80 pkpc [2]. To see if such bumps are reproduced in our data, we construct a new subsample which has LAEs with companion within 40 pkpc. We exclude LABs and LAEs with more than 1 companion from the subsample for simplification, resulting in 70 pairs of LAEs. Using the location of one of the LAEs among the pair as a center of image, stacking is performed. The result is plotted in the Figure 3.21. Similar to galaxies in the simulation with companions, a bump at $\sim$ 40 pkpc is clearly appeared. In this case, UV profiles are extended too, as opposed to most of the cases in Figure 3.12 and Figure 3.13. In the simulation, the averaged UV continuum profile also show very large halo out to > 80 pkpc (see Figure 8 of Lake et al. 2015).

From above arguments, the cause of high Lyα SB in the simulation is probably the overabundance of companion galaxies, which are rare in our observed LAE sample. Thus we conclude that the 9 galaxies selected in the simulation would not be representative of star-forming galaxies at $z \sim 3$. Since the simulation box is centered at

---

[2] In Figure 3.20, there is no companion around G76 (top middle). However, this is just a projection effect and there actually are companions behind G76 in a simulated galaxy catalog.

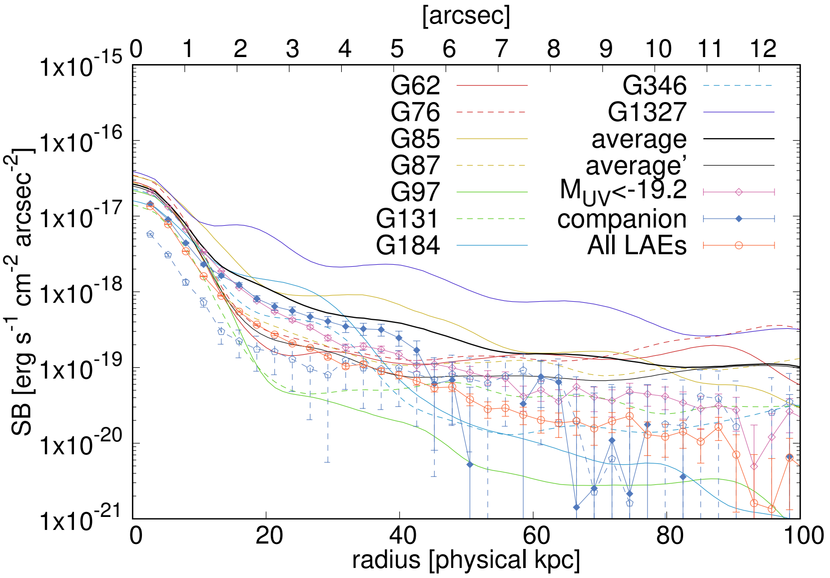

Figure 3.21: Lyα (left) SB profiles of galaxies in the Lake et al. (2015) simulation along with our results. The UV profile of companion subsample is shown with blue dashed line with error bars.

the galaxy cluster at $z = 0$, some over-representation of overdense regions is possible. Also, a stacking analysis can only produce the “averaged” shapes of stacked LAEs. As already evident in Figure 3.21, SB profiles in the simulation have very large scatter. They are computed by viewing them from many different direction (and thus signal from the companion or ambient knots are preserved). To directly compare with the observed profile, radiative transfer calculations of orders of magnitude more simulated galaxy are needed to derive the averaged SB profile.

We are able to capture the “flattening” of the Lyα SB profiles beyond 20 pkpc. This is roughly reproduced in the simulation and they claimed that this component cannot be explained by scattered Lyα photon emitted by the central galaxy alone and the contribution from “knots” and “background” is necessary. “Knots” are defined as high emissivity region other than the 9 galaxies seen in Figure 3.20. “Background” are the regions that are neither the central galaxies nor knots. In the simulation, the origin of each Lyα photon is recorded (either star formation or gravitational cooling). Their results show the contribution from gravitational cooling in the knots and background regions can be nearly ~ 50 %. Thus, the flattening regions of LAHs are explained by both the star formation and cooling radiation in matter clustered around galaxies. The significant contribution from the clustered sources is also supported by Zheng et al. (2011) at $z \sim 6$. Returning to our observations, we see higher level of emission in UV bright subsample than UV faint subsample in flattening region, while in the bins of environment only the protocluster sample shows deviation from others. Assuming that UV bright galaxies have massive dark matter halos and thus stronger clustering, UV bright galaxies should have more matter which produce Lyα in the flattening regions, consistent with the observed trend. At the same time, the weak environmental difference out of protoclusters may suggest that the clustering strength is solely determined by halo masses and not strongly depends on environment, or galaxy assembly bias is weak (Croton et al., 2007). Cooling radiation in the simulation is, however, difficult to handle because of exponential dependence on temperature (e.g., Faucher-Giguère et al., 2010). More accurate modeling of self-shielding against the UVB is needed to accurately predict the contribution of gravitational cooling radiation.

4

Conclusions and Future Prospects

In this Chapter, we summarize the key results obtained in Chapter 2 and Chapter 3, and wrap up what is learned from those results as a whole in Section 4.1. Discussions based on both Chapters are briefly presented in Section 4.2. In the end, we show how this study is extended in the future in Section 4.3.

4.1 Highlights of Previous Chapters

In this thesis, we investigated diffuse Lyα emission both from the IGM and the CGM, fully utilizing the NB468 and g band images obtained with Hyper Suprime-Cam on the Subaru Telescope. The original aims of this project suggested in Section 1.6 is: **(1)** to detect the IGM in emission to test the validity of the cold-mode accretion scenario, and **(2)** to determine if LAHs depend on environment they reside. These main goals are respectively discussed in Chapter 2 and Chapter 3 along with other sub-topics. In the following, we highlight the results especially relevant to the two aims.

4.1.1 Detection of the candidate of the cosmic web filament

In Chapter 2, we present a $>$ 100 cMpc-scale large-scale distributions of LAEs and LABs. Targeting at the protocluster, we are able to probe diverse environments down to void-like regions with only one pointing. Thanks to wide-field observations, the large-scale structure extending from the HS1549 protocluster is captured for the first time and we found that the protocluster marks the "node" of the large-scale filamentary structure. Such an environment is the place where simulations predict a huge amount of cold gas can accrete (Dekel et al., 2009). We indeed identified a variety of Lyα nebulae near the central part of the protocluster centered on the HLQSO. What especially stand out in this field are the significant overdensity of LABs, their apparent alignment with that of the large-scale structure, and the existence of a "filament" (Figure 2.9). In Section 2.4.2, we discuss the possibility of the filament being a dense part of the cosmic web. We think the discussion is reasonable and thus our aim is partially achieved. Very important next step is to follow-up with spectroscopy for definitive evidence. This will be further tested with planned observations with Keck/KCWI. We describe about this observation in Section 4.3.1.

4.1.2 Dependence of LAHs on Environments

In Chapter 3 we showed the results of the stacking analyses to probe LAHs of LAEs across environments. The depth and wide field coverage of our data enables us to argue the dependence of LAH shapes on various galaxy properties, especially on Mpc-scale environments with unprecedented depth and sample size at $z \sim 3$. We succeeded to detect more extended Lyα emission compared to UV continuum emission in all defined subsamples (Figure 3.12 and Figure 3.13). Surprisingly, we found that shapes of LAHs of LAEs in different environment do not show significant difference, except for those in the protocluster (the upper left panel Figure 3.13) where the Lyα SB profile of their stack does show significant offset from others. Combining our results including simulations described in Section 3.5.2 and those in literature, we conclude that dependence of LAH shapes of LAEs on large-scale environments is evident only in protoclusters and the dependence (including results reported in the previous works) could be due to diffuse emission around the cores of forming protoclusters in cosmic noon, where cold gas accretion rate should be high (Kereš et al., 2009). Thus, our aim

(2) is achieved, providing a significant step toward resolving the controversy in the literature.

4.2 Discussion

4.2.1 Relation between LABs and LAEs

While LABs evidently prefer denser environments (Figure 2.7 and Figure 2.8), LAHs of LAEs show difference only in the protocluster. This can be explained if the origin of the extent of the two classes is different. In Section 3.5.4, we argued that LAHs of LAEs are likely to be produced by scattering of Lyα photon from star formation and possibly gravitational cooling, through comparison with Lake et al. (2015). On the other hand, LABs could have much variable physical origins for their extent. As explained in Section 1.5, there are number of theoretical models which can reproduce observed extent and Lyα luminosity of LABs. Indeed, we can see a variety of morphology in the Lyα images of LABs shown in Figure 2.4 to Figure 2.6. LABs would be different class of object than typical ($L_{\mathrm{Ly}\alpha} \lesssim 10^{42}$ erg s^{-1}) LAEs, and their triggering mechanism should be related with dense environments to be consistent with the observed trend — probably galaxy mergers. To further reveal the origin of the variety of LABs, multi-wavelength observations are definitely required. We present ongoing observations of the protocluster core with ALMA in Section 4.3.2.

4.2.2 Benefits and Caveats of Our Project

As is already demonstrated, the benefit of our study is its efficiency and uniqueness of the targets. For the former, we can simultaneously search for the Mpc-scale Lyα emitting structure (Chapter 2) and kpc- to tens of kpc-scale LAHs around the LAE by obtaining thousands of LAEs across environments (Chapter 2). Before the advent of the HSC, deep multiple pointing observations with S-Cam was the most efficient way. Now we can study ~ 7 times more efficient. For the latter, we chose a unique field around a protocluster which contains hyperluminous QSO. To detect very diffuse emission from the IGM, only strategy we can take is to target denser environments with additional supports from ionizing radiation from nearby sources are available. The effectiveness of our strategy will be justified after the planned follow-up observation presented in Section 4.3.1.

The last benefits could be also a caveat of this study — which is, a possible bias introduced by targeting at one of the brightest QSOs in the Universe. If such high luminosity of QSOs is only achieved in very special circumstances, the observed trend may not be general. The bolometric luminosity of the QSO, $1.5 \times 10^{14} L_{\odot}$ is, though very rare, not impossibly high. Protoclusters are rare in the first place and defining "normal" protoclusters is difficult and actually there are not enough protoclusters studied to date. At this stage where evidence for the cosmic web and cold-mode accretion is still scarce, mere detection should have significant value in itself. To overcome this possible caveat, more and more observations are needed to know how diverse protoclusters are. In Section 4.3.3, we present a next step we start to take to enlarge sample of protoclusters and detection of the cosmic web.

4.3 Future Prospects

We end this thesis by discussing what should be done next to extend this study. Detailed introduction of ongoing relevant observational projects are presented in Appendix A.

4.3.1 Further Observations of Diffuse Nebulae

Very recently, the first direct image of the cosmic web was captured in the SSA22 protocluster at $z = 3.1$ with a wide-field ($1' \times 1'$ FoV), sensitive integral field spectrograph, the Multi-Unit Spectroscopic Explorer (MUSE) on the Very Large Telescope (Umehata et al., 2019). The SSA22 protocluster is qualitatively very similar to the HS1549 protocluster; it has a comparable total mass of $\sim 10^{15}\ M_{\odot}$ (Steidel et al., 1998) and contains significant overdensity of giant LABs (Matsuda et al., 2004), AGNs (Alexander et al., 2016), and SMGs (Umehata et al., 2018) and is located at the node of filamentary structures of LAEs (Matsuda et al., 2005). Similar hints are seen in another protocluster at $z = 2.3$ (Erb et al., 2011). These suggest that such diffuse filaments is generic feature of forming clusters at the cosmic noon, as already discussed in Section 3.5.3. The natural next step we should take is further characterization of such diffuse nebulae. What are their gas mass, density, and temperature, and whether it is inflowing or outflowing with respect to galaxies nearby, are pivotal questions to be answered with cutting-edge instruments.

The filament we discovered in Chapter 2 is the most promising candidate to be followed up. The filament detected in the SSA22 field is also bright in some parts, but due to its complex configuration the center of the protocluster is hard to define as opposed to our case with HS1549+1919, making interpretation difficult. With motivations described above, we proposed Keck/KCWI observations of a diffuse Lyα nebula through Subaru-Keck time-exchange program in S20A semester and 2 nights were awarded in June 2020. We modeled this nebula assuming it represents cold filament gas, and test if this is true by analyzing the spatially resolved Lyα line to derive $N_{\rm HI}$ and line of sight velocity of the emitting cloud, which should be very different from the Lyα line from star-forming galaxies.

If the filament is not just a nebula associated with a hidden source within it, the most natural explanation then is that it represent a denser portion of a cold filament that has been long sought after, given the alignment with the large-scale LAE distribution (Figure 2.7, 2.9). Because gravitational energy alone cannot explain the observable level of Lyα luminosity unless gas is within a virial radius of massive ($M_{\rm h} > 10^{12.5} M_{\odot}$) halos (Faucher-Giguère et al., 2010), QSO illumination is the most likely power source, as discussed in Section 2.4.2. We illustrate a model for the filament in Figure 4.1. It is made of a number of low-mass, compact, and thus unresolved halos ($M_{\rm h} < 10^{9} M_{\odot}$, or a kind of "proto-galaxies") which can naturally exist in the cosmic web and ambient ionized gas. An ionized skin around small halos can be dense enough to produce observed Lyα luminosity, making the clumping factor high. $N_{\rm HI}$ should be in the range of 10^{14}–10^{17} cm^{-2} to let Lyman continuum in but is also able to scatter Lyα. This value is roughly consistent with cosmological simulations given the HI fraction derived by the QSO radiation field. Details of the model will be presented elsewhere (Cen et al. in prep.).

More details can be found in Section A.1.

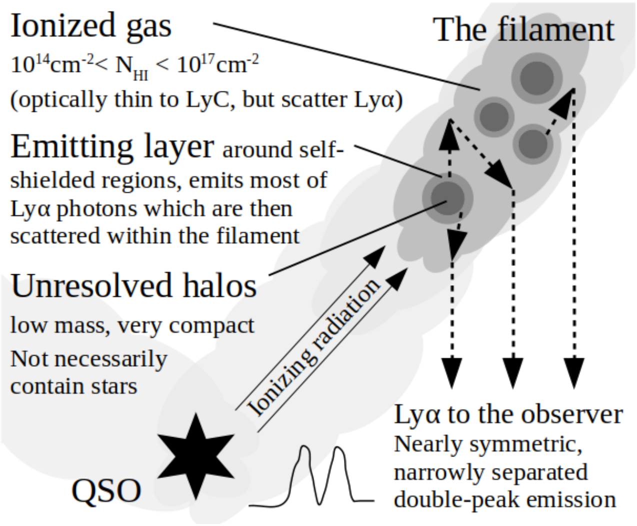

Figure 4.1: Schematic picture of the filament.

4.3.2 Unveiling Obscured Activities within the Protocluster Core with ALMA

We mainly utilized the Lyα emission and UV continuum emission to map the large-scale structure around the HLQSO in Chapter 2. However, very active phenomena occurring at the core of the protocluster must simultaneously produce a significant amount of dust, making themselves elusive in UV/optical lights, as explained in Section 1.4 and 1.5. Rest-frame FIR observations are therefore indispensable to obtain a complete picture of galaxy formation and evolution in the densest environments. Lacaille et al. (2019) conducted a survey using JCMT/SCUBA2 (a submillimeter bolometer camera) and found 6 times more 850μm submillimeter sources around the HS1549 than in blank fields (Fig.A.2a). This suggests that a large number of dusty gas-rich starburst galaxies are indeed hidden in the core. If most of the SCUBA2 sources are associated with this protocluster, the inferred total star-formation rate density in the core would be $\sim 3000\,M_\odot\,\mathrm{yr}^{-1}\,\mathrm{Mpc}^{-3}$, which is $\sim 10^4\times$ higher than that in blank fields at the same redshift. A detailed survey with ALMA, which has much better sensitivity and spatial resolution than SCUBA2 is thus necessary.

Detailed description of the target field and aims of our observations can be found in Section A.2.

4.3.3 Observations for Other Protoclusters

To extend our study, we must observe more and more actively forming protoclusters to confirm if the diffuse Lyα emission is a generic feature of forming protocluster at cosmic noon. Here, we introduce another example of a forming protocluster at $z = 3.3$ discovered in HSC-SSP survey. This field is also a good candidate for the cosmic web observations as it contains protoclusters and intense ionizing photon sources, similar to the HS1549 field. Moreover, LAHs of LAEs studied with this field complement our investigation presented in Chapter 3, because the hyperluminous QSO may affect the CGM of LAEs around the field via its intense ionizing radiation. The QSOs in this pair QSO field is not as strong as HS1549+1919 and its "sphere of influence" should be smaller compared to the field of view.

Together with the results for the HS1549 field, more comprehensive view of the CGM of LAE will be obtained. Of course, we will continue searching for new protoclusters that can be similarly probed with narrowband filters installed on the HSC. Description and current status of our analysis of the pair QSO field is given in Section A.3.

A

Appendix: Details of Ongoing Observational Projects

In this Appendix, we provide the aims of our ongoing projects described in Section 4.3.1, Section 4.3.2 and Section 4.3.3 and how they can be achieved in much detail.

A.1 Details of IFU observations for the filament

What we do with KCWI datacube is to analyse the spatially resolved Lyα line to know $N_{\rm HI}$ and the line of sight velocity of the filament. Due to its resonant nature, the Lyα line from optically thick ($N_{\rm HI} > 10^{14}$ cm^{-2}) media naturally becomes double-peaked, with its separation widen with increasing $N_{\rm HI}$. If there is velocity difference between scattering media and emitting regions, one of the two peaks is significantly weakened (Verhamme et al., 2015). High-redshift star-forming galaxies typically have $N_{\rm HI} > 10^{18}$ cm^{-2} and separation larger than 300 km s^{-1} (if both peaks are observed, e.g., Erb et al., 2018). Moreover, since outflow is ubiquitous in their spectra (Sugahara et al., 2017), basically the redder peak is stronger than the other (sometimes only a broad red peak is observed). By contrast, if our model is valid, $N_{\rm HI}$ in the filament should be lower than in galaxies because of ionization. In addition, ambient gas and small halos are inflowing with the same speed and streams do not show significant motion perpendicular to the web which causes velocity difference. Thus, an emergent line shape should be dramatically different from those of galaxies: double-peak emission with a small (< 200km s^{-1}) separation and peak ratio about unity. We measure the peak separation, peak flux ratio, and spatial variation of them. We would also be able to map line-center velocity and dispersion along the filament. Simulation predict roughly constant inflow velocity due to radiative cooling and gas heating (=growing velocity dispersion) in the course of infall (Goerdt & Ceverino, 2015), giving us a chance to directly test these theories.

Again, our target, the filament, is the first promising object to observationally constrain physical properties of the cold filament with sufficient brightness for existing instruments. Moreover, implications from our model, if proved, are significant; star formation, gas richness, etc. in such small halos at high redshift. In the future, our ALMA observations for the field (Section A.2) will put a stronger constraint on possible hidden sources. Low-mass halos should be very compact when seen in Hα, which can be tested with JWST/NIRCam.

A.2 Unveiling Obscured Activities within the Protocluster Core with ALMA

We proposed ALMA 1.3mm (band 6) continuum mosaicing observations for the $6' \times 5'$ core region of the $z = 2.84$ protocluster in Cycle 7 (Figure A.1). The proposal was accepted with a priority grade B (Program ID: 2019.1.00403.S, PI: S. Kikuta) and the data is now all delivered. With the data, we will compare the 1.3mm number count in the core with that in blank fields to test if intense activity preferentially triggered in protoclusters. Similar mosaicing observations for the core of SSA22 protocluster (also done in band 6) revealed that an excess of the number count by a factor of 3–5 down to ~ 0.5 mJy (Figure A.2(b), Umehata et al. 2017). However, the faintest bin of their differential counts shows little evidence of excess, implying "downsizing" trend, where accelerated formation first occurs selectively in the massive-end as simulations suggest (Muldrew et al., 2018).

In addition, we will investigate the connection between dusty star formation and LABs and AGNs in the field to understand the co-evolution between them. Constraining their obscured star formation through FIR luminosity is vital to know the origins of LABs by pinning down the power sources. ALMA observations of AGNs enable us to study their host galaxy properties such as SFR and morphology, which is impossible with shorter wavebands due to contaminated AGN light. From their SFR, we can know the relative growth of SMBHs and stellar components and how this is different compared to that in blank fields (Alexander et al., 2016). Simulations predict different SFR-to-black hole growth rate ratio depending on how AGNs are triggered (e.g., gas-rich merger VS. secular process, Bournaud et al. 2011).

A.3 Narrowband Observations around a Pair Quasar Field at $z = 3.3$

We conducted narrow-band (NB527, $\lambda_c = 5260$Å and $\Delta\lambda = 80$Å) imaging observations for the protocluster field at $z = 3.3$ with HSC (S19A-QN138, PI: S. Kikuta). The field (Figure A.3), namely "QSOP2" field, originally found as an overdense region of Lyman break galaxies (LBGs) around a QSO pair (two SDSS-BOSS QSOs are at $z = 3.31$ and $z = 3.33$ with projected separation $R_\perp = 1.04$ pMpc) in Onoue et al. (2018) using HSC-SSP survey data. A preliminary analysis of a search for [OIII] emitters at $z = 3.3$ with narrow-band imaging using Subaru/MOIRCS suggests a factor of 30 overdensity compared to the number density in the blank field (Sobral et al., 2013) around the QSOs. In addition to two BOSS QSO, another fainter QSO candidate 2 pMpc away from the pair center is also reported in Onoue et al. (2018). Furthermore, wide field of view of HSC enables us to simultaneously observe an isolated BOSS QSO at $z = 3.34$ located at ~ 7 pMpc away from the pair and another protocluster candidate which have independently discovered by Toshikawa et al. (2018).

This field is a perfect laboratory for our purpose because we can simultaneously probe "cluster+QSO", "QSO", "cluster", and normal environment. These QSO's "spheres of influence" where their radiation dominate over the cosmic average are about a few

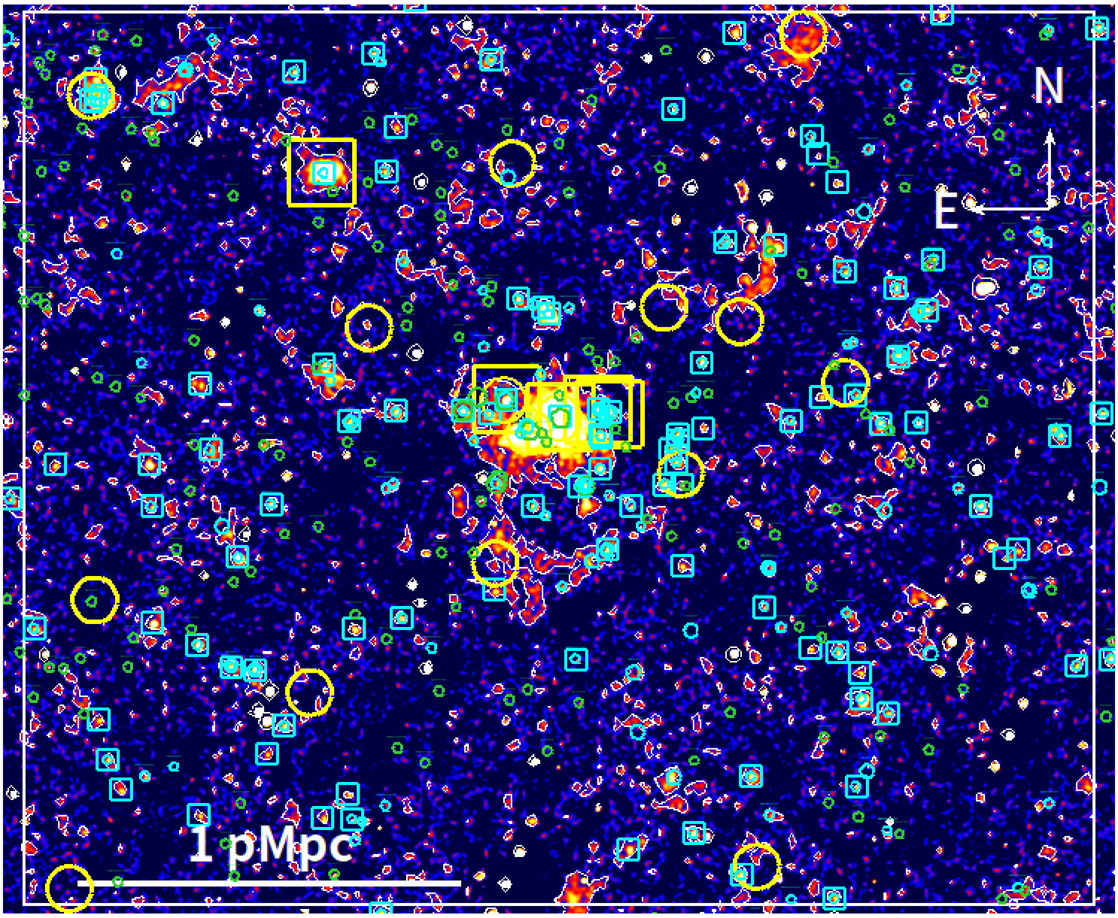

Figure A.1: Lyα image of the core region with the ALMA coverage ($6' \times 5'$, white box) and targets of interests marked. Cyan squares and circles respectively show LAEs and LBGs at $2.82 < z < 2.89$. Green circles show spectroscopically confirmed foreground or background LBGs at $1.5 < z < 3.0$. Yellow squares and circles are AGNs at $z \sim 2.84$ and SCUBA2 sources. To maximize the survey efficiency, we set the field to contain as much galaxy populations as possible simultaneously covering the densest part of the protocluster. There are 15 SCUBA2 sources, 10 LABs, 5 AGNs, 110 NB-selected LAEs and 317 galaxies at $1.5 < z < 3$ with spec-z in the proposed 30 arcmin^2 field.

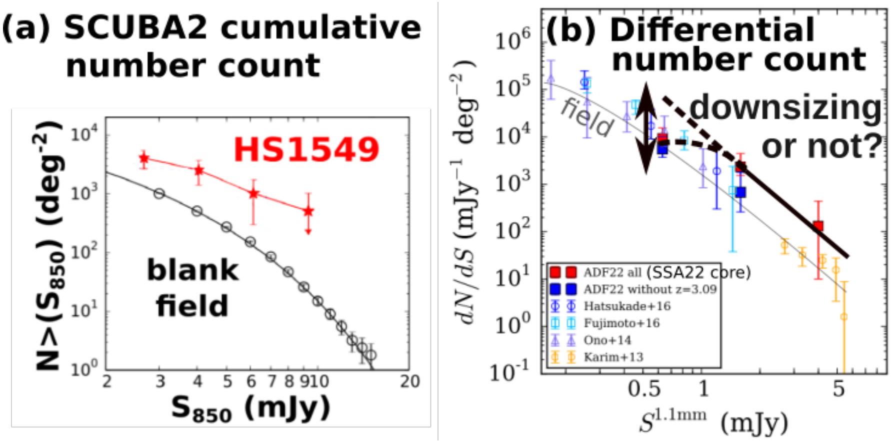

Figure A.2: **(a)** The cumulative number counts of SCUBA2 850μm sources in the HS1549 protocluster core and blank fields (Lacaille et al., 2019). The counts of HS1549 field shows an excess by a factor of 6. **(b)** The differential number count in the different (SSA22) protocluster and blank fields (Umehata et al., 2017). While red points (for a protocluster core) shows an excess at brighter side, there is no evidence of an excess at the faintest bin. The proposed ALMA observations of the HS1549 protocluster core will test if such downsizing trend is ubiquitous in high-redshift protoclusters.

pMpc, so their influence can be properly separated. This complete set of environments and HSC's wide field of view and high sensitivity for the first time enable us to guess by what mechanisms LAHs become larger; a strong ionizing field and/or an overdensity of matter? Does dependence on environments exist in this field as opposed to our inference presented in Section 3.5.2? Or just their hosts properties such as UV magnitude matter? With a sufficient depth, we will detect statistically meaningful ($>$ 3000) number of LAEs and investigate their LAH properties (luminosity and scalelength) as a function of various quantities through stacking analysis in a consistent manner as done in Chapter 3. Because a half of our field is considered to be general field, obtained conclusion on LAHs will not be biased.

We expect to find numerous Lyα blobs (LABs) around the protocluster (recall Section 2.3.1). In addition, luminous QSOs at $z > 3$ are known to ubiquitously have giant Lyα nebulae (Borisova et al., 2016; Arrigoni Battaia et al., 2019). Illumination by the QSO pair would further boost the emission around them. In the era of new IFUs (e.g., KCWI, MUSE, and FOCAS IFU) and also JWST, such discovery is invaluable to study physical states of Lyα nebulae in greater detail.

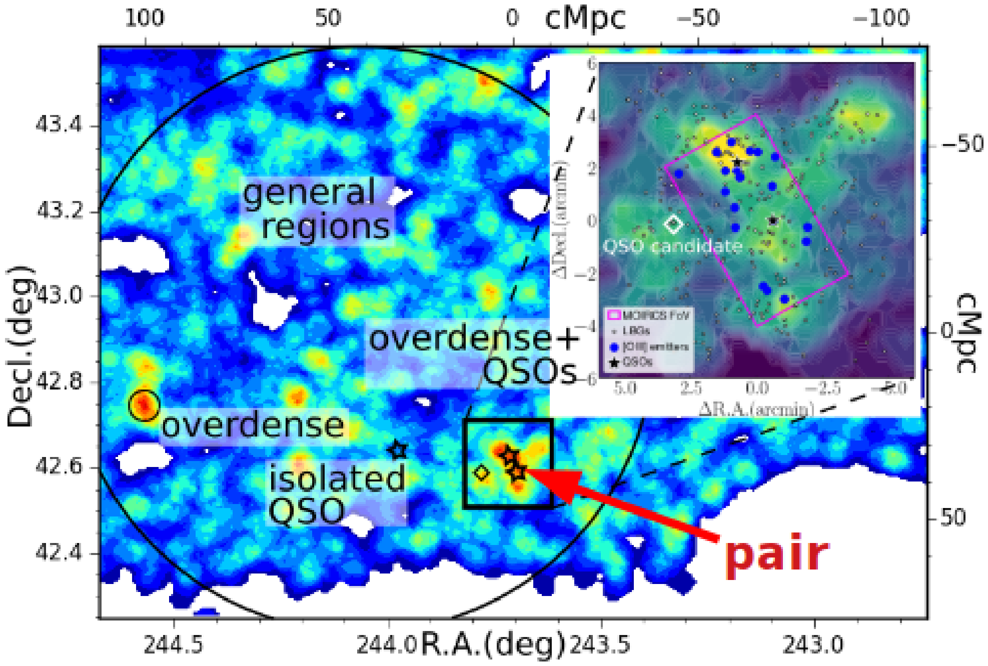

Figure A.3: Overview of our target field including a QSO pair at $z = 3.3$. Color shows a overdensity significance map. Stars are QSOs at $z = 3.3$, the diamond shows QSO candidate, and the small circle marks another protocluster candidate. The large circle illustrates FoV of HSC ($\sim 1.5°$ diameter). White regions are where no galaxy exists or no data is available. Gray dots and blue circles in the insets are LBGs with $i_{\rm HSC} < 26$ mag and [OIII] emitters.

We almost completed data reduction and are about to start selection of LAEs at $z = 3.3$. Figure A.4 shows a cutout of the resultant NB and g-band images obtained in our open-use program and HSC-SSP around the one of the QSO in the pair. Next, we will map out the large-scale structure across the field, and investigate LAHs of LAEs within various environments in the way we specified in Chapter 2 and Chapter 3. In this way, we will extend our protocluster sample to further study the IGM and the CGM, and finally test if the cold filaments and diffuse Lyα emission is generic feature in massive halos at cosmic noon.

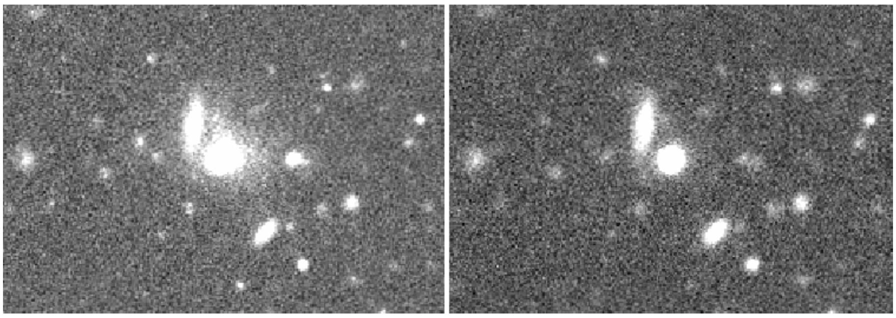

Figure A.4: NB527 (left) and g-band (right) image of one of the QSO in the pair at $z = 3.3$. Extended emission around the QSO and some LAEs are already visible in the NB527 image.

Bibliography

Abolfathi, B., Aguado, D. S., Aguilar, G., et al. 2018, The Astrophysical Journal Supplement Series, 235, 42

Adams, S. M., Martini, P., Croxall, K. V., Overzier, R. A., & Silverman, J. D. 2015, Monthly Notices of the Royal Astronomical Society, 448, 1335

Adelberger, K. L., Shapley, A. E., Steidel, C. C., et al. 2005, The Astrophysical Journal, 629, 636

Agertz, O., Teyssier, R., & Moore, B. 2009, Monthly Notices of the Royal Astronomical Society: Letters, 397, 64

Alexander, D. M., Bauer, F. E., Chapman, S. C., et al. 2005, The Astrophysical Journal, 632, 736

Alexander, D. M., Simpson, J. M., Harrison, C. M., et al. 2016, Monthly Notices of the Royal Astronomical Society, 461, 2944

Ando, M., Ohta, K., Iwata, I., et al. 2006, The Astrophysical Journal, 645, L9

Arrigoni Battaia, F., Hennawi, J. F., Prochaska, J. X., et al. 2019, Monthly Notices of the Royal Astronomical Society, 482, 3162

Bacon, R., Vernet, J., Borisiva, E., et al. 2014, 13

Bădescu, T., Yang, Y., Bertoldi, F., et al. 2017, The Astrophysical Journal, 845, 172

Baldry, I. K., Glazebrook, K., Brinkmann, J., et al. 2004, The Astrophysical Journal, 600, 681

Baldry, I. K., Glazebrook, K., & Driver, S. P. 2008, Monthly Notices of the Royal Astronomical Society, 388, 945

Bañados, E., Venemans, B., Walter, F., et al. 2013, The Astrophysical Journal, 773, 178

Bertin, E., & Arnouts, S. 1996, Astronomy and Astrophysics Supplement Series, 117, 393

Birnboim, Y., & Dekel, A. 2003, Monthly Notices of the Royal Astronomical Society, 345, 349

Borisova, E., Cantalupo, S., Lilly, S. J., et al. 2016, The Astrophysical Journal, 831, 39

Bosch, J., Armstrong, R., Bickerton, S., et al. 2018, Publications of the Astronomical Society of Japan, 70, 1

Bournaud, F., Dekel, A., Teyssier, R., et al. 2011, Astrophysical Journal Letters, 741, 6

Bouwens, R. J., Illingworth, G. D., Oesch, P. A., et al. 2015, The Astrophysical Journal, 803, 34

Butcher, H., & Oemler, A. J. 1984, The Astrophysical Journal, 285, 426

Cai, Z., Cantalupo, S., Prochaska, J. X., et al. 2019

Cano-Díaz, M., Maiolino, R., Marconi, A., et al. 2012, Astronomy & Astrophysics, 537, L8

Cantalupo, S., Arrigoni-Battaia, F., Prochaska, J. X., Hennawi, J. F., & Madau, P. 2014, Nature, 506, 63

Cantalupo, S., Porciani, C., Lilly, S. J., & Miniati, F. 2005, The Astrophysical Journal, 628, 61

Cantalupo, S., Pezzulli, G., Lilly, S. J., et al. 2019, Monthly Notices of the Royal Astronomical Society, 483, 5188

Capak, P. L., Riechers, D., Scoville, N. Z., et al. 2011, Nature, 470, 233

Cappellari, M., Emsellem, E., Krajnović, D., et al. 2011, Monthly Notices of the Royal Astronomical Society, 416, 1680

Cen, R. 2012, The Astrophysical Journal, 748, 121

—. 2014, The Astrophysical Journal, 789, L21

Cen, R., & Zheng, Z. 2013, The Astrophysical Journal, 775, 112

Chiang, Y.-K., Overzier, R., & Gebhardt, K. 2013, The Astrophysical Journal, 779, 127

Cicone, C., Maiolino, R., Gallerani, S., et al. 2015, 14, 1

Corlies, L., Peeples, M. S., Tumlinson, J., et al. 2018

Cowie, L. L., & Hu, E. M. 1998, The Astronomical Journal, 115, 1319

Croton, D. J., Gao, L., & White, S. D. 2007, Monthly Notices of the Royal Astronomical Society, 374, 1303

Dekel, A., & Birnboim, Y. 2006, Monthly Notices of the Royal Astronomical Society, 368, 2

Dekel, A., Birnboim, Y., Engel, G., et al. 2009, Nature, 457, 451

Dijkstra, M., & Kramer, R. 2012, Monthly Notices of the Royal Astronomical Society, 424, 1672

Dijkstra, M., & Loeb, A. 2009, Monthly Notices of the Royal Astronomical Society, 400, 1109

Dressler, A. 1980, The Astrophysical Journal, 236, 351

Erb, D. K., Bogosavljević, M., & Steidel, C. C. 2011, Astrophysical Journal Letters, 740, L31

Erb, D. K., Steidel, C. C., & Chen, Y. 2018, The Astrophysical Journal, 862, L10

Falder, J. T., Stevens, J. A., Jarvis, M. J., et al. 2011, The Astrophysical Journal, 735, 123

Fardal, M. A., Katz, N., Gardner, J. P., et al. 2001, The Astrophysical Journal, 562, 605

Faucher-Giguère, C.-A., Kereš, D., Dijkstra, M., Hernquist, L., & Zaldarriaga, M. 2010, The Astrophysical Journal, 725, 633

Feldmeier, J. J., Hagen, A., Ciardullo, R., et al. 2013, The Astrophysical Journal, 776, 75

Feruglio, C., Maiolino, R., Piconcelli, E., et al. 2010, Astronomy & Astrophysics, 155, 1

Fielding, D., Quataert, E., McCourt, M., & Thompson, T. A. 2017, Monthly Notices of the Royal Astronomical Society, 466, 3810

Francis, P. J., Williger, G. M., Collins, N. R., et al. 2001, The Astrophysical Journal, 554, 1001

Fujimoto, S., Ouchi, M., Ferrara, A., et al. 2019

Garel, T., Blaizot, J., Guiderdoni, B., et al. 2015, Monthly Notices of the Royal Astronomical Society, 450, 1279

Goerdt, T., & Ceverino, D. 2015, Monthly Notices of the Royal Astronomical Society, 450, 3359

Goerdt, T., Dekel, A., Sternberg, A., et al. 2010, Monthly Notices of the Royal Astronomical Society, 407, 613

Gould, A., & Weinberg, D. H. 1996, The Astrophysical Journal, 468, 462

Gronke, M., & Bird, S. 2017, The Astrophysical Journal, 835, 207

Haardt, F., & Madau, P. 2012, The Astrophysical Journal, 746, 125

Haiman, Z., & Rees, M. J. 2001, The Astrophysical Journal, 556, 87

Harikane, Y., Ouchi, M., Ono, Y., et al. 2018, Publications of the Astronomical Society of Japan, 70, 1

Hashimoto, T., Ouchi, M., Shimasaku, K., et al. 2017, Monthly Notices of the Royal Astronomical Society, 465, 1543

Hayashino, T., Matsuda, Y., Tamura, H., et al. 2004, The Astronomical Journal, 128, 2073

Heckman, T. M., Alexandroff, R. M., Borthakur, S., Overzier, R., & Leitherer, C. 2015, The Astrophysical Journal, 809, 147

Heckman, T. M., Miley, G. K., Lehnert, M. D., & van Breugel, W. 1991, The Astrophysical Journal, 370, 78

Hennawi, J. F., Prochaska, J. X., Cantalupo, S., & Arrigoni-Battaia, F. 2015, Science, 348, 779

Hernquist, L., & Mihos, J. C. 1995, The Astrophysical Journal, 448, 41

Higuchi, R., Ouchi, M., Ono, Y., et al. 2018

Hopkins, A. M., & Beacom, J. F. 2006, The Astrophysical Journal, 651, 142

Hopkins, P. F., Somerville, R. S., Hernquist, L., et al. 2006, The Astrophysical Journal, 652, 864

Hummels, C. B., Smith, B. D., Hopkins, P. F., et al. 2018

Husband, K., Bremer, M. N., Stanway, E. R., et al. 2013, Monthly Notices of the Royal Astronomical Society, 432, 2869

Infante-Sainz, R., Trujillo, I., & Román, J. 2019, Monthly Notices of the Royal Astronomical Society, 14, 1

Ishiyama, T., Enoki, M., Kobayashi, M. A., et al. 2015, Publications of the Astronomical Society of Japan, 67, 1

Jiang, L., Egami, E., Fan, X., et al. 2013, Astrophysical Journal, 773, doi:10.1088/0004-637X/773/2/153

Kashikawa, N., Kitayama, T., Doi, M., et al. 2007, The Astrophysical Journal, 663, 765

Kashikawa, N., Aoki, K., Asai, R., et al. 2002, Publications of the Astronomical Society of Japan, 54, 819

Kashikawa, N., Shimasaku, K., Malkan, M. A., et al. 2006, The Astrophysical Journal, 648, 7

Katz, N., & White, S. D. M. 1993, The Astrophysical Journal, 412, 455

Kauffmann, G., & Haehnelt, M. 2000, Monthly Notices of the Royal Astronomical Society, 311, 576

Kauffmann, G., Heckman, T. M., White, S. D. M., et al. 2003, Monthly Notices of the Royal Astronomical Society, 341, 33

Keel, W. C., Cohen, S. H., Windhorst, R. A., & Waddington, I. 1999, The Astronomical Journal, 118, 2547

Kereš, D., Katz, N., Fardal, M., Davé, R., & Weinberg, D. H. 2009, Monthly Notices of the Royal Astronomical Society, 395, 160

Kereš, D., Katz, N., Weinberg, D. H., & Davé, R. 2005, Monthly Notices of the Royal Astronomical Society, 363, 2

Kikuta, S., Imanishi, M., Matsuoka, Y., et al. 2017, The Astrophysical Journal, 841, 128

Kikuta, S., Matsuda, Y., Cen, R., et al. 2019, Publications of the Astronomical Society of Japan, 71, 1

Kim, S., Stiavelli, M., Trenti, M., et al. 2009, The Astrophysical Journal, 695, 809

Kodama, T., Tanaka, I., Kajisawa, M., et al. 2007, Monthly Notices of the Royal Astronomical Society, 377, 1717

Kollmeier, J. A., Zheng, Z., Davé, R., et al. 2010, The Astrophysical Journal, 708, 1048

Koyama, Y., Kodama, T., Tadaki, K. I., et al. 2013, Monthly Notices of the Royal Astronomical Society, 428, 1551

Lacaille, K., Chapman, S., Smail, I., et al. 2018

Lacaille, K. M., Chapman, S. C., Smail, I., et al. 2019, Monthly Notices of the Royal Astronomical Society, 488, 1790

Lake, E., Zheng, Z., Cen, R., et al. 2015, Astrophysical Journal, 806, 46

Leclercq, F., Bacon, R., Wisotzki, L., et al. 2017, Astronomy & Astrophysics, 608, A8

Magorrian, J., Tremaine, S., Richstone, D., et al. 1998, The Astronomical Journal, 115, 2285

Martin, D. C., Chang, D., Matuszewski, M., et al. 2014, The Astrophysical Journal, 786, 106

Mas-Ribas, L., & Dijkstra, M. 2016, The Astrophysical Journal, 822, 84

Matsuda, Y., Yamada, T., Hayashino, T., et al. 2004, The Astronomical Journal, 128, 569

—. 2005, The Astrophysical Journal, 634, L125

Matsuda, Y., Nakamura, Y., Morimoto, N., et al. 2009, Monthly Notices of the Royal Astronomical Society: Letters, 400, L66

Matsuda, Y., Yamada, T., Hayashino, T., et al. 2011, Monthly Notices of the Royal Astronomical Society: Letters, 410, 13

—. 2012, Monthly Notices of the Royal Astronomical Society, 425, 878

Mazzucchelli, C., Bañados, E., Decarli, R., et al. 2017, The Astrophysical Journal, 834, 83

McNamara, B. R., Kazemzadeh, F., Rafferty, D. A., et al. 2009, The Astrophysical Journal, 698, 594

Miralda-Escude, J., Cen, R., Ostriker, J. P., & Rauch, M. 1996, The Astrophysical Journal, 471, 582

Miyazaki, S., Komiyama, Y., Nakaya, H., et al. 2012in , 84460Z

Momose, R., Ouchi, M., Nakajima, K., et al. 2014, Monthly Notices of the Royal Astronomical Society, 442, 110

—. 2016, Monthly Notices of the Royal Astronomical Society, 457, 2318

Moore, B., Ghigna, S., Governato, F., et al. 1999, The Astrophysical Journal, 524, L19

Mori, M., & Umemura, M. 2006, Nature, 440, 644

Morrissey, P., Matuszewski, M., Martin, D. C., et al. 2018, The Astrophysical Journal, 864, 93

Morselli, L., Mignoli, M., Gilli, R., et al. 2014, Astronomy & Astrophysics, 568, A1

Mostardi, R. E., Shapley, A. E., Nestor, D. B., et al. 2013, The Astrophysical Journal, 779, 65

Muldrew, S. I., Hatch, N. A., & Cooke, E. A. 2018, Monthly Notices of the Royal Astronomical Society, 473, 2335

Murphy, E. J., Condon, J. J., Schinnerer, E., et al. 2011, The Astrophysical Journal, 737, 67

Nelson, D., Vogelsberger, M., Genel, S., et al. 2013, Monthly Notices of the Royal Astronomical Society, 429, 3353

Ocvirk, P., Pichon, C., & Teyssier, R. 2008, Monthly Notices of the Royal Astronomical Society, 390, 1326

Ono, Y., Ouchi, M., Harikane, Y., et al. 2017, 00, 1

Onoue, M., Kashikawa, N., Uchiyama, H., et al. 2018, Publications of the Astronomical Society of Japan, 70, S31

Ouchi, M., Shimasaku, K., Furusawa, H., et al. 2003, The Astrophysical Journal, 582, 60

Ouchi, M., Shimasaku, K., Okamura, S., et al. 2004, The Astrophysical Journal, 611, 660

Ouchi, M., Shimasaku, K., Akiyama, M., et al. 2005, The Astrophysical Journal, 620, L1

—. 2008, The Astrophysical Journal Supplement Series, 176, 301

Ouchi, M., Shimasaku, K., Furusawa, H., et al. 2010, The Astrophysical Journal, 723, 869

Ouchi, M., Harikane, Y., Shibuya, T., et al. 2017, 1

Overzier, R. A. 2016, The Astronomy and Astrophysics Review, 24, 14

Overzier, R. A., Nesvadba, N. P. H., Dijkstra, M., et al. 2013, The Astrophysical Journal, 771, 89

Ozaki, S., Tanaka, Y., Hattori, T., et al. 2014in , 915149

Peeples, M. S., Corlies, L., Tumlinson, J., et al. 2018

Planck Collaboration, Ade, P. A. R., Aghanim, N., et al. 2015, 1

Prescott, M. K. M., Kashikawa, N., Dey, A., & Matsuda, Y. 2008, The Astrophysical Journal, 678, L77

Prescott, M. K. M., Momcheva, I., Brammer, G. B., Fynbo, J. P. U., & Møller, P. 2015, The Astrophysical Journal, 802, 32

Press, W. H., & Schechter, P. 1974, The Astrophysical Journal, 187, 425

Prochaska, J. X., Werk, J. K., Worseck, G., et al. 2017, The Astrophysical Journal, 837, 169

Rakic, O., Schaye, J., Steidel, C. C., & Rudie, G. C. 2012, Astrophysical Journal, 751, doi:10.1088/0004-637X/751/2/94

Rauch, M., Sargent, W. L. W., & Barlow, T. A. 1999, The Astrophysical Journal, 515, 500

Rauch, M., Haehnelt, M., Bunker, A., et al. 2008, The Astrophysical Journal, 681, 856

Rees, M. J., & Ostriker, J. P. 1977, Monthly Notices of the Royal Astronomical Society, 179, 541

Rhoads, J. E., Malhotra, S., Dey, A., et al. 2000, The Astrophysical Journal, 545, L85

Rosdahl, J., & Blaizot, J. 2012, Monthly Notices of the Royal Astronomical Society, 423, 344

Rudie, G. C., Steidel, C. C., Trainor, R. F., et al. 2012, The Astrophysical Journal, 750, 67

Sanders, D. B., Soifer, B. T., Elias, J. H., et al. 1988, The Astrophysical Journal, 325, 74

Sargent, W. L. W., Young, P. J., Boksenberg, A., & Tytler, D. 1980, The Astrophysical Journal Supplement Series, 42, 41

Schaerer, D. 2003, Astronomy and Astrophysics, 397, 527

Schaye, J., Carswell, R. F., & Kim, T. S. 2007, Monthly Notices of the Royal Astronomical Society, 379, 1169

Schlafly, E. F., Finkbeiner, D. P., Jurić, M., et al. 2012, The Astrophysical Journal, 756, 158

Schlegel, D. J., Finkbeiner, D. P., & Davis, M. 1998, The Astrophysical Journal, 500, 525

Scoville, N. Z., Evans, A. S., Thompson, R., et al. 2000, The Astronomical Journal, 119, 991

Shimasaku, K., Ouchi, M., Furusawa, H., et al. 2005, Publications of the Astronomical Society of Japan, 57, 447

Shimasaku, K., Ouchi, M., Okamura, S., et al. 2003, The Astrophysical Journal, 586, 111

Shioya, Y., Taniguchi, Y., Sasaki, S. S., et al. 2009, The Astrophysical Journal, 696, 546

Simpson, C., Mortlock, D., Warren, S., et al. 2014, Monthly Notices of the Royal Astronomical Society, 442, 3454

Sobral, D., Smail, I., Best, P. N., et al. 2013, Monthly Notices of the Royal Astronomical Society, 428, 1128

Springel, V., Di Matteo, T., & Hernquist, L. 2005a, Monthly Notices of the Royal Astronomical Society, 361, 776

Springel, V., White, S. D. M., Jenkins, A., et al. 2005b, Nature, 435, 629

Steidel, C. C., Adelberger, K. L., Dickinson, M., et al. 1998, The Astrophysical Journal, 492, 428

Steidel, C. C., Adelberger, K. L., Shapley, A. E., et al. 2005, The Astrophysical Journal, 626, 44

—. 2000, The Astrophysical Journal, 532, 170

Steidel, C. C., Bogosavljević, M., Shapley, A. E., et al. 2011, The Astrophysical Journal, 736, 160

Steidel, C. C., Erb, D. K., Shapley, A. E., et al. 2010, Astrophysical Journal, 717, 289

Steidel, C. C., Giavalisco, M., Pettini, M., Dickinson, M., & Adelberger, K. L. 1996, The Astrophysical Journal, 462, L17

Stern, J., Fielding, D., Faucher-Giguère, C.-A., & Quataert, E. 2019, 17, 1

Sugahara, Y., Ouchi, M., Lin, L., et al. 2017, The Astrophysical Journal, 850, 51

Suresh, J., Nelson, D., Genel, S., Rubin, K. H., & Hernquist, L. 2019, Monthly Notices of the Royal Astronomical Society, 483, 4040

Swinbank, J., Baker, J., Barr, J., Hook, I., & Bland-Hawthorn, J. 2012, Monthly Notices of the Royal Astronomical Society, 422, 2980

Takata, T., Sekiguchi, K., Smail, I., et al. 2006, The Astrophysical Journal, 651, 713

Taniguchi, Y., & Shioya, Y. 2000, The Astrophysical Journal, 532, L13

Teyssier, R., Chapon, D., & Bournaud, F. 2010, The Astrophysical Journal, 720, L149

Toomre, A., & Toomre, J. 1972, The Astrophysical Journal, 178, 623

Toshikawa, J., Kashikawa, N., Ota, K., et al. 2012, The Astrophysical Journal, 750, 137

Toshikawa, J., Uchiyama, H., Kashikawa, N., et al. 2018, Publications of the Astronomical Society of Japan, 70, doi:10.1093/pasj/psx102

Trainor, R. F., & Steidel, C. C. 2012, The Astrophysical Journal, 752, 39

Trainor, R. F., Steidel, C. C., Strom, A. L., & Rudie, G. C. 2015, The Astrophysical Journal, 809, 89

Tumlinson, J., Peeples, M. S., & Werk, J. K. 2017, Annual Review of Astronomy and Astrophysics, 55, 389

Tumlinson, J., Thom, C., Werk, J. K., et al. 2011, Science, 334, 948

Turner, M. L., Schaye, J., Crain, R. A., et al. 2017, 20, 1

Uchiyama, H., Toshikawa, J., Kashikawa, N., et al. 2018, Publications of the Astronomical Society of Japan, 70, S32

Umehata, H., Tamura, Y., Kohno, K., et al. 2017, The Astrophysical Journal, 835, 98

Umehata, H., Hatsukade, B., Smail, I., et al. 2018, Publications of the Astronomical Society of Japan, 70, doi:10.1093/pasj/psy065

Umehata, H., Fumagalli, M., Smail, I., et al. 2019, Science, 366, 97

van de Voort, F., Schaye, J., Booth, C. M., Haas, M. R., & Dalla Vecchia, C. 2011, Monthly Notices of the Royal Astronomical Society, 414, 2458

van de Voort, F., Springel, V., Mandelker, N., van den Bosch, F. C., & Pakmor, R. 2019, Monthly Notices of the Royal Astronomical Society: Letters, 482, L85

van Ojik, R., Röttgering, H. J. A., Carilli, C. L., et al. 1996, Astronomy & Astrophysics, 313, 25

Venemans, B. P., Röttgering, H. J. A., Miley, G. K., et al. 2007, Astronomy & Astrophysics, 461, 823

Verhamme, A., Orlitová, I., Schaerer, D., & Hayes, M. 2015, Astronomy & Astrophysics, 578, A7

Vogelsberger, M., Genel, S., Springel, V., et al. 2014, Monthly Notices of the Royal Astronomical Society, 444, 1518

White, S. D. M., & Rees, M. J. 1978, Monthly Notices of the Royal Astronomical Society, 183, 341

Wisotzki, L., Bacon, R., Blaizot, J., et al. 2016, Astronomy & Astrophysics, 587, A98

Witstok, J., Puchwein, E., Kulkarni, G., Smit, R., & Haehnelt, M. G. 2019, 17, 1

Wylezalek, D., Galametz, A., Stern, D., et al. 2013, The Astrophysical Journal, 769, 79

Xue, R., Lee, K.-S., Dey, A., et al. 2017, The Astrophysical Journal, 837, 172

Yajima, H., Li, Y., & Zhu, Q. 2013, Astrophysical Journal, 773, doi:10.1088/0004-637X/773/2/151

Yamada, T., Nakamura, Y., Matsuda, Y., et al. 2012, The Astronomical Journal, 143, 79

Yang, Y., Zabludoff, A., Eisenstein, D., & Davé, R. 2010, The Astrophysical Journal, 719, 1654

Yoshida, M., Shimasaku, K., Kashikawa, N., et al. 2006, The Astrophysical Journal, 653, 988

Zhang, H., Ouchi, M., Itoh, R., et al. 2019

Zheng, W., Overzier, R. A., Bouwens, R. J., et al. 2006, The Astrophysical Journal, 640, 574

Zheng, Z., Cen, R., Weinberg, D., Trac, H., & Miralda-Escudé, J. 2011, The Astrophysical Journal, 739, 62